VNIVERSITAT DE VALÈNCIA

Facultat de Química

ICMUV
INSTITUT DE CIÈNCIA DELS MATERIALS de la Universitat de València

Optical hybrid nanocomposite sensors for selective explosive detection

Tesi Doctoral

Programa de Doctorat en Química

Autor

Eduardo Aznar Gadea

Supervisors

Dr. Rafael Abargues López

Dr. Pedro J. Rodríguez Cantó

València, Juny 2022

VNIVERSITAT DE VALÈNCIA

Programa de Doctorat en **Química**

Informe favorable de los directores para el depósito de tesis

Dr. Rafael Abargues López, Ramón y Cajal en la Universidad de Valencia y Dr. Pedro J. Rodríguez Cantó, colaborador científico del Instituto de Ciencia de los Materiales de la Universidad de Valencia.

Certifican que la presente tesis doctoral, titulada "**Optical hybrid nanocomposite sensors for selective explosive detection**" ha sido realizada por Eduardo Aznar Gadea bajo la dirección de ambos directores en el Instituto de Ciencia de los Materiales de la Universidad de Valencia (ICMUV), autorizando mediante este escrito la presentación de la misma para optar al grado de Doctor.

Valencia, a 21 de junio de 2022.

ABARGUES LOPEZ RAFAEL - 44852270Q

Firmado digitalmente por ABARGUES LOPEZ RAFAEL - 44852270Q
Fecha: 2022.09.29 16:44:10 +02'00'

Rafael Abargues López

RODRIGUEZ CANTO PEDRO JAVIER - 30819189V

Digitally signed by RODRIGUEZ CANTO PEDRO JAVIER - 30819189V
Date: 2022.09.29 13:25:08 +02'00'

Pedro J. Rodríguez Cantó

Als meus pares

Contents

Agraïments

La meua estada a l'Institut de Ciència dels Materials va començar l'any 2016 quan em van brindar l'oportunitat de treballar com a tècnic de suport a la investigació dins del programa de Garantia Juvenil i, dos anys després, vaig iniciar la meua etapa com a estudiant de doctorat. Aquest ha sigut un camí llarg i amb alguns contratemps, però també ha sigut una experiència molt enriquidora tant a nivell personal com professional. Per aquesta raó, voldria donar el meu agraïment a totes les persones que d'una forma o una altra han fet possible que aquesta tesi doctoral veja la llum.

En primer lloc, m'agradaria donar les gràcies al Prof. Juan Martínez Pastor i als meus directors de la tesi, el Dr. Rafael Abargues i el Dr. Pedro J. Rodríguez Cantó, per tot el treball de supervisió, la seua infinita paciència i el suport rebut que ha fet possible que aquesta tesi doctoral s'haja pogut dur-se a terme. També voldria expressar la meua gratitud a Volodymyr Chegel i Andrii Lopatynskyi per la seua col·laboració i ajuda en les seues estades a València, així com a totes les persones de Intenanomat i la Universitat de València que d'una manera o una altra han contribuït en que tot aquest treball haja pogut eixir endavant.

Al projecte de l'OTAN "*Technology of high-selective imprinted nanoantenna for explosives detection*" dins del "*Science for Peace and Security Programme*" que ha sigut la font de finançament que ha ajudat a portar endavant tota la investigació i, per tant, sense aquesta no haguera realitzat la tesi doctoral.

A la meua companya de despatx, amiga i confident, Sandra Albert, per tots els moments viscuts al despatx, per aconsellar-me, animar-me i ajudar-me de forma incondicional sempre que ho he necessitat però sobretot, per haver-me hagut de patir durant tots aquests anys.

A la meua parella, Vicent Noé, per estar sempre al meu costat, per la seua infinita paciència aguantant les meues històries encara que li sonaren a xinés i tranquil·litzar-me en les èpoques més estressants del doctorat.

A ma mare, Maria Dolores, per creure sempre en mi i ser un dels pilars fonamentals en la meua vida. A mon pare, Eduardo y a tota la meua família que ha confiat en mi durant aquest llarg camí.

I finalment, no volia oblidar-me de tots els meus amics que en algun moment han hagut de suportar el meus llargs discursos i maldecaps de forma desinteressada, especialment, Noelia Carbonell i Vanessa Rottier.

Moltes gràcies a tots, sense vosaltres tot açò no haguera sigut possible.

Abstract

Over the last decade, the detection of improvised explosive devices (IEDs) in both military and civil fields has become a strategic priority in homeland security due to the increasing terrorist threat. Although conventional techniques such as gas chromatography coupled to mass spectrometry or X-ray diffraction show notable advantages such as high sensitivity and selectivity, most of them have many drawbacks such as time-consuming processes and expensive, complex, and cumbersome instrumentation, which limit continuous and real-time sampling. For that reason, there is constant research for a sensing platform suitable for different environments.

The role of nanoscience has been greatly determining the development of chemical sensors with enhanced performance because of their outstanding properties. The design of low-cost, easy-to-fabricate and portable sensors with a low limit of detection (LOD), good selectivity, high sensitivity and short response time is very challenging. The goal of this PhD thesis is to synthesize different optical solid-state sensing platforms based on a nanocomposite of different nanoparticles embedded in a polymer matrix for the detection and quantification of some explosive taggants and explosive-like molecules in the vapour phase.

Firstly, the synthesis of a plasmonic sensor based on a nanocomposite of Ag nanoparticles (NPs) embedded in a molecularly imprinted polymer (MIP) for selective detection of 3-NT, an explosive taggant for 2,4,6-trinitrotoluene. In our approach, the in-situ synthesis of Ag NPs and the molecular imprinting with 3-NT as a template take place simultaneously inside the polyethyleneimine (PEI) thin film during the baking step after spin coating. The chemosensing capabilities of Ag-PEI MIP nanocomposites to 3-NT using the localized surface plasmon resonance band intensity decay as a sensing parameter were demonstrated. Moreover, the molecular imprinting approach results in an enhancement of the sensor sensitivity and selectivity to 3-NT. As a result, these plasmonic sensors can be easily implemented with portable reading platforms into remote explosive detection and bomb disposal robots.

In the second part, chemical sensors based on fluorescent nanoparticles such as quantum dots (QDs) and metal halide perovskites (PVKs) have been used because of their excellent optical and electronic properties. One of the sensors is based on an array

containing either green-emitting or red-emitting CdSe QDs embedded in polycaprolactone (PCL) as a polymer host matrix. The sensing capability of the nanocomposites by exposing both sensors to vapours of explosive taggants, explosive-like molecules and some common solvents was evaluated. They exhibit a very fast response time of <30s and low LOD. Moreover, the sensor array constitutes a powerful tool to discriminate between explosive taggants (3-nitrotoluene, 4-nitrotoluene and 2,3-dimethyl-2,3-dinitrobutane) and shows specific molecular recognition towards picric acid. The other sensor is based on a nanocomposite of $CsPbBr_3$ nanocrystals (NCs) embedded in a molecularly imprinted polymer (MIP) using 3-nitrotoluene (3-NT) or nitromethane (NM) as template molecules. The straightforward and low-cost molecular imprinting process occurs inside the nanocomposite of $CsPbBr_3$-PCL during the baking step after spin-coating. The sensing capability of the MIP sensors was evaluated and compared to that of the non-imprinted polymer (NIP) by monitoring the photoluminescence (PL) upon exposure to vapours of different explosive taggants, nitro-containing molecules and some organic solvents. The nanocomposite sensors show a fast response time to analytes below 5 s. Moreover, molecular imprinting enhances the PL response of MIP sensors and the specificity to 3-NT. An excellent selectivity towards nitro containing molecules is also exhibited, particularly when NM is used as the template molecule.

In the light of the reported results, this PhD thesis proposes that these sensing platforms are potential candidates for effective explosive detection in the vapour phase.

Resum

Durant l'última dècada, la detecció d'artefactes explosius improvisats (IEDs) tant en l'àmbit militar com civil s'ha convertit en una prioritat estratègica en la seguretat nacional a causa de la creixent amenaça terrorista.

Els explosius es poden classificar segons la seua velocitat de detonació. Així podem distingir entre dos mecanismes d'explosió diferents: deflagració i detonació. El primer dels fenòmens es basa en una reacció de combustió de l'explosiu que s'autopropaga capa per capa i genera una ona subsònica que viatja en la direcció oposada a la dels productes de descomposició de l'explosiu, mentre que el segon es fonamenta en una reacció explosiva que produeix una ona supersònica que es dirigeix en el mateix sentit que els productes de descomposició. Aleshores, segons la velocitat de detonació dels explosius, aquests es classifiquen com propel·lents, els que la seua descomposició es produeix mitjançant una deflagració, i explosius ràpids, els que produeixen una explosió.

A més, la potència dels explosius també pot avaluar-se considerant altres paràmetres termodinàmics com el balanç d'oxigen, el calor d'explosió, el volum de gas alliberat, la potència explosiva i l'índex de potència. El balanç d'oxigen mesura la quantitat d'oxigen necessària per a produir la combustió total de la molècula d'explosiu, és a dir, per a transformar tot el carboni en diòxid de carboni, l'hidrogen en aigua i, en el cas que hi haja metalls, aquests en òxids metàl·lics. Aleshores, un valor positiu indicarà que en la molècula d'explosiu hi ha un excés d'oxigen, un valor zero expressarà que la molècula conté la quantitat exacta i un valor negatiu, que l'oxidació no serà completa i, per tant, podran generar-se gasos tòxics. El calor d'explosió proporciona informació sobre la quantitat d'energia alliberada en la reacció i estarà directament relacionada amb la calor de formació dels productes de descomposició i la calor de formació del propi explosiu. A més a més, el balanç d'oxigen també tindrà una gran influència en el seu valor, aconseguint el seu màxim quan aquest es zero. Un altre paràmetre per a determinar la potència dels explosius es el volum de gasos alliberat en l'explosió ja que, quan major siga aquest, major serà el seu poder destructiu. Finalment, la potència explosiva i l'índex de potència son dos paràmetres que reflecteixen el poder real dels explosius ja que es troben directament relacionats amb la calor d'explosió i el volum de gasos alliberats.

Un gran nombre de molècules explosives presenten un balanç d'oxigen negatiu i, per això, es mesclen amb altres per a incrementar el seu valor i que aquest estiga pròxim a zero, per a així, augmentar la potència explosiva.

Aquest tipus de substàncies, especialment les que contenen grups funcionals nitro, presenten unes pressions de vapor molt baixes. Això provoca que la seua concentració en fase gas es trobe al voltant del nivell de traces o ultratraces. Encara que l'addició de marcadors d'explosius, unes molècules que contenen grups nitro i presenten pressions de vapor moderadament elevades, es obligatòria en tots els explosius comercials per a facilitar la seua detecció, aquesta continua sent difícil. Per això, les tècniques convencionals com la detecció amb gossos o instrumentals com la cromatografia de gasos acoblada a espectrometria de masses o la difracció de raigs X, entre altres, mostren notables avantatges degut a la seua elevada sensibilitat i selectivitat. No obstant això, una gran part d'aquestes presenten inconvenients com per exemple, un manteniment car, processos de mesura lents, instrumentació complexa i voluminosa que limiten el mostreig en continu i en temps real necessari per a aquest tipus d'analits. Per aquesta raó, existeix una recerca constant d'una plataforma de detecció robusta i versàtil que siga adequada per a diferents entorns.

El disseny de sensors portàtils, fàcils de fabricar i de baix cost amb un límit de detecció (LOD) baix, bona selectivitat, alta sensibilitat i un temps de resposta curt és un gran desafiament. El paper de la nanociència ha sigut determinant en gran mesura per al desenvolupament de sensors químics amb un rendiment millorat degut a les seues excel·lents propietats òptiques, catalítiques, elèctriques i electroquímiques. En l'actualitat existeixen una gran varietat de plataformes per al sensat d'explosius i marcadors d'explosius que es basen en l'ús de diferents tipus de nanoestructures però, la gran dificultat per a obtindre una superfície homogènia quan aquestes es depositen sobre un suport sòlid i la baixa volatilitat de les molècules d'explosius, com hem mencionat abans, han produït que un percentatge elevat d'aquests sensors es basen en la detecció d'explosius en fase líquida.

Degut a les propietats redox del nitroderivats els dispositius més emprats per al sensat d'explosius estan basats en mecanismes de transducció electroquímics. No obstant això, la seua utilització està molt limitada a la detecció d'aquestes molècules en dissolució. D'altra banda, el sensors basats en mecanismes de transducció òptics com l'absorbància o la fotoluminescència, a més de mostrar els avantatges que tenen els

sensors electroquímics, poden aplicar-se a la detecció de diferents tipus d'analits en fase vapor.

0.1 Síntesi dels nanocompòsits

En aquesta tesi doctoral, per a obtindre una capa homogènia, i a més millorar l'estabilitat i les propietats mecàniques i tèrmiques dels sensors, es van sintetitzar nanocompòsits híbrids on les nanopartícules es troben embegudes en l'interior d'una matriu polimèrica. Addicionalment, per a millorar tant la selectivitat com la sensibilitat dels nanocompòsits es van emprar mètodes d'impressió molecular per a crear nanocavitats selectives als analits del nostre interès. El mètode d'encapsulació va ser l'escollit per a la generació de les empremtes ja que en el nostre procediment prescindim de l'etapa de polimerització amb la utilització d'un polímer ja sintetitzat.

Aleshores, per a dur a terme la fabricació de les plataformes de sensat es van seguir el següents passos:

- Per començar, es va mesclar en un dissolvent comú el polímer, les nanopartícules i les molècules d'empremta (en el seu cas).
- Tot seguit, es va dipositar sobre un suport sòlid i, mitjançant la tècnica de recobriment per rotació es van formar les capes primes de nanocompòsit.
- Finalment, es va calfar a una temperatura determinada per evaporar tant el dissolvent com les molècules d'empremta i així, generar els llocs de reconeixement molecular, en el seu cas.

Una vegada finalitzat el procés de síntesi, els sensors ja podien ser caracteritzats així com exposats als diferents analits per a avaluar la seua capacitat de detecció.

0.2 Objectiu de la tesi

Aquesta tesi doctoral està presentada com a compendi de tres publicacions, en les quals la introducció de cadascuna d'aquestes ha sigut simplificada i les referències bibliogràfiques s'han indicat de forma conjunta en el capítol 6 per raons de claredat.

En cadascuna d'aquestes es du a terme la síntesi de diferents plataformes òptiques de detecció en estat sòlid basades en un nanocompòsit format per diferents nanopartícules amb propietats òptiques embegudes en una matriu polimèrica, per a dur a terme la

detecció, identificació i quantificació d'alguns explosius, marcadors d'explosius i molècules similars a explosius en fase gasosa.

0.3 Procediment experimental i conclusions

El primer sensor consisteix en un nanocompòsit de nanopartícules de plata (Ag NPs) embegut en un polímer imprés molecularment (MIP). La detecció selectiva de 3-nitrotoluè (3-NT), un marcador explosiu per al 2,4,6-trinitrotoluè, es produirà mitjançant l'absorció de les molècules d'analit sobre la superfície de les nanopartícules de plata, fet que provocarà canvis espectrals mesurables com la longitud d'ona i/o la intensitat màxima de pic de l'espectre de ressonància del plasmó superficial localitzat.

En primer lloc, la síntesi d'un sensor plasmònic basat en un nanocompòsit de nanopartícules de plata (Ag NPs) embegut en un polímer imprés molecularment (MIP) per a la detecció selectiva de 3-nitrotoluè (3-NT), un marcador explosiu per al 2,4,6-trinitrotoluè (TNT). En la nostra estratègia, la síntesi in situ de les nanopartícules de plata i la impressió molecular amb l'empremta de 3-NT, tenen lloc simultàniament dins de la pel·lícula prima de polietilenimina (PEI) durant l'etapa de calfament, després del recobriment per rotació. També es va sintetitzar un polímer no imprés molecularment per a poder comprar els resultats.

Les concentracions de plata i de 3-nitrotoluè van ser optimitzades per a obtindre la major resposta front als analits. De la mateixa manera es va optimitzar el temps i la temperatura de calfament. Degut a que la síntesi de les nanopartícules de plata es realitza in situ, per a confirmar la seua presència en l'interior de la matriu polimèrica, així com també per a conéixer la seua grandària i forma es van emprar diferents tècniques de caracterització. Les mesures d'espectroscòpia UV-Visible es van fer amb un reflectòmetre i el resultat obtingut va determinar una banda d'absorció a 425 nm que es va atribuir a les nanopartícules de plata esfèriques. També es va mesurar amb el microscopi electrònic de transmissió i es va poder confirmar la distribució uniforme de les NPs esfèriques i d'una grandària mitjana de 6,3 ± 1,3 nm per a l'Ag-PEI MIP i 6,2 ± 1,1 nm per al NIP. Tant els resultats proporcionats pel difractòmetre de raigs X (DRX) com pel microscopi de electrònic de transmissió d'alta resolució (HRTEM) van servir per corroborar els resultats anteriors. L'estructura orgànica del sensor es va estudiar mitjançant un espectre d'infraroig (FTIR) on es van observar els grups característics del PEI i,

finalment, per a conéixer la morfologia del MIP es va realitzar un estudi amb el microscopi de força atòmica (AFM) observant una estructura plana i homogènia.

La capacitat de sensat químic dels nanocompòsits MIP i NIP d'Ag-PEI cap al 3-NT es va demostrar mitjançant l'exposició dels sensors a un flux de vapor d'aigua contenint una concentració de 3-NT de 13,7 µg/mL a temperatura ambient i per a diferents temps de sensat. Açò es va aconseguir amb el bombolleig d'una dissolució aquosa de 3-NT 10^{-4} M emprant aire com a gas portador. L'adsorció de les molècules de 3-nitrotoluè sobre la superfície de les nanopartícules estava determinada pel transport de l'analit en fase vapor cap a aquestes i la posterior velocitat d'interacció química. Per a avaluar la resposta d'ambdós sensors es va monitoritzar la disminució de la intensitat de la banda de ressonància de plasmó superficial localitzada. El mètode d'impressió molecular va proporcionar una millora de la resposta del LSPR cap al 3-NT en comparació amb el NIP obtenint un LOD de 1,37 ng/mL i una sensibilitat de 24,0 ± 3,0%. Aquest resultat va confirmar que el mecanisme de impressió molecular sensibilitat i la selectivitat del sensor cap al 3-NT. Per a avaluar la selectivitat del sensor MIP, aquest va ser exposat als vapors de diferents molècules amb grups funcionals NO_2 com el 2,3-dimetil-2,3-dinitrobutà (DMDNB), àcid pícric (PA) i 4-nitrofenol (4-NP). Els resultats van demostrar l'elevada especificitat cap al 3-NT.

Aleshores, amb aquest treball vam poder confirmar que els sensors MIP d'Ag-PEI es poden emprar com a sensors òptics plasmònics en la detecció de 3-NT. Encara que el temps de resposta es elevat, aquests poden ser emprats en certes aplicacions on aquest paràmetre no es limitant, com per exemple, com a sentinel·les en vaixells de càrrega.

Com a resultat es va obtindre un sensor plasmònic que, a més de ser fàcil de preparar i d'utilitzar, barat, robust, sensible, selectiu i versàtil, es pot implementar fàcilment com un dispositiu de lectura portàtil en robots remots de detecció d'explosius i eliminació de bombes.

En la segona part, s'han emprat sensors químics que contenen nanopartícules fluorescents com els punts quàntics (QDs) i les perovskites d'halogenurs metàl·lics (PVKs) degut a les seues excel·lents propietats òptiques i electròniques.

Aleshores, un dels sensors consisteix en un sistema que conté punts quàntics de selenur de cadmi (CdSe) de diferents grandàries que emeten llum verda o roja i es troben embeguts en una matriu polimèrica de policaprolactona (PCL). El mecanisme de transducció del sensor està basat en els canvis en la intensitat d'emissió de

fotoluminescència dels punts quàntics quan els analits interaccionen amb la seua superfície.

En aquest cas es van preparar dos dissolucions diferents contenint policaprolactona i punts quàntics de color roig o verd. Aleshores, ambdós sensors es van sintetitzar mitjançant el recobriment per rotació després d'haver depositat sobre el substrat sòlid una xicoteta quantitat de dissolució. Finalment, en l'etapa de calfament únicament es va produir l'evaporació del dissolvent ja que en aquest sistema de sensat no s'ha emprat la tecnologia de impressió molecular.

La caracterització òptica d'ambdós sensors es va dur a terme amb la mesura de l'absorbància i la fotoluminescència dels punts quàntics tant en dissolució com formant la capa prima sobre el suport sòlid. Així es va comprovar que les característiques d'aquests es modificaven notablement amb la formació del nanocompòsit, fet que es va atribuir a una disminució de l'índex de refracció efectiu que envolta els punts quàntics causat per la porositat de la matriu polimèrica. La mesura de les dimensions de les nanopartícules amb el microscopi electrònic de transmissió va indicar que la distribució de grandàries romania constant quan aquests s'embevien en la matriu polimèrica. Finalment, amb el microscopi electrònic d'escombratge es va observar que la superfície dels sensors era homogènia i plana.

Per avaluar la capacitat de detecció d'ambdós nanocompòsits, aquests es van exposar, durant intervals de temps diferents, als vapors de 0,2 g de marcadors explosius, molècules semblants als explosius o alguns dissolvents comuns en un recipient de 100 mL tancat a temperatura ambient. La mesura de la fotoluminescència es va dur a terme amb un sistema de mesura casolà on el feix del làser es feia incidir sobre els sensors i la senyal era recollida mitjançant un espectrofotòmetre.

Els resultats obtinguts van demostrar l'elevada capacitat de resposta d'ambdós sensors cap al 3-nitrotoluè ja que l'exposició durant 30 segons a aquest analit va provocar un increment significatiu de la senyal de fotoluminescència (un 138,2 % en el cas del CdSe verd i un 165,6 % en el cas del CdSe roig). En aquest cas, l'adsorció de les molècules d'analit sobre la superfície dels punts quàntics està determinada per la difusió de l'analit en fase vapor cap al sensor i la velocitat d'interacció química.

També es va comprovar si els sensors podien ser reutilitzats. Per a això, cada cicle de sensat consistia en l'exposició de cadascun dels sensors a un flux de 3-NT durant 240 s seguit d'un cicle de recuperació on els sensors es calfaven a 100ºC durant 240 s. Els

resultats obtinguts van demostrar que mentre que el sensor de CdSe verd sofria una degradació en les successives etapes de calfament i, per consegüent, una disminució en la fotoluminescència, el sensor de CdSe roig experimentava un augment de senyal degut a una incompleta eliminació de l'analit en l'etapa de calfament.

La selectivitat dels sensors es va examinar mitjançant l'exposició d'aquests a diferents analits com marcadors d'explosius (3-NT, 4-NT, DMDNB), altres molècules que contenen grups NO_2 (4-NP, 5-NI, 1-NN, NM, PA) i alguns dissolvents (hexà, toluè, acetona, acetonitril, metanol, i aigua). Es va observar que tant la resposta del sensor amb CdSe verd com la de CdSe roig cap als marcadors explosius i les molècules que contenen grups funcionals nitro era considerablement major que cap als dissolvents. Com que en aquest cas no vam emprar la tècnica de la impressió molecular, els resultats van indicar que ambdós nanocompòsits van interaccionar amb una major selectivitat amb els compostos nitroderivats. A més a més, cadascun dels sensors van mostrar respostes diferents quan foren exposats als vapors dels diferents analits. A partir d'aquests resultats, es va estudiar l'habilitat de la plataforma de sensat per a dur a terme un anàlisi multiparamètric. Llavors, es van monitoritzar els canvis de fotoluminescència dels sensors i després es va representar la resposta d'aquests a un temps determinat. Açò ens va permetre identificar la formació de tres grups d'analits diferents en un mapa bidimensional. El primer grup estava format pels analits que havien provocat un menor canvi de senyal en ambdós sensors, els dissolvents. El segon el formaven els analits amb una major interacció amb el sensor que contenia punts quàntics verds (DMDNB, 4-NT and 4-NP), mentre que el tercer i últim grup estava constituït pels analits que havien interaccionat més fortament amb el sensor amb punts quàntics rojos (NM, 1-NN, PA, 3-NT and 5-NI). Per tant, aquests resultats van demostrar aquesta plataforma de sensat tenia la capacitat per a poder discriminar entre els diferents marcadors d'explosius. Finalment, també es va estudiar el límit de detecció per a alguns marcadors d'explosius obtenint resultats molt baixos, com per exemple de 10 pM en el cas del 3-NT.

Per tant, a la llum dels resultats es va concloure que la matriu de sensat presenta un temps de resposta molt ràpid (menor a 30 s) i un límit de detecció baix per als marcadors d'explosius. A més, l'anàlisi multiparamètric permet discriminar entre les molècules de 3-nitrotoluè, 4-nitrotoluè i 2,3-dimetil-2,3-dinitrobutà per a així minimitzar els falsos positius i així, podria constituir una poderosa eina per a la identificació i quantificació d'aquestes substancies tant abans com després d'una explosió.

L'altre sensor es basa en un nanocompòsit de nanocristalls (NCs) de perovskita de tribromur de cesi i plom ($CsPbBr_3$) embeguts en una matriu polimèrica de policaprolactona impresa molecularment que utilitza 3-nitrotoluè o nitrometà (NM) com a molècules empremta. En aquest cas el mecanisme de transducció generalment està basat en la disminució de la intensitat d'emissió de fotoluminescència de les nanopartícules quan els analits interaccionen amb la seua superfície. Aquest canvi por ser degut a una transferència electrònica entre les perovskites (donadores d'electrons) i les molècules d'analit (acceptors d'electrons) degut a la forta capacitat d'atracció d'electrons dels grups NO_2. No obstant això, el mecanisme encara no es coneix de forma exacta.

En primer lloc es va dur a terme la síntesi i purificació dels nanocristalls de perovskita. Aquests es van preparar amb el mètode de injecció en calent en atmosfera de nitrogen on en un matràs es trobava el carbonat de cesi, la oleilamina i l'1-octadecè i, en l'altre, el bromur de plom (II) dissolt en 1-octadecè. Aleshores, una vegada ambdós dissolucions estaven a la temperatura adequada, la dissolució amb cesi es va injectar ràpidament sobre la que contenia plom per a, finalment, refredar el matràs de reacció en un bany de gel. La purificació dels nanocristalls va consistir en etapes successives de centrifugació i redispersió amb una mescla d'hexà i acetat d'etil.

Seguint el mateix procediment que en el cas dels punts quàntics, es van preparar dos dissolucions diferents contenint policaprolactona, els NCs de $CsPbBr_3$ i les molècules empremta de 3-nitrotoluè o nitrometà. Com en el cas del sensor d'Ag-PEI, també es va preparar un sensor no imprés molecularment per a poder comprar el resultats obtinguts. Aleshores, la síntesi d'ambdós sensors es va dur a terme mitjançant la deposició de la dissolució sobre un suport sòlid i el posterior recobriment d'aquest per rotació. Finalment, la síntesi va acabar en una etapa de calfament en la que es va evaporar tant el dissolvent com les molècules empremta deixant així unes nanocavitats específiques per als analits de interés.

Les tècniques de caracterització que es van utilitzar van ser l'espectroscòpia UV-Vis, així com la fotoluminescència per a mesurar les propietats òptiques de les nanopartícules tant en dissolució com quan es troben formant el nanocompòsit. Els resultats obtinguts van demostrar un espectre d'absorbància diferent, fet que es va atribuir a la porositat del polímer quan no es troba en dissolució. D'altra banda, la semblança entre els espectres de fotoluminescència va ser indicativa d'una dispersió homogènia de les nanopartícules. Per a analitzar la forma, la grandària i comprovar la distribució uniforme dels nanocristalls

es va mesurar amb el microscopi electrònic de transmissió. Això va revelar una morfologia cúbica i unes dimensions al voltant de 7,2 nm en tots els casos. Els resultats obtinguts amb la difracció de raigs X i amb el microscopi electrònic de transmissió d'elevada resolució van confirmar els indicats anteriorment. L'estudi de l'estructura orgànica del nanocompòsit, així com la constatació de l'eliminació total de les molècules d'empremta es va realitzar amb l'espectrofotòmetre d'infraroig. Per acabar, la morfologia del NIP i d'ambdós MIPs es va mesurar amb el microscopi electrònic d'escombratge obtenint uns resultats de rugositat molt majors per als sintetitzats amb molècules d'empremta que per a l'altre, fet que va suggerir que el procediment s'havia desenvolupat de manera satisfactòria.

La capacitat de detecció dels sensors de $CsPbBr_3$-PCL es avaluar i comparar amb la del polímer no imprés molecularment mitjançant la monitorització de la fotoluminescència (PL) després de l'exposició d'aquests a un flux constant de vapors de diferents marcadors d'explosius, molècules amb grups nitro i alguns dissolvents orgànics emprant una bomba peristàltica i aire com gas portador. La intensitat de senyal es va mesurar de forma continua en un sistema casolà on, de la mateixa forma que en els punts quàntics, el feix del làser es feia incidir sobre els nanocompòsits i la resposta era recollida mitjançant un espectrofotòmetre.

D'igual forma que en el sensor format per nanopartícules de plata, l'adsorció de les molècules de 3-nitrotoluè sobre la superfície dels nanocristalls va estar determinada pel flux d'analit en fase vapor cap al sensor i la posterior velocitat d'interacció química. Així i tot, els sensors van demostrar un temps de resposta extraordinàriament ràpid cap al 3-nitrotoluè on després de 120 s d'exposició la intensitat de senyal dels sensors MIP s'havia reduït un 69% i la del NIP ho havia fet un 53%.

A pesar del baix cost i la senzillesa per a fabricar els sensors, també es va fer un estudi de reversibilitat del sensat. Així, en cada cicle el sensor va ser exposat a un flux de 3-nitrotoluè durant 60 s seguit de l'exposició a un flux d'aire durant altres 60 s. Els resultats obtinguts després d'una sèrie de cicles van demostrar que mentre que el NIP recuperava quasi tot el senyal inicial, ambdós polímers impresos molecularment mostraven una tendència decreixent. Això podia ser degut a l'increment de porositat i permeabilitat generat en els polímers impresos molecularment, fet que provocava una eliminació incompleta de les molècules d'analit sobre la superfície del sensor.

Per conéixer la capacitat de sensat de tots els nanocompòsits, aquests es van analitzar mitjançant un cromatògraf de gasos acoblat a un detector d'ionització de flama (GC-FID). En primer lloc es va dur a terme un anàlisi previ al sensat per a comprovar que l'eliminació de les molècules empremta havia sigut efectiva, tal com ens havia indicat l'espectre d'infraroig, i així no tindre un error per excés. Una vegada confirmada l'eliminació total del 3-NT i el NM, els diferents sensors es van exposar als vapors de 3-nitrotoluè durant 180 segons i després es van dissoldre en cloroform i es van injectar en el cromatògraf de gasos. Els resultats obtinguts van indicar una major capacitat d'adsorció per al sensor de NM, seguit pel MIP amb 3-nitrotoluè i, finalment, el NIP.

El límit de detecció també va ser determinat per al 3-nitrotoluè obtenint un resultat al voltant d'1,59 µM. Per acabar, la selectivitat dels sensors NIP, 3-NT MIP i NM MIP es va avaluar mitjançant l'exposició d'aquests als vapors de diferents analits com marcadors d'explosius (3-NT, 4-NT, DMDNB), molècules que contenen grups funcionals nitro (4-NP, 5-NI, 1-NN, NM) i alguns dissolvents comuns (toluè, acetona, acetonitril, metanol, i acetat d'etil), d'igual manera que s'havia fet amb els punts quàntics. Així, es va observar que els sensors impresos molecularment experimentaven una major interacció amb els marcadors d'explosius i les altres molècules nitroderivades, particularment quan s'empra NM com a molècula d'impressió.

Aleshores, després d'analitzar els resultats obtinguts es va concloure que els sensors mostren un temps de resposta ràpid cap als analits (per davall dels 5 s). A més a més, el procés d'impressió molecular va proporcionar un increment en la resposta i una millora de la selectivitat degut a la interacció més específica amb els marcadors explosius i les molècules amb grups funcionals nitro que amb els dissolvents comuns. Particularment, el sensor imprés molecularment amb nitrometà és el que va exhibir una major resposta cap als nitroderivats, fet que va confirmar la correcta generació dels llocs de reconeixement molecular, permetent una ràpida detecció del 3-nitrotoluè (al voltant de 2 s) amb un límit de detecció de 0,218 µg/mL.

A la llum de tots els resultats reportats, aquesta tesi doctoral proposa que aquestes plataformes de detecció són unes candidates potencials per a la detecció, identificació i quantificació efectiva d'explosius en fase vapor degut a l'elevada selectivitat i el baix límit de detecció mostrat. A més a més, proporcionen un temps de resposta adequat per a la seua utilització en diverses aplicacions i degut la grandària, robustesa i versatilitat de les plataformes de sensat, poden incorporar-se en sistemes portàtils que permeten l'anàlisi en temps real.

Capítol 1

Introducció

En els últims anys, la creixent amenaça d'un atac terrorista amb explosius ha incrementat la necessitat de desenvolupar tecnologies per a detectar-los de manera ràpida i fiable. No obstant això, aquests materials solen estar empaquetats, ocults o en concentracions molt baixes, la qual cosa limita la capacitat de detecció. Per tant, el desenvolupament de mètodes de detecció efectius per a identificar i quantificar compostos explosius en escenaris molt diferents, com contenidors, vehicles o equipatge, són essencials.

Per això, el principal objectiu d'aquesta tesi doctoral és la recerca y el desenvolupament de diferents plataformes de sensat basades en sistemes de transducció òptics que a més de ser capaços de detectar de forma selectiva i reproduïble traces de molècules d'explosius o marcadors d'explosius amb un temps de resposta adequat, es puguen incorporar a sistemes portàtils que permeten l'anàlisi en temps real.

1.1 Materials explosius

Un explosiu es pot definir com un dispositiu, un compost químic o una mescla de diferents compostos capaços de produir una explosió. Això és, una reacció química extremadament exotèrmica i ràpida deguda a la generació de grans quantitats de calor i pressió, generalment produïdes per la formació de gasos a partir de la descomposició de l'explosiu, amb una ràpida expansió de la matèria en un període molt curt de temps.[1] No obstant això, els explosius no poden patir una descomposició sense alguns estímuls externs que inicien el procés. Per això, són molt sensibles a l'impacte, fricció, xoc o qualsevol aplicació d'un simple pols d'energia.[2,3] La majoria dels explosius contenen oxigen i nitrogen en major proporció que altres compostos orgànics, i a més, compostos oxidables (combustibles) com carboni, hidrogen i metalls.[4] Durant la reacció de descomposició, el nitrogen i l'oxigen reaccionen amb els combustibles generant principalment CO/CO_2, H_2O i N_2 (Esquema 1).

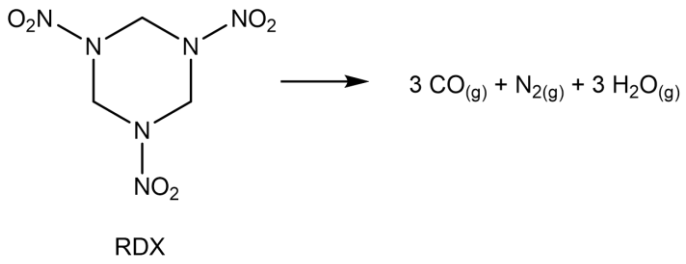

Esquema 1. Reacció química de detonació de la ciclotrimetilentrinitramina (RDX).

1.2 Aspectes històrics

En aquesta part del capítol, ens centrem en una descripció general d'alguns dels desenvolupaments i aplicacions més rellevants dels explosius (Figura 1).

La pólvora negra va ser el primer explosiu conegut. Va ser descobert accidentalment per uns alquimistes xinesos l'any 220 a. C., però no va ser introduït a Europa fins 1249 quan el científic Roger Bacon va mesclar salpetre (nitrat de potassi, oxidant) amb carbó i sofre (combustibles), com es mostra a l'Esquema 2. A partir d'aleshores, molts països van utilitzar la pólvora negra per a qüestions militars.

$$8\ C + 3\ S + 10\ KNO_3 \rightarrow 3\ K_2SO_4 + 2\ K_2CO_3 + 6\ CO_2 + 5\ N_2$$

Pólvora negra

Esquema 2. Esquema de reacció de la descomposició de la pólvora negra.[5]

En 1846, el químic italià, Ascanio Sobrero, va sintetitzar la nitroglicerina líquida però degut al seu caràcter explosiu va abandonar els seus estudis. Així i tot, en 1863, Alfred Nobel i el seu pare van desenvolupar un procés de fabricació de nitroglicerina (NG) que consistia a afegir glicerina a una mescla freda d'àcids nítric i sulfúric altament concentrats sota agitació contínua. Finalment, la nitroglicerina es llavava amb aigua i una solució alcalina per a eliminar les restes d'àcid. Degut a la seua alta sensibilitat als colps i la iniciació impredictible de la pólvora negra van tindre alguns inconvenients en el procés de fabricació. En 1864, una explosió va destruir la fàbrica i va matar a cinc persones, inclòs el germà d'Alfred, Emil. El mateix any, Alfred Nobel va inventar el detonador que contenia fulminat de mercuri ($Hg(CNO)_2$) per a reemplaçar a la pólvora negra com a iniciador. En 1866, es va centrar en desenvolupar un mètode per a reduir la reactivitat de la nitroglicerina, després que una altra explosió accidental destrossara tota la fàbrica. Per a això, van mesclar nitroglicerina (75%) amb un material adsorbent basat en terra de diatomees o diatomita (Kieselguhr, 25%) obtenint així un sòlid molt més segur de manipular i més fàcil d'usar, que va ser patentat en 1867 com “Ghur Dynamite”.[6]

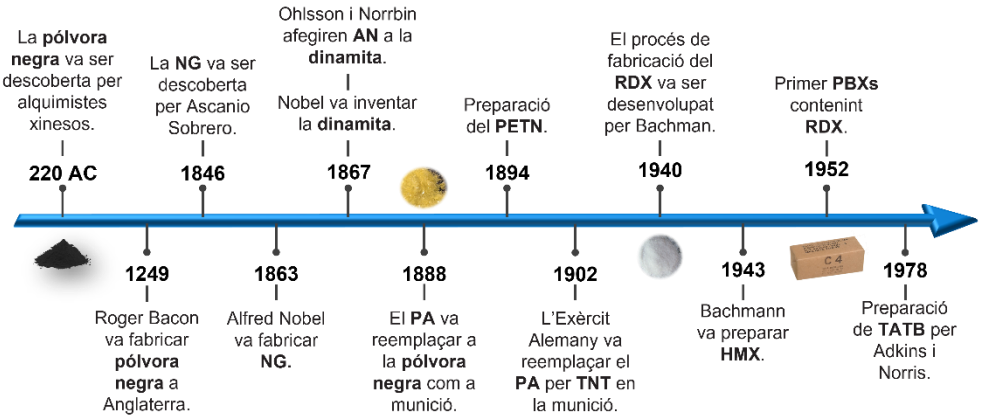

Figura 1. Cronologia del descobriment d’alguns explosius importants.

Encara que el nitrat d'amoni (AN) no estava considerat com un explosiu, en 1867, els químics suecs Ohlsson i Norrbin es van adonar que les propietats explosives de la dinamita es milloraven amb l'addició de nitrat d’amoni i, després d'això, Nobel ho va

incorporar en el seu procés de fabricació. Al mateix temps, la nitració de la cel·lulosa per a obtindre nitrocel·lulosa (NC) va ser realitzada per Schönbein i Böttger i, en 1875, Alfred Nobel va descobrir que la mescla de nitroglicerina amb nitrocel·lulosa formava un gel que podia emprar-se per a produir gelatina explosiva, però únicament va ser utilitzada en l'àmbit civil.

En 1888, l'àcid pícric (PA) va reemplaçar a la pólvora negra per a usos militars en granades i mines terrestres a causa de la sensibilitat de les seues sals metàl·liques als colps. El desenvolupament del "tetril" va ocórrer al mateix temps que l'àcid pícric, però fins 1906 no es va emprar com a explosiu.

La síntesi del 2,4,6-trinitrotoluè (TNT) pur que va dur a terme Hepp en 1880 i el seu posterior desenvolupament com a compost explosiu en 1899, va reemplaçar l'ús d'àcid pícric en operacions militars. La seua fabricació consisteix en tres passos successius de nitració del toluè mesclant-lo amb una mescla d'HNO_3 i H_2SO_4 (Esquema 3). Va ser l'explosiu estàndard durant la Primera Guerra Mundial però, a causa de l'escassesa de toluè per a produir TNT, es va popularitzar una mescla de TNT amb AN (amatol) per al farciment d'armes militars.[7,8]

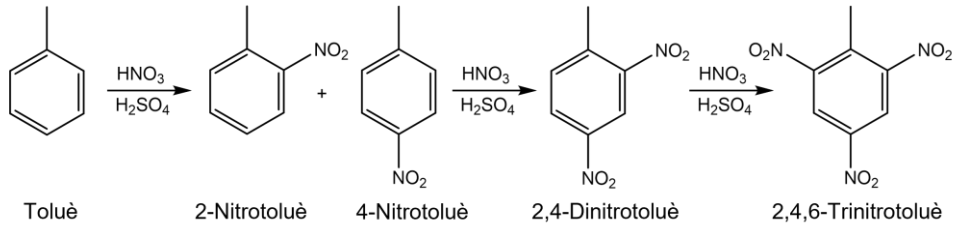

Esquema 3. Preparació del 2,4,6-trinitrotoluè (TNT).

Encara que els explosius més comuns en la Segona Guerra Mundial van ser l'hexogen (RDX) i el tetranitrat de pentaeritritol (PETN), la seua primera aplicació (i també de la NG) va ser per a tractar problemes de salut com a vasodilatador. El RDX va ser l'explosiu més utilitzat degut a l'alta sensibilitat a l'impacte i la baixa estabilitat química del PETN. Aquest últim es va utilitzar en mescles de PETN-TNT en proporció 1:1 (pentolita) per a granades i detonadors, però finalment també va ser reemplaçat pel RDX. Al final de la Segona Guerra Mundial, l'octogen (HMX), obtingut com una impuresa del procés de fabricació del RDX descrit per Bachman, va començar a estar disponible.[9]

Amb la finalitat de reduir la sensibilitat d'explosius com el RDX, HMX i PETN i millorar les seues propietats mecàniques i processament, aquests es van embeure en una matriu

polimèrica elàstica gomosa (aglutinant) constituint els explosius en pols aglutinats (PBX). El primer PBX es va sintetitzar en 1952 als Estats Units d'Amèrica (EUA) i consistia en cristalls de RDX embeguts en poliestirè plastificat. Els aglutinants son seleccionats en funció de la reactivitat dels explosius. Per exemple, els polímers inerts com el tefló es trien per a explosius altament reactius. En alguns casos, també es necessita l'addició d'un plastificant per a millorar el processament i reduir la reactivitat del PBX. Els PBXs més coneguts són el "Semtex" (PETN + cautxú + plastificant) i "Composició C-4" (RDX + poliisobutilè + dioctilsebacat + material oliós).[10]

Des de l'any 1955, el desenvolupament de l'ANFO (Ammonim Nitrate – Fuel Oil, mescla de nitrat d'amoni i combustible derivat del petroli), els gels d'aigua ("slurries"), les emulsions i els explosius de voladura han provocat una reducció en el preu dels explosius per a ús civil. Entre altres desenvolupaments explosius recents, l'hexanitrostilbè (HNS, Shipp en 1966) i el triaminotrinitrobencè (TATB, Norris i Atkins en 1978) van ser de gran interès per la seua extraordinària estabilitat tèrmica i baixa sensibilitat a estímuls externs.[11]

Un dels explosius més moderns són els peròxids orgànics. Es basen en el grup funcional (-O-O-) dels peròxids. Aquesta estructura bivalent pot proporcionar suficient oxigen per a una ràpida autooxidació i explosió. No obstant, la seua alta sensibilitat a la calor, els colps i la fricció combinats amb l'alta pressió de vapor, en comparació amb els explosius nitroderivats, els fa extraordinàriament inestables, impredictibles i molt perillosos per al seu maneig.[12,13,14] Com a resultat, el nombre d'aplicacions és molt limitat.

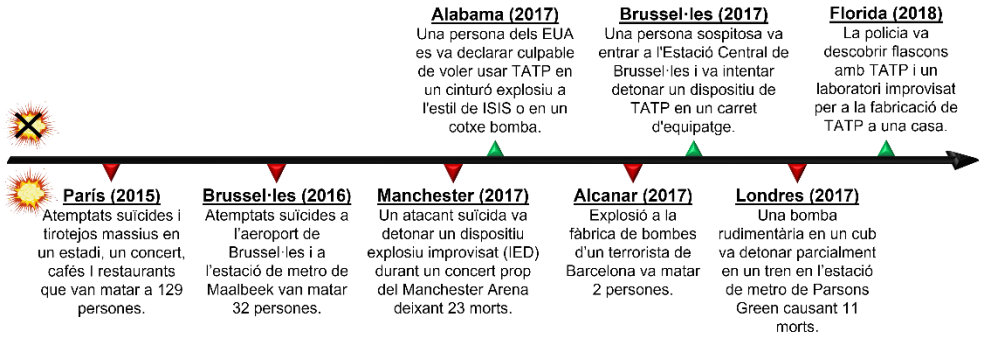

Figura 2. Alguns exemples d'atacs terroristes exitosos i avortats que fan ús del TATP.[15]

Malgrat això, en les últimes dues dècades, els peròxids orgànics com el triperòxid de triacetona (TATP) i l'hexametilè triperòxid de diamina (HMTD) han centrat l'atenció a

causa del seu ús en atemptats terroristes a Europa i els Estats Units, entre d'altres (Figura 2). Per la seua reactivitat, tots dos poden ser utilitzats com a càrrega principal o iniciador.[16,17]

El TATP, també conegut com a la "Mare de Satanàs", va ser descobert pel químic alemany Richard Wolffenstein en 1895. És un explosiu casolà amb quasi el mateix poder destructiu que el TNT, però que es pot sintetitzar fàcilment mesclant acetona amb peròxid d'hidrogen altament concentrat usant H_2SO_4, HCl o HNO_3 com a catalitzador àcid. El producte precipita en un sòlid cristal·lí inestable que pot sublimar a temperatura ambient.[18] No obstant això, depenent del pH i de les concentracions del reactiu també es pot obtindre diperòxid de diacetona (DADP) com a producte secundari (Esquema 4A).[19,20,21]

L'HMTD, també conegut com a peròxid d'amina, va ser sintetitzat per Ludwig Leger en 1885 a partir de la reacció de l'amoníac amb els productes de la combustió de l'èter. També és un explosiu casolà que es pot preparar a partir de la mescla d'hexamina (HXM) i peròxid d'hidrogen en presència d'un catalitzador àcid orgànic o inorgànic com l'àcid cítric (Esquema 4B).[22,23] Encara que l'HMDT és menys potent que el TATP, aquest és més sensible, inestable i difícil de detectar a causa de la seua baixa pressió de vapor.[24]

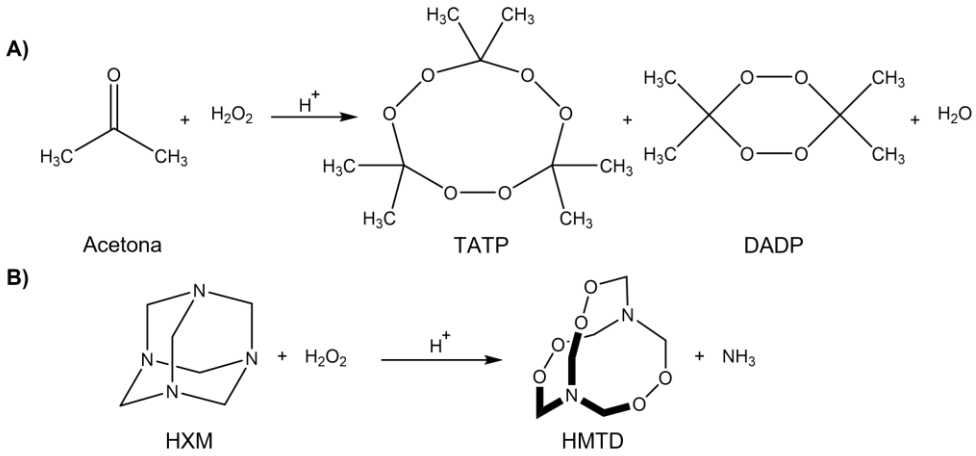

Esquema 4. A) Síntesi del TATP a partir d'acetona i peròxid d'hidrogen i B) Síntesi de l'HMTD a partir d'hexamina i peròxid d'hidrogen.

A més dels peròxids orgànics, altres explosius nitroderivats tant casolans com comercials s'han utilitzat en atemptats terroristes. Per exemple, l'ANFO es va utilitzar en els atemptats terroristes de la ciutat d'Oklahoma en 1995 i a Oslo en 2011, així com la

dinamita (Goma-2)[25] va ser la triada per a Al-Qaeda en els atemptats del tren de Madrid en 2004.[16]

1.3 Mecanismes de descomposició dels explosius

1.3.1 Velocitat de detonació (VOD)

La velocitat de detonació es defineix com l'ona de detonació que viatja a través de l'explosiu. Aquest paràmetre mesura la potència de l'explosiu i és directament proporcional a la seua densitat, grau de confinament, força d'iniciació i diàmetre.[26]

Generalment, és possible distingir entre combustió (no explosiu) i dos mecanismes d'explosió diferents (Figura 3A). Quan s'inicia la descomposició explosiva, aquests poden cremar-se (deflagració) o explotar (detonació).[27]

1.3.1.1 Combustió

La combustió es defineix com una reacció d'oxidació ràpida i exotèrmica que allibera grans quantitats de gas a altes temperatures en un llarg període de temps. Alguns explosius poden cremar-se sense explotar degut a que contenen ambdós molècules combustibles (combustible i oxidant), com s'havia mencionat anteriorment. Així i tot, depenent de la substància explosiva i el temps de reacció, la generació de calor i gasos pot donar lloc a processos de deflagració o detonació. Per exemple, quan es crema 1 kg de carbó, pot alliberar al voltant de 32660 kJ de calor, que és un nombre molt major a la calor alliberada per 1 kg de TNT. Ara bé, mentre que la combustió del carbó tarda més de 3600 s, el temps de descomposició del TNT és de 0,00001 s, experimentant, per tant, una explosió.

1.3.1.2 Deflagració

La deflagració es defineix com una reacció en la qual la velocitat del front de reacció a través del material sense reaccionar no arriba a la velocitat del so en l'estat sòlid o líquid (generalment 1000-3000 m/s) creant un front d'ona subsònica. La deflagració s'inicia quan una xicoteta quantitat d'explosiu s'encén després de l'exposició a una flama, espurna o xoc i es crema capa per capa. Cada partícula en la superfície conté l'oxigen necessari per a cremar i generar calor i gasos que afecten les partícules adjacents

iniciant una descomposició mitjançant un procés d'auto-propagació. Encara que aquest és un mecanisme relativament lent controlat pel ràtio de transferència de calor (conducció, convecció i radiació), quan els explosius estan confinats, la formació progressiva de compostos volàtils causarà una explosió (Figura 3B). La direcció de propagació de la deflagració és l'oposada a la direcció dels productes de descomposició de l'explosiu.

1.3.1.3 Detonació

La detonació es defineix com una reacció en la qual la velocitat de propagació del front de detonació és superior a la velocitat del so a través del material que no ha reaccionat, creant una ona de xoc supersònica, que normalment supera els 4000 m/s. El mecanisme està controlat per la velocitat a la qual el material transmetrà l'ona de xoc i, a diferència dels anteriors, aquests no necessiten trobar-se confinats per explotar. Els productes de descomposició i l'ona de xoc avancen en la mateixa direcció.

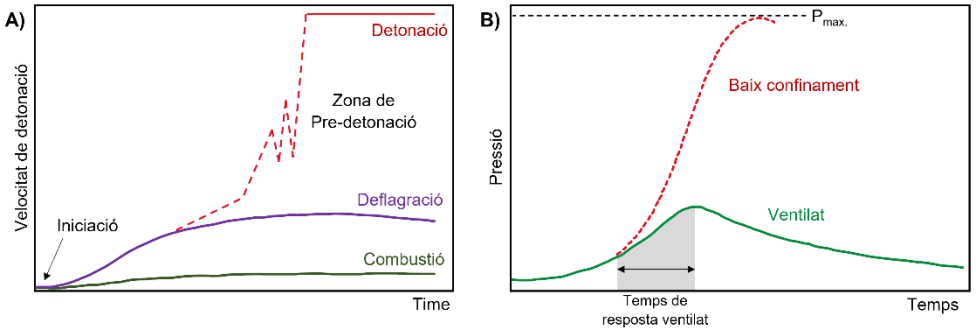

Figura 3. A) Mecanismes d'explosió considerant la VOD. B) Gràfic pressió-temps del mecanisme de deflagració.[28]

1.4 Classificació dels explosius

1.4.1 En funció de la composició química i les aplicacions

Les substàncies explosives (Figura 4) es poden classificar en sis àmplies categories d'acord amb la seua composició química i les seues aplicacions. Compostos nitro-alifàtics com el nitrometà (NM), nitro-aromàtics com el 2,4,6-trinitrotoluè (TNT) o el tetril, que són els principals components dels explosius amb finalitats militars i de les mines terrestres que encara es troben sense explotar. Nitramines com la

ciclotrimetilentrinitramina (RDX) i èsters de nitrat com el tetranitrat de pentaeritritol (PETN), que són els principals components dels explosius plàstics per a l'enginyeria civil i militar, i s'utilitzen, per exemple, en la demolició d'edificis i l'excavació en les mines.

Sals àcides com el nitrat d'amoni (AN) i el fosfat d'amoni (AP) que s'usen freqüentment per a aplicacions industrials i explosius a base de peròxid com el peròxid de triacetona (TATP) i l'hexametilè triperòxid de diamina (HMTD) que han evolucionat ràpidament com a explosius casolans per la seua facilitat de síntesi, com s'havia esmentat abans.[29,30,31,32] No obstant, aquesta classificació no proporciona informació sobre la velocitat de descomposició química, així com tampoc de la quantitat de gas i calor alliberada.

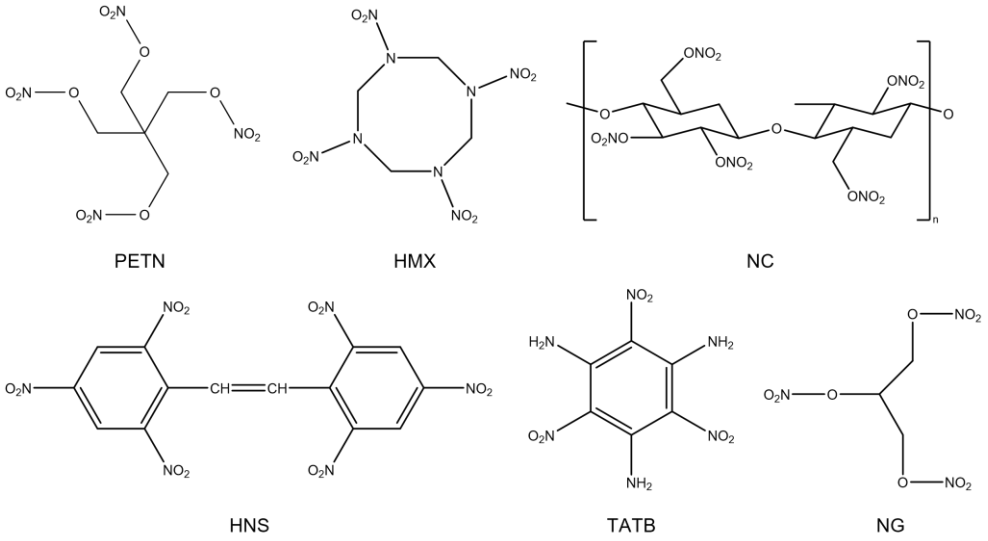

Figura 4. Estructura química d'alguns explosius comuns.

1.4.2 En funció de la VOD

En conseqüència, els explosius també poden classificar-se com a explosius lents o ràpids segons la VOD (Taula 1). Els explosius lents o propel·lents són compostos químics que es caracteritzen pel fenomen de la deflagració. La pólvora, la pólvora sense fum i els propulsors d'armes són els explosius lents més comuns.

Els explosius ràpids consisteixen en diferents tipus de materials que detonen. Segons la seua estabilitat, es divideixen en tres categories diferents.[9,33]

Els explosius primaris o iniciadors són molt sensibles a qualsevol estímul extern i tenen la capacitat de transmetre la calor o xoc produït en la seua ignició o detonació per una metxa o cable a explosius menys sensibles (Figura 5).

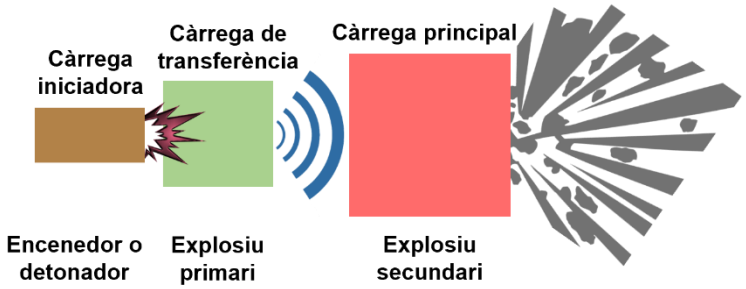

Figura 5. Representació esquemàtica de la detonació d'un material explosiu.

Per això, s'utilitzen en xicotetes quantitats com a iniciadors d'explosius més estables. La seua velocitat de detonació es troba en el rang de 3500-5500 m/s. L'azida de plom, el fulminat de mercuri, l'estifnat de plom o la nitroglicerina són alguns exemples d'explosius primaris. La reacció de descomposició del fulminat de mercuri es mostra en l'Esquema 5.

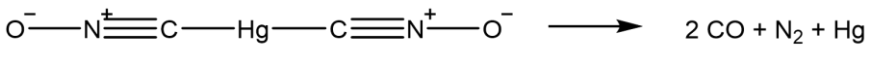

Fulminat de mercuri

Esquema 5. Reacció de detonació del fulminat de mercuri.

Els explosius secundaris són bastant insensibles als estímuls tèrmics i mecànics i requereixen un iniciador per a explotar però, generalment, tenen un efecte de destrucció major que els explosius primaris. La majoria d'ells són molècules alifàtiques i aromàtiques que contenen grups nitro (NO_2). El fort caràcter d'extracció d'electrons (oxidant) dels grups NO_2 dóna com a resultat explosius extraordinàriament potents. A més, després de la detonació, els propis grups NO_2 proporcionen l'oxigen essencial per a la combustió dels anells aromàtics generant CO_2 i els àtoms de nitrogen es transformen en N_2 augmentant així el volum de gas produït. Els altres explosius són peròxids orgànics, que contenen l'enllaç O-O com a font d'oxigen per a una ràpida auto-oxidació i detonació. La velocitat de detonació dels explosius secundaris es troba entre 5500 i

9500 m/s. Alguns d'aquests explosius s'utilitzen en l'àmbit militar com el 2,4,6-trinitrotoluè (TNT), la ciclotrimetilentrinitramina (RDX) o el tetranitrat de pentaeritritol (PETN).

Els explosius terciaris o agents de voladura són compostos insensibles en els quals l'inici de la descomposició degut a una flama, xoc o fricció és més difícil que altres explosius de gran potència. Són principalment oxidants que, combinats amb la proporció exacta de combustible, poden alliberar grans quantitats d'energia. Alguns exemples són el nitrat d'amoni o el perclorat d'amoni.

Taula 1. VOD d'alguns materials explosius.[11,14,33,34]

	Substància explosiva	Densitat ($g \cdot cm^{-3}$)	VOD ($m \cdot s^{-1}$)
Propulsor	Pólvora negra	-	400-500
Explosiu primari	Fulminat de mercuri	3,3	4480
	NG*	1,6	7700
Explosiu secundari	TATP	1,2	5300
	TNT	1,55	6850
	PA	1,60	7900
	PETN	1,6	7920
	RDX	1,70	8440
	HMX	1,89	9110
Explosiu terciari	AN	1,72	3700

* La NG és un explosiu primari degut a la seua sensibilitat a un estímul extern.

1.5 Termodinàmica dels explosius

La termoquímica dels explosius consisteix en l'avaluació de diferents paràmetres emprats per a caracteritzar-los. Aquests són: balanç d'oxigen, calor d'explosió, volum de gas alliberat, potència explosiva i índex de potència.

1.5.1 Balanç d'oxigen

El balanç d'oxigen (OB) és un paràmetre que mesura la quantitat d'oxigen requerida per a la transformació total del carboni (C) en diòxid de carboni (CO_2), l'hidrogen (H) en aigua (H_2O) i els metalls en òxids metàl·lics. Després, la reacció s'ajusta amb la quantitat

d'oxigen alliberat o consumit.[20,35] Generalment, les reaccions químiques considerades per a determinar el OB no coincideixen amb les reaccions de descomposició.

Hi ha dues expressions diferents per a calcular el valor del OB. La primera consisteix a utilitzar l'Equació 1.1:

$$\mathrm{OB}\ (\%) = \left(\mathrm{n_O} - 2\mathrm{n_C} - \frac{\mathrm{n_H}}{2} - n_M\right) \cdot \frac{1599{,}940}{\mathrm{MW}} \qquad \text{Eq. 1.1}$$

On n_C, n_H, n_O, i n_M són el nombre de mols de carboni, hidrogen, oxigen i metall respectivament en la fórmula empírica de la molècula explosiva i MW és el pes molecular de l'explosiu.

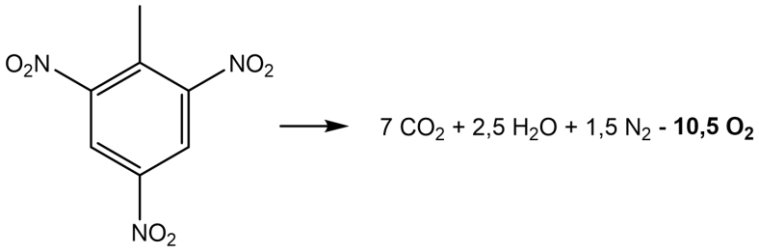

TNT

Esquema 6. Reacció química d'oxidació total del TNT.

Per exemple, la fórmula empírica del TNT és $C_7H_5N_3O_6$ i el pes molecular és 227,1312 g/mol. La reacció de descomposició es mostra en l'Esquema 6.

Com a resultat, el balanç d'oxigen de la detonació del TNT és -73,96%.

A més, el valor d'aquest paràmetre també es pot obtindre considerant: la quantitat d'oxigen alliberat o consumit (n_O) en la reacció ajustada de la combustió total de l'explosiu, el pes atòmic de l'oxigen (AW_O) i el pes molecular de l'explosiu ($MW_{explosiu}$) com es mostra en l'Equació 1.2:

$$\mathrm{OB}\ (\%) = \frac{\mathrm{n_O} \cdot \mathrm{AW_O}}{\mathrm{MW_{explosiu}}} \cdot 100 \qquad \text{Eq. 1.2}$$

Per exemple, el pes molecular de la NG ($C_3H_5N_3O_9$) és de 227 g/mol i la reacció de descomposició s'il·lustra en l'Esquema 7. Per tant, el balanç d'oxigen per a la NG és 3,52%.

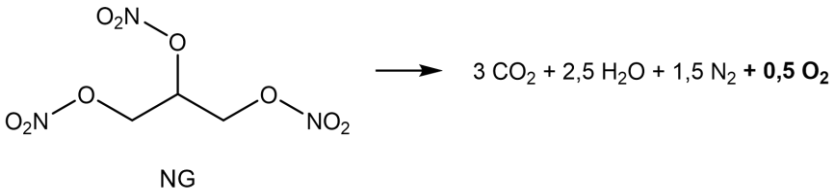

Esquema 7. Reacció química de la combustió total de la NG.

Aleshores, els compostos explosius també es poden classificar utilitzant el OB (Taula 2) degut a que aquest pot tindre valor positiu, zero o negatiu i a més, dóna informació sobre els productes de descomposició. Un resultat negatiu indica que la molècula explosiva conté menys oxigen del necessari per a la seua oxidació completa. Així doncs, s'alliberaran gasos nocius com el monòxid de carboni (CO). Quan el balanç d'oxigen és positiu o zero indica que l'explosiu conté més o la quantitat exacta d'oxigen, respectivament, per a la seua oxidació. La majoria dels explosius secundaris utilitzats en el camp militar tenen un balanç d'oxigen negatiu.

1.5.2 Calor d'explosió

Com s'havia mencionat anteriorment, els productes de la descomposició d'un explosiu són principalment calor i gasos. La calor d'explosió (Q) proporciona informació sobre la quantitat d'energia alliberada i la potència de l'explosiu quan s'inicia la detonació o deflagració. La diferència entre la calor de formació dels productes (ΔH_p) i la calor de formació del propi explosiu (ΔH_r) amb el pes molecular de l'explosiu (MW_e) s'utilitza per a calcular Q (Equació 1.3). Un valor elevat de Q implica que l'explosiu alliberarà més energia després de la iniciació.[11]

$$Q = \frac{(\Delta H_p - \Delta H_e)}{MW_e} \cdot 1000 \qquad \text{Eq. 1.3}$$

Per exemple, considerant la detonació del PETN, la calor d'explosió es calcula utilitzant la Llei d'Hess (Figura 6).

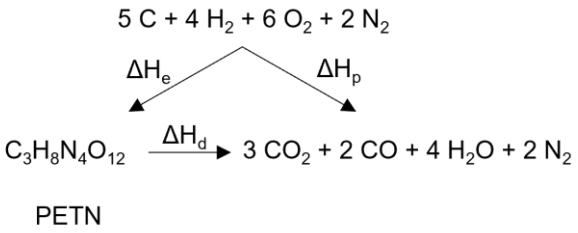

Figura 6. Entalpia de detonació del PETN emprant la llei d'Hess.

Per tant, si s'aplica l'Eq. 1.3 a la descomposició del PETN (MW_{PETN} = 316,138 g·mol^{-1}),

$$Q = \frac{[3 \cdot \Delta H_f\,(CO_2) + 2 \cdot \Delta H_f\,(CO) + 4 \cdot \Delta H_f\,(H_2O)] - [\Delta H_f\,(PETN)]}{MW_e} \cdot 1000$$

el valor de Q és -5815 kJ·kg^{-1} (el signe negatiu indica que és una reacció exotèrmica).

Com podem observar en la Taula 2, la calor d'explosió es veu afectada pel valor de l'OB. Així, quan és zero, la calor d'explosió aconsegueix el seu màxim. En conseqüència, alguns explosius secundaris amb valors d'OB molt negatius com el TNT es mesclen amb uns altres amb OB positius com l'AN per a que aquest valor estiga el més pròxim possible a zero. A més, la calor d'explosió també es pot augmentar mesclant l'explosiu amb un altre combustible amb major calor de combustió, com el beril·li, l'alumini o el bor.

1.5.3 Volum de gas alliberat en l'explosió

Un altre paràmetre important per a avaluar el poder explosiu és el volum de gas (V_T) generat en l'explosió. Es pot calcular a partir de la reacció de descomposició de l'explosiu considerant el volum de productes gasosos, mesurats en condicions de estàndard de temperatura i pressió o "stp" (1 atm, 273,15 K). A més, segons la llei d'Avogadro 1 mol de gas ocuparà 22,4 L en aquestes condicions. Per tant, el volum de gasos alliberats s'obtindrà mitjançant l'Equació 1.4.

$$V_T = \frac{\sum n_{gas} \cdot 22{,}4}{MW} \cdot 1000 \qquad \text{Eq. 1.4}$$

On n_{gas} és el nombre de mols de productes gasosos en la reacció de descomposició de la molècula explosiva i MW és el pes molecular de l'explosiu.

Per exemple, el MW del TNT és 227 g·mol^{-1} i la reacció de descomposició es mostra en l'Esquema 8.

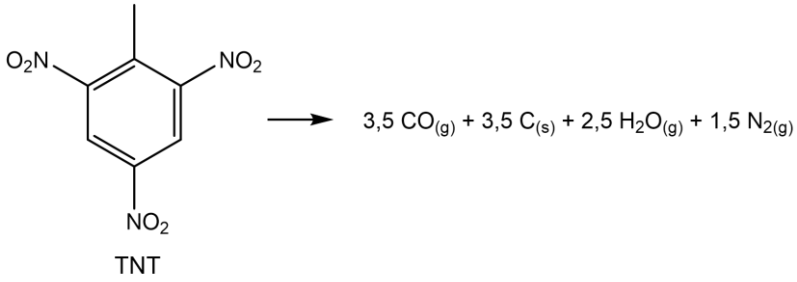

Esquema 8. Reacció química de detonació del TNT.

Aleshores, el nombre de mols de gas generat en la detonació del TNT és de 7,5 i, per tant, el volum de gasos alliberats és de 740 $dm^3 \cdot kg^{-1}$, com s'il·lustra en la Taula 2.

1.5.4 Potència explosiva i índex de potència

La potència explosiva (EP) es defineix com el producte de la calor de l'explosió (Q) i el volum de gasos (V) alliberats en la reacció de detonació explosiva (Equació. 1.5).

$$EP = Q \cdot V \qquad \text{Eq. 1.5}$$

L'índex de potència (PI) s'obté quan es compara el valor de la potència explosiva amb la potència explosiva d'un patró, generalment àcid pícric (Equació 1.6).

$$PI\ (\%) = \frac{Q_i \cdot V_i}{Q_{PA} \cdot V_{PA}} \cdot 100 \qquad \text{Eq. 1.6}$$

Taula 2. Comparació dels diferents paràmetres termodinàmics d'alguns explosius ràpids.[11,23,35,36,37]

Explosiu	OB (%)	Q ($kJ \cdot kg^{-1}$)	V_{gas} ($dm^3 \cdot kg^{-1}$)	EP·10^4 ($kJ \cdot dm^3 \cdot kg^{-2}$)	PI (%)
Fulminat de mercuri	- 16,9	1757	236	38	14
NG	+ 3,5	6228	740	461	168
EGDN	0,00	6716	737	495	180
PETN	- 10,1	5815	780	453	165
RDX	- 21,6	5076	908	461	168
HMX	- 21,6	5012	908	455	166
PA	- 45,4	3301	831	274	100
TNT	- 74,0	4092	740	303	110
HMTD	- 92,2	3450	1075	371	135
TATP	- 151,2	2745	855	235	86
AN	+ 20,0	1441	980	141	51

1.6 Mescles d'explosius

Normalment, els materials explosius estan formats per una mescla d'un o més explosius individuals amb alguns altres compostos com combustibles, oxidants, aglutinants i/o plastificants per a millorar les seues propietats segons la seua aplicació. Per exemple, el TNT es mescla amb AN per a millorar les propietats explosives a causa del OB negatiu del TNT, com havíem esmentat abans. Un altre exemple és la composició química de la dinamita Goma-2, que es basa en una barreja d'AN amb dinitrat d'etilenglicol (EGDN), serradura i plastificants.[25]

1.7 Marcadors explosius

Els marcadors d'explosius (Figura 7) són compostos nitroderivats que mostren pressions de vapor moderades, al voltant de tres o quatre ordres de magnitud més elevades que el TNT (Taula 3), i s'evaporen lentament de l'explosiu. L'addició d'aquests marcadors és obligatòria en tots els explosius fabricats legalment per a la seua identificació com explosius comercials i militars en aeroports, entrades a edificis públics i altres llocs apropiats, així com per a la detecció forense després d'explosions.[38] Algunes molècules nitro-aromàtiques com el 2-nitrotoluè (2- NT), 3-nitrotoluè (3-NT) i 4-nitrotoluè (4-NT) s'usen com a marcador per a la detecció del TNT,[39] mentre que 2,3-dimetil-2,3-dinitrobutà (DMDNB) s'utilitza com a marcador en explosius plàstics com el C-4 (91% RDX) i el Semtex (40-76% PETN).[29,40,41,42] Aquest treball es centra en la detecció d'alguns d'aquests analits, a més d'altres compostos amb grups funcionals nitro.

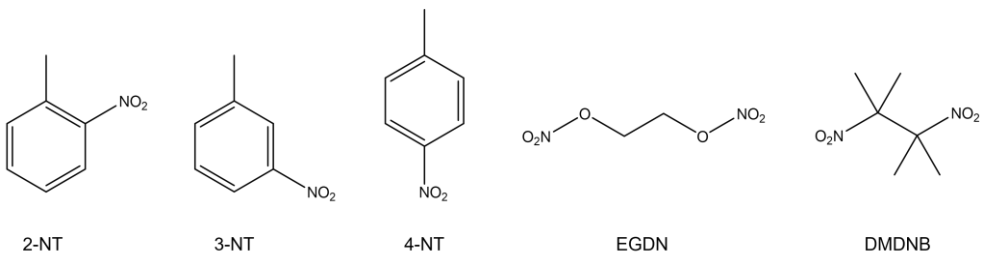

Figura 7. Estructura química dels marcadors explosius.

Taula 3. Pressió de vapor d'alguns explosius comuns i marcadors explosius a 25 °C.[43,44]

Substància	NM	NG	RDX	HMX	TNT	TATP	EGDN	DMDNB	4-NT
Pressió de Vapor (atm)	$4{,}7\cdot10^{-2}$	$6{,}5\cdot10^{-7}$	$4{,}9\cdot10^{-12}$	$2{,}4\cdot10^{-17}$	$9{,}2\cdot10^{-9}$	$6{,}3\cdot10^{-5}$	$1{,}0\cdot10^{-4}$	$2{,}7\cdot10^{-6}$	$6{,}5\cdot10^{-5}$

1.8 Tècniques per a la detecció d'explosius

La detecció d'explosius ha atret una atenció considerable en seguretat nacional, detecció de mines terrestres, operacions antiterroristes, investigació forense, salut humana i seguretat ambiental.[45,46]

No obstant, com hem vist abans, els explosius ràpids basats en NO_2 tenen una pressió de vapor molt baixa, per davall de 10^{-7} atm. a temperatura ambient i, com a resultat, només es troben traces de molècules explosives en les mostres d'aire, la qual cosa les fa extremadament difícils de detectar. Degut a això, els explosius disponibles en el mercat es formulen amb molècules volàtils conegudes com a marcadors d'explosius per a millorar la seua detectabilitat. Amb la finalitat de detectar selectivament traces d'explosius, s'utilitzen diferents eines analítiques per a la identificació i quantificació d'explosius.

1.8.1 Detecció d'explosius amb gossos entrenats

Els gossos es consideren un dels mètodes més fiables per al treball de camp en la detecció d'explosius. Això és possible a causa de la gran capacitat per detectar entre tres tipus diferents de compostos que estan directament relacionats amb la molècula explosiva: l'explosiu mateix, un marcador explosiu o un altre compost residual i algun producte de la descomposició explosiva.

Els canins també mostren una extraordinària especificitat, és a dir, són capaços de distingir entre l'analit que ha sigut entrenat per a detectar i un altre compost similar, i sensibilitat perquè el seu llindar de detecció ha mostrat sensibilitats per davall de 10^{-16} M, encara que la sensibilitat depèn molt en el seu entrenament.[47] Altres inconvenients estan relacionats amb el manteniment, els protocols d'entrenament de llarga durada i la infraestructura que el converteix en un mètode de detecció bastant costós.[48,49]

1.8.2 Tècniques instrumentals de detecció

Diferents mètodes analítics han sigut utilitzats per a detectar traces d'explosius en estat sòlid, líquid i vapor.[20,50]

1.8.2.1 Cromatografia-espectrometria de masses

Les tècniques cromatogràfiques són un grup de tècniques de separació basades en la diferència de velocitats dels components d'una mescla quan viatgen a través de la columna a causa de la seua diferent afinitat entre les fases mòbil i estacionària. Segons l'estat físic de la fase mòbil, aquestes tècniques es classifiquen en cromatografia de gasos (GC), cromatografia de líquids (LC) i cromatografia de fluids supercrítics (SFC).

L'espectrometria de masses (MS) es basa en la separació i l'anàlisi dels ions d'una molècula orgànica segons la seua relació massa-càrrega (m/z). Existeixen diferents analitzadors de masses, com el quadrupol, el capturador d'ions, el temps de vol (TOF) i les tècniques basades en una combinació d'aquestes.

Tècniques acoblades com la cromatografia de gasos-espectrometria de masses (GC-MS) quan l'analit és volàtil o la cromatografia líquida-espectrometria de masses (HPLC-MS) s'han emprat per a identificar i quantificar traces d'explosius, ja que combinen la capacitat de separació de la cromatografia amb la sensibilitat i selectivitat d'un espectròmetre de masses.[51,52,53]

Així i tot, la majoria de les mostres requereixen algun tractament previ per a eliminar alguns dels compostos de la matriu que podrien interferir en l'anàlisi, augmentar la selectivitat i la concentració d'analit.

1.8.2.2 Espectroscòpia Raman

L'espectroscòpia Raman es basa en els canvis en els nivells vibracionals quan una molècula és irradiada amb una radiació potent, normalment un làser. Per consegüent, l'espectre Raman proporciona informació sobre l'estructura química de l'analit i, per tant, consisteix en l'empremta digital de la molècula. No obstant això, aquesta tècnica no és adequada per a determinar quantitats traça d'analit degut a la seua baixa sensibilitat. Per això, una alternativa per a aconseguir un menor límit de detecció (LOD) és la Dispersió Raman Millorada en la Superfície (SERS). Està basada en una millora de la senyal de resposta quan els analits s'adsorbeixen sobre la superfície de les nanopartícules, ja siga en dissolució o depositats sobre un substrat, i produeix una alteració en els estats electrònics que indueix un canvi en la polaritzabilitat de la molècula.[54,55]

1.8.2.3 Difracció de raigs X

La difracció de raigs X (XRD) és una tècnica no invasiva que proporciona informació sobre l'estructura química de les mostres. Aquesta tècnica es basa en les interferències constructives quan un feix de raigs X monocromàtic incideix sobre la mostra en el mateix angle en el que es dispersat. En aquest angle específic, la radiació, que obeeix la llei de Bragg, es dispersada des de cada conjunt de plans de la xarxa de la mostra cap al detector. La XRD s'ha utilitzat per a la identificació d'explosius mitjançant l'ús d'una base de dades d'espectres per a augmentar l'eficàcia del mètode.[56,57,58]

1.8.2.4 Mètodes electroquímics

Els mètodes electroquímics es basen en la mesura dels processos de transferència d'electrons a causa d'una reacció redox que s'ha produït en la interfase elèctrode/solució. Aquests mètodes es poden classificar en conductimètrics, amperomètrics o potenciomètrics depenent de si la variable és corrent, conductivitat o voltatge, respectivament. Els compostos nitro-explosius tenen un caràcter redox particular a causa de la presència del grup NO_2 en la molècula que permet la seua detecció electroquímica. Els sistemes electroquímics ofereixen un temps de resposta ràpid amb alta sensibilitat, però s'apliquen principalment a mostres en fase líquida.[59,60]

1.8.2.5 Tècniques nuclears de detecció

Els mètodes nuclears es basen en l'anàlisi del nucli atòmic per a obtindre informació sobre la composició elemental de la molècula mesurant la radiació gamma o els neutrons emesos/transmesos. Aquests mètodes es divideixen en dues categories, els que utilitzen neutrons com a feix incident i els que utilitzen un altre tipus de partícules, com a protons o fotons. Quan la mostra és impactada amb una font de radiació, aquesta interactua amb el nucli atòmic de la mostra, el que permet realitzar un anàlisi isotòpic d'aquesta per a obtindre una empremta digital de l'analit. Les tècniques nuclears tenen una gran capacitat de penetració a causa de la poca probabilitat d'interacció entre el feix incident i les partícules del nucli i una alta especificitat, el que les converteix en una eina útil per a la detecció de traces d'explosius en contenidors de vaixells de càrrega, equipatge facturat, etc.[61,62,63] No obstant això, totes aquestes tècniques utilitzen isòtops radioactius com a font de radiació, la qual cosa limita les seues aplicacions a causa de les normes de seguretat i salut.

A pesar que aquestes tècniques compleixen amb els requisits necessaris per a la detecció de traces d'explosius, com l'elevada sensibilitat i selectivitat, la majoria d'elles són costoses i requereixen instrumentació voluminosa i sofisticada, la qual cosa limita la seua portabilitat i el treball de camp. A causa d'aquestes limitacions, existeix una recerca constant d'un sistema de detecció adequat per a diferents entorns, des de la detecció de vehicles fins a ubicacions estratègiques, com a aeroports i edificis governamentals.

1.9 Sensors químics d'explosius

Un sensor químic és un sistema de detecció que indica la presència o absència de l'analit objectiu mitjançant la generació d'una resposta mesurable que permet la seua identificació i/o quantificació.

Idealment, un sensor d'explosius ha de ser xicotet i compacte per a poder incorporar-lo en dispositius portàtils i, a més, combinar un temps de resposta curt i la robustesa, necessaris per al treball rutinari de camp, amb un ampli rang lineal, baix límit de detecció, bona sensibilitat i selectivitat per a ser capaç de detectar traces dels compostos explosius. Aquests requisits són molt exigents, especialment perquè els sensors també han de ser rendibles i estar llestos per a la seua producció en massa. Durant l'última dècada, l'atenció dels científics s'ha centrat principalment en el desenvolupament de sensors que utilitzen nanomaterials degut a que presenten excel·lents propietats òptiques, catalítiques, elèctriques i electroquímiques. Per aquesta raó, aquests materials poden oferir grans beneficis com una bona portabilitat, baix cost, alta selectivitat i sensibilitat.[64]

1.9.1 Sensors òptics

Els sensors d'explosius basats en el mecanisme de transducció electroquímica es troben entre els preferits degut a les propietats redox dels compostos que contenen NO_2, així com també, de la seua senzillesa, rendibilitat, alta sensibilitat, resposta ràpida i idoneïtat per a dispositius portàtils.[65] No obstant això, la majoria d'aquests sensors es limiten a la detecció en fase líquida.

Altres estratègies involucren les propietats òptiques dels nanomaterials com l'absorbància (colorimètrica) i la fluorescència o fotoluminescència. Aquests mostren els mateixos avantatges que els sensors electroquímics però, a més a més, es poden aplicar

per a la detecció d'analits en fase de vapor. Per això, basant-se en els òptims resultats obtinguts a partir l'exposició d'aquests tipus de sensors a diferents compostos orgànics volàtils com amines biogèniques[66] o tiols com el 2-mercaptoetanol,[67] es van proposar per a la detecció d'explosius.[68,69]

A més, l'objectiu científic i tecnològic del projecte de l'OTAN "*High-selective nanoantenna for explosives detection*" es va basar en el desenvolupament de nous elements sensibles basats en receptors polimèrics artificials de mida nanomètrica amb capacitat de resposta òptica per al seu ús en detectors d'explosius portàtils i econòmics, capaços de detectar traces de substàncies explosives. Per aquesta raó, en aquesta tesi s'han desenvolupat tres sensors òptics diferents per a detectar i quantificar traces de marcadors d'explosius en fase de vapor. Depenent de la nanopartícula, la resposta òptica generada es produeix a través de diferents mecanismes de transducció.

1.9.1.1 Sensat basat en la Ressonància del Plasmó Superficial Localitzat

Les nanopartícules de metalls nobles, com l'Ag i l'Au, presenten ressonància del plasmó superficial localitzat (LSPR) com a resultat de la interacció entre les NPs i la radiació electromagnètica de major o igual longitud d'ona que la grandària que aquestes, la qual cosa produeix un efecte de ressonància a causa d'una oscil·lació col·lectiva d'electrons lliures en la banda de conducció de la NP. A més, aquest fenomen s'observa en el rang visible de l'espectre electromagnètic el que permet l'ús de mètodes de mesurament senzills.[70,71,72]

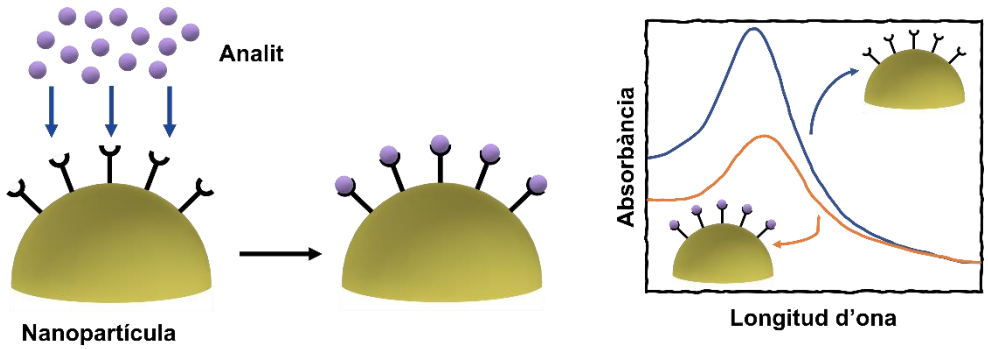

Figura 8. Mecanisme de sensat basat en la LSPR.

La LSPR depèn de la grandària, la forma i l'índex de refracció del mitjà circumdant de les NPs. Per aquesta raó, els mecanismes de detecció es basen en els canvis de les propietats òptiques (la intensitat i l'amplada de banda de la LSPR i la longitud d'ona del màxim d'absorció de la LSPR), que poden ocórrer quan les molècules de l'analit interactuen amb la superfície de les NPs (Figura 8).[73] Aquests mecanismes consisteixen en la variació de l'índex de refracció del mitjà circumdant de la superfície metàl·lica,[74] la dispersió en la superfície de les NPs,[75] l'agregació de les NPs[76] i la transferència de càrrega entre les NPs i els analits adsorbits.[66,77]

1.9.1.2 Sensat basat en la fluorescència

Els sensors basats en fluorescència s'empren per a detectar traces d'explosius i marcadors explosius degut a avantatges com un temps de resposta curt i en temps real, límit de detecció baix i elevada selectivitat.[78] El mecanisme de detecció es basa principalment en el canvi de la intensitat de la fluorescència (disminució o augment) quan les molècules d'analit interactuen amb els fluorocroms, com es mostra en la Figura 9.[30] L'*estat de l'art* indica que polímers conjugats,[79] *nanoclusters*,[80] *metal-organic frameworks*,[81] dendrímers,[42] punts quàntics luminescents (QDs)[82] i perovskites híbrides,[83] entre altres,[84] han sigut utilitzats amb el mateix propòsit.

Els mecanismes d'extinció de la fluorescència com la transferència d'electrons fotoinduïda (PET), la transferència d'energia de ressonància (RET), l'intercanvi d'electrons i la transferència de càrrega intramolecular (ICT) són predominants en la detecció d'explosius que contenen el grup nitro. No obstant això, altres mecanismes poden ser possibles. Quan la NP es troba embeguda en un polímer, la interacció entre l'analit i la superfície de la NP pot ser possible si l'analit es difon a través del polímer. En conseqüència, aquest procés produeix un inflament que afecta les propietats d'emissió.

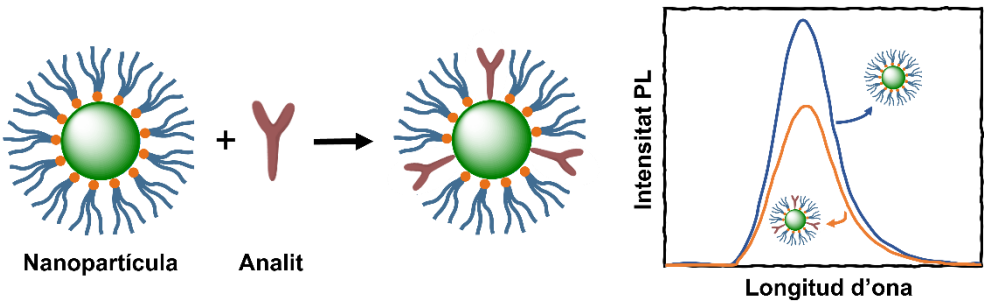

Figura 9. Mecanisme de sensat basat en la fluorescència.

1.10 Nanocompòsits híbrids

Els sensors basats en NPs s'utilitzaven principalment en dissolució degut als inconvenients per a depositar-los sobre un suport sòlid, com una distribució irregular de les NP i unes propietats mecàniques deficients.[85,86]

Els nanocompòsits consisteixen en materials formats per més d'un component en els quals, almenys un d'ells té una grandària nanomètrica. En aquests materials, les NPs s'incorporen a una matriu orgànica o inorgànica per a millorar les seues propietats. En particular, els nanocompòsits híbrids polimèrics combinen les propietats òptiques de les NPs amb les propietats mecàniques i tèrmiques dels polímers orgànics, com la flexibilitat, les propietats conductives/dielèctriques, el bon processament en pel·lícules molt primes, etc., el que fa possible la síntesi de capes molt primes mitjançant tècniques de deposició convencionals *(spin-coating*, *inkjet printing*, *dip-coating*, *blade coating*, etc.).[86,87,88,89] A més, l'estabilitat química i tèrmica i l'organització de les NPs augmenten quan es troben embegudes en la matriu polimèrica.

Com havíem esmentat anteriorment, es poden utilitzar diferents tècniques per a obtindre pel·lícules primes a partir de solucions precursores. El mètode de deposició que s'utilitza en aquesta tesi doctoral és el *spin-coating*. Consisteix a deixar caure una xicoteta quantitat de solució sobre un substrat i després aquest es fa rotar a una velocitat molt elevada per a obtindre una capa prima homogènia. Finalment, per a eliminar les restes de dissolvent i afavorir l'adherència del film al substrat, es calfa sobre una placa calefactora. La grossària de la capa depèn de la viscositat del polímer, així com de la velocitat i temps de rotació.

1.11 Tecnologia d'impressió molecular (MIT)

Una de les estratègies per a millorar la selectivitat i sensibilitat dels sensors òptics és l'ús de mètodes d'impressió molecular per a generar llocs de reconeixement molecular artificial en un polímer.[90] Generalment, el mètode convencional per a la síntesi de MIPs no covalents consisteix a polimeritzar el monòmer i el reticulant en presència de molècules d'empremta. Posteriorment, el polímer resultant es llava amb diferents solvents per a eliminar l'empremta i generar cavitats estereoespecífiques tridimensionals (Figura 10A).[91,92,93,94]

En aquest treball s'ha triat el mètode d'encapsulació per a sintetitzar el MIP. Com podem observar en la Figura 10B, en aquest mètode el sensor es prepara mesclant el polímer amb l'empremta seguint un mètode *sol-gel* o hidrotèrmic.[90,95] Quan es retira l'empremta de la matriu polimèrica es generen unes nanocavitats en aquesta.

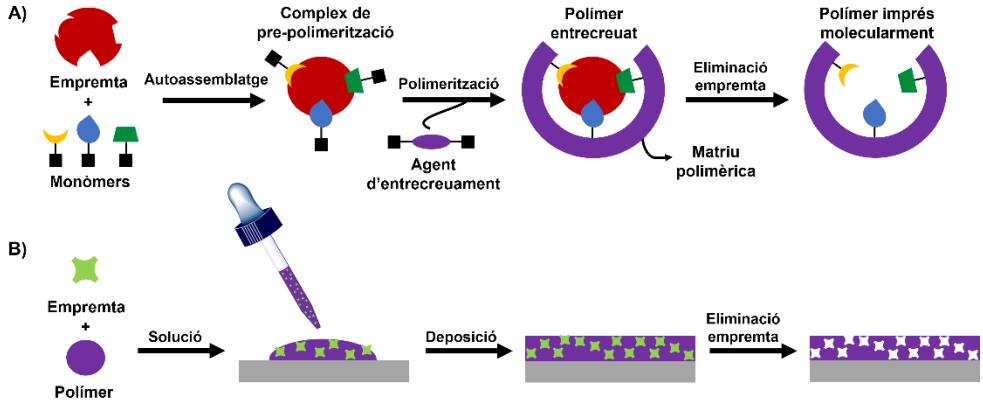

Figura 10. Síntesi del MIP mitjançant A) mètode no covalent i B) mètode d'encapsulació.

Les cavitats específiques en ambdós mètodes tenen una grandària i forma similar a la molècula d'empremta i un entorn químic que condueix cap als fenòmens de reconeixement molecular.[96] D'aquesta manera, el polímer imprés molecularment (MIP) resultant reconeixeria i s'uniria selectivament només a aquelles molècules amb grandària, forma i grups funcionals similars als de la molècula d'empremta, com es mostra en la Figura 11.[97] Diversos autors han proposat diferents estratègies per a la fabricació de sensors en estat sòlid basats en MIP per a la detecció d'explosius[98,99] i altres analits,[100,101] però totes experimenten procediments lents i amb diversos passos.

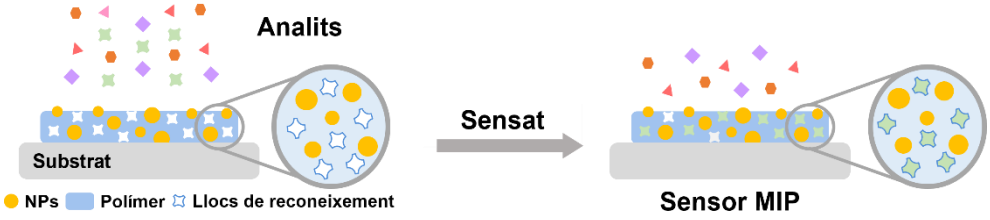

Figura 11. Procés de sensat d'un polímer imprés molecularment (MIP).

Chapter 1

Introduction

In recent years, the growing threat of an explosive terrorist attack has increased the need to develop technologies to detect them quickly and reliably. However, these materials are usually packaged, hidden or in very low concentrations, which limits the detection capability. Therefore, the development of effective detection methods to identify and quantify explosive compounds in very different scenarios, such as containers, vehicles, or luggage, are essential.

For that reason, the main objective of this PhD thesis is the research and development of different sensing platforms based on optical transduction systems, which can detect trace amounts of explosive or explosive taggants selectively and reproducibly, with an adequate response time and also, they can be incorporated into portable systems that allow real-time analysis.

1.1 Explosive materials

An explosive can be defined as a device, chemical compound, or mixture of different compounds, which are capable to produce an explosion. It means an extremely exothermic and fast chemical reaction due to the generation of large amounts of heat and pressure, generally produced by the formation of gases from the decomposition of the explosive, with rapid expansion of matter in a very short period of time.[1] However, explosives cannot undergo decomposition without some external stimuli to initiate the process. Because of that, they are very sensitive to impact, friction, shock, or any simple application of an energy pulse.[2,3] Most of the explosives contain oxygen and nitrogen in greater proportion than other organic compounds, and oxidisable compounds (fuels) such as carbon, hydrogen and metals.[4] During the decomposition reaction the nitrogen and oxygen react with fuels generating mainly CO/CO_2, H_2O, and N_2 (Scheme 1).

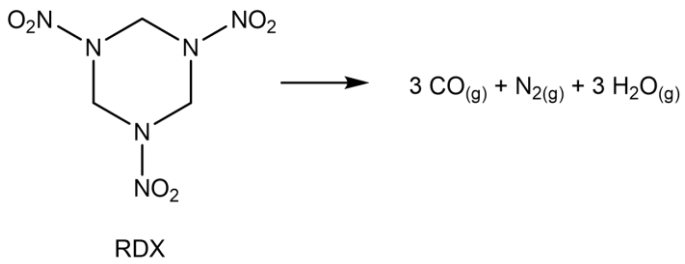

Scheme 1. Chemical reaction of 1,3,5-trinitroperhidro-1,3,5-triazine (RDX) detonation.

1.2 Historical aspects

In this part of the chapter, we focus on an overview of some relevant explosive developments and applications (Figure 1).

Black powder was the first known explosive. It was discovered accidentally by some Chinese alchemists in 220 BC, but it was not introduced to Europe until 1249 when the scientist Roger Bacon mixed saltpetre (potassium nitrate, oxidizer) with charcoal and sulfur (fuels) as is shown in the Scheme 2. From then on, many countries used black powder for military issues.

$$8\ C + 3\ S + 10\ KNO_3 \rightarrow 3\ K_2SO_4 + 2\ K_2CO_3 + 6\ CO_2 + 5\ N_2$$

Blackpowder

Scheme 2. Reaction scheme of black powder decomposition.[5]

In 1846, the Italian chemist, Ascanio Sobrero, synthesized liquid nitroglycerine (NG) but he abandoned his studies due to its explosive nature. However, in 1863, Alfred Nobel and his father developed a fabrication process of nitroglycerine (NG), which consisted of adding glycerine to a cold mixture of highly concentrated nitric and sulfuric acids under continuous stirring. Finally, nitroglycerine was washed with water and with an alkaline solution to remove the acid remains. They had some drawbacks in the manufacturing process due to their high shock sensitivity and unpredictable initiation by black powder and in 1864, an explosion destroyed the factory and killed five people, including Alfred's brother, Emil. The same year, Alfred Nobel invented the metal blasting cap detonator, which contained mercury fulminate ($Hg(CNO)_2$) to replace black powder as an initiator. In 1866, he focused on developing a method to reduce the nitroglycerine reactivity, after another accidental explosion that shattered the entire factory. Therefore, they mixed nitroglycerine (75%) with an adsorbent material based on diatomaceous earth (Kieselguhr, 25%) obtaining a solid much safer to handle and easier to use, which was patented in 1867 as Ghur Dynamite.[6]

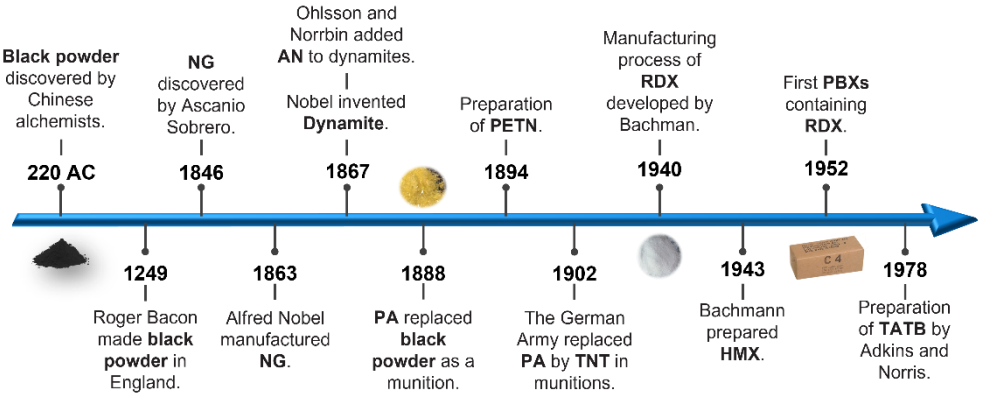

Figure 1. Timeline of some important explosive discoveries.

Although ammonium nitrate (AN) was not considered an explosive, in 1867, the Swedish chemists Ohlsson and Norrbin realized that the explosive properties of dynamite were improved by the addition of AN and after that, Nobel incorporated it in their manufacturing

process. At the same time, the nitration of cellulose to obtain nitrocellulose (NC) was carried out by Schönbein and Böttger in 1875. Alfred Nobel discovered that the mixture of nitroglycerine with nitrocellulose formed a gel that was used to produce gelatine dynamite, but it was only used for civil purposes.

In 1888, picric acid (PA) replaced black powder for military uses in grenades and landmines due to the sensitivity of its metal salts to shock. The development of Tetryl occurred at the same time as the PA, but until 1906 it was not used as an explosive.

The synthesis of pure 2,4,6-trinitrotoluene (TNT) in 1880 by Hepp and its subsequent development as an explosive compound in 1899, replaced the use of picric acid in military operations. Their manufacture consists of three successive nitration steps of toluene by mixing it with a mixture of HNO_3 and H_2SO_4 (Scheme 3). It was the standard explosive during the First World War but, due to the shortage of toluene to produce TNT, a mixture of TNT and AN (amatol) became popular for the filling of military arms.[7,8]

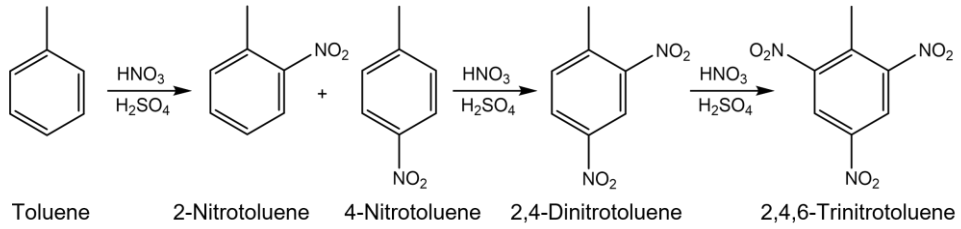

Scheme 3. Preparation of 2,4,6-trinitrotoluene (TNT).

Although the most common explosives in the Second World War were hexogen (RDX) and pentaerythritol tetranitrate (PETN), their first application (and also NG) were to treat health issues as a vasodilator. RDX was the most widely used explosive because of the high sensitivity to impact and poor chemical stability of the PETN. The latter was used in mixtures of 50 % PETN and 50 % TNT (pentolite) for grenades and detonators but it was also replaced by the RDX. At the end of the Second World War, octogen (HMX), which was obtained as an impurity of the Bachman manufacturing process of RDX, became available.[9]

To reduce the sensitivity and enhance the mechanical properties and processability of explosives like RDX, HMX and PETN, they were embedded into a rubbery elastic polymer matrix (binder) constituting the polymer bonded explosives (PBXs). The first PBX was synthesized in 1952 in the USA and it consisted of RDX crystals embedded into plasticized polystyrene. Binders are selected depending on the reactivity of the

explosives. For instance, inert polymers such as Teflon, are chosen for high reactive explosives. In some cases, the addition of a plasticizer is also needed to enhance the processability and reduce the reactivity of the PBX. The most known PBXs are Semtex (PETN + rubber + plasticizer) and Composition C-4 (RDX + polyisobutylene + dioctylsebacate + oily material).[10]

Since 1955, the development of ammonium nitrate fuel oil (ANFO), water-gels (slurries), emulsions, and blasting explosives have reduced the price of explosives for civil purposes. Among other recent explosive developments, the hexanitrostilbene (HNS, Shipp in 1966), and triaminotrinitrobenzene (TATB, Norris and Atkins in 1978) were of great interest due to their extraordinary thermal stability and low sensitivity to external stimuli.[11]

One of the most modern explosives is organic peroxides. They are based on the peroxide functional group (-O-O-) . This bivalent structure can provide enough oxygen for fast self-oxidation and explosion. However, their high sensitivity to heat, shock, and friction combined with the high vapour pressure, compared with the nitro-based explosives, make them extraordinary unstable, unpredictable and very dangerous to handle.[12,13,14] As a result, the number of applications is very limited.

However, in the last two decades, organic peroxides such as triacetone triperoxide (TATP) and hexamethylene triperoxide diamine (HMTD) have centred the attention due to their use in terrorist attacks in Europe and the United States (US), among others (Figure 2). Due to their reactivity, both can be used as main charge or initiator.[16,17]

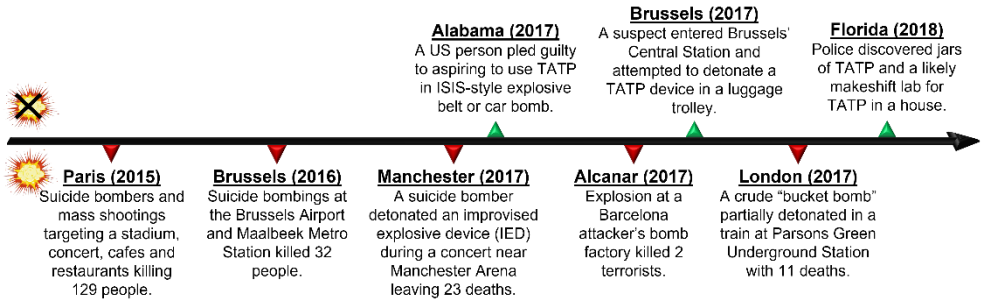

Figure 2. Some examples of successful and failed criminal attacks involving the use of TATP.[15]

TATP, also known as "Mother of Satan", was discovered by German chemist Richard Wolffenstein in 1895. It is a homemade explosive with almost the same shattering power as TNT, which can be easily synthesized by mixing acetone with highly concentrated

hydrogen peroxide using H_2SO_4, HCl or HNO_3 as an acid catalyst. The product precipitates in an unstable crystalline solid, which can sublime at room temperature.[18] However, depending on the pH and reagent concentrations diacetone diperoxide (DADP) can also be obtained as a secondary product (Scheme 4A).[19,20,21]

HMTD, also known as amine peroxide, was synthesized by Ludwig Leger in 1885 from the reaction of ammonia with the products of the combustion of ether. It is also a homemade explosive, which can be prepared from hexamine (HXM) and hydrogen peroxide in presence of an organic or inorganic acidic catalyst such as citric acid (Scheme 4B).[22,23] Although HMDT is less powerful than TATP, it is more sensitive, unstable, and difficult to detect because of its low vapour pressure.[24]

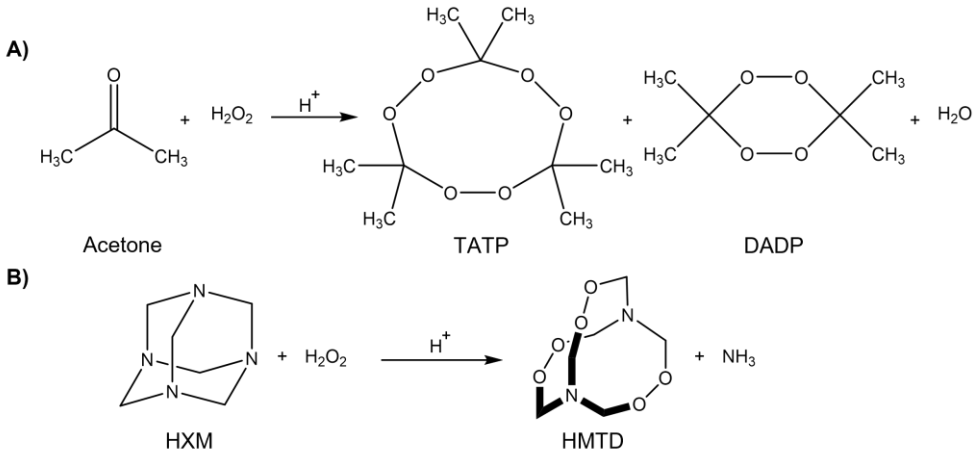

Scheme 4. A) Synthesis of TATP from acetone and hydrogen peroxide and B) Synthesis of HMTD from hexamine and hydrogen peroxide

Apart from organic peroxides, other commercial and homemade nitro-based explosives have been used in criminal attacks. For example, ANFO was used in the terrorist attacks in Oklahoma City in 1995 and Oslo in 2011 and dynamite (Goma-2)[25] was chosen for Al-Qaeda in the Madrid train bombings in 2004.[16]

1.3 Explosive decomposition mechanisms

1.3.1 Velocity of detonation (VOD)

The detonation velocity corresponds to the detonation wave, which travels through the explosive. This parameter measures the power of the explosive and is directly proportional to the density of the explosive, the degree of confinement, the strength of initiation, and the diameter of the explosive.[26]

Generally, it is possible to distinguish between combustion (non-explosive) and two different explosion mechanisms (Figure 3A). When the explosive decomposition is initiated, they can burn (deflagration) or explode (detonation).[27]

1.3.1.1 Combustion

Combustion is defined as a fast and exothermic oxidation reaction, which releases huge amounts of gas at high temperatures in a big period of time. Some explosives can be burned without explosion because they contain both combustible molecules (fuel and oxidizer), as was mentioned before. However, depending on the explosive substance and the time reaction the generation of heat and gases can lead to deflagration or detonation processes. For instance, when 1 kg of coal burns, it can release about 32660 kJ of heat, which is much more than the heat liberated by 1 kg of TNT. However, the coal burning takes more than 3600 s whereas the time decomposition of TNT is 0.00001 s, undergoing an explosion.

1.3.1.2 Deflagration

Deflagration is defined as a reaction in which the velocity of the reaction front through the unreacted material does not reach the speed of sound in the solid or liquid state (generally 1000-3000 m/s) creating a subsonic wave front. The deflagration is initiated when a small amount of explosive ignites after the exposure to a flame, spark, or shock and it burns layer by layer. Each particle on the surface contains enough oxygen needed to burn and generate heat and gases, which affect the adjacent particles initiating a decomposition through a self-propagating process. Although this is a relatively slow mechanism controlled by the rate of heat transfer (conduction, convection, and radiation), when explosives are under confinement, the progressive formation of volatile compounds

will cause an explosion (Figure 3B). The direction of deflagration propagation is the opposite of the direction of the explosive decomposition products.

1.3.1.3 Detonation

Detonation is defined as a reaction in which the speed of propagation of the detonation front is higher than the speed of sound through the unreacted material creating a supersonic shock wave, normally exceeding 4000 m/s. The mechanism is controlled by the speed at which the material will transmit the shock wave and they do not need confinement to explode. The decomposition products and the shock wave advance in the same direction.

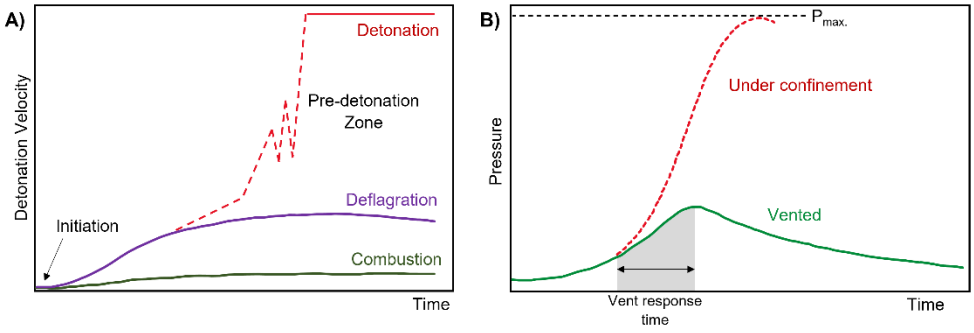

Figure 3. A) Explosion mechanisms considering VOD. B) Pressure-Time graph of a deflagration mechanism.[28]

1.4 Classification of the explosives

1.4.1 Based on their chemical composition and applications

Explosive substances (Figure 4) can be classified into six broad categories according to their chemical composition and applications. Nitroaliphatics such as nitromethane (NM), nitroaromatics such as 2,4,6-trinitrotoluene (TNT) and tetryl are the main components of explosives for military purposes and the principal components in the unexploded landmines. Nitramines such as 3,5-trinitroperhydro-1,3,5-triazine (RDX) and nitrate esters such as pentaerythritol tetranitrate (PETN) are the main components of plastic explosives for military and civil engineering like building demolition and excavation in mining. Acid salts such as ammonium nitrate (AN) and ammonium phosphate (AP), which are commonly used for the industrial applications and, peroxide-based explosives like

triacetone triperoxide (TATP) and hexamethylene triperoxide diamine (HMTD), which have grown rapidly as for homemade explosives because of their easiness to synthesize, as is mentioned before.[29,30,31,32] These classification does not give any information about the rate of the chemical decomposition as well as the amount of gas and heat released.

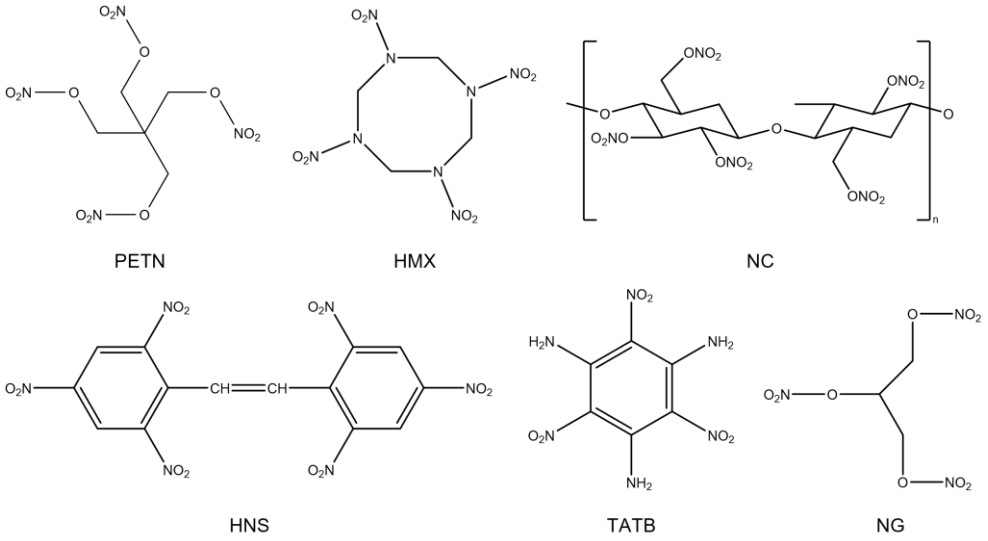

Figure 4. Chemical structure of some common explosive compounds.

1.4.2 Based on the VOD

Consequently, explosives can also be classified as either low or high explosives depending upon the VOD (Table 1). Low explosives or propellants are chemical compounds, which are characterized by the deflagration phenomenon. Gunpowder, smokeless powder, and gun propellants are the most common low explosives.

High explosives consist of different types of materials, which undergo detonation. According to their stability, there are divided into three different categories.[9,33]

Primary explosives or initiators are very sensitive to weak external stimuli such as heat, spark, or shock and have the ability to transmit the heat or shock produced in their ignition or detonation by a fuse or bridgewire to fewer sensitive explosives (Figure 5).

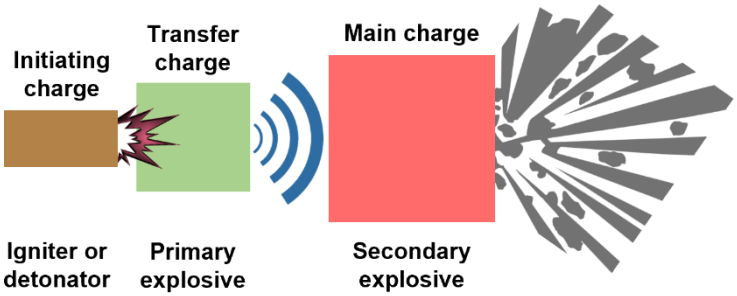

Figure 5. Schematic representation of an explosive material detonation.

Because of that, they are used in small quantities as an initiator of more stable explosives. The detonation velocity of them is in the range of 3500-5500 m/s. Lead azide, mercury fulminate, lead styphnate or nitroglycerine are some examples of primary explosives. The decomposition reaction of the mercury fulminate is shown in Scheme 5.

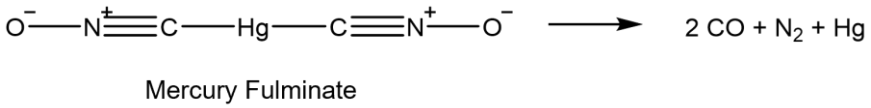

Mercury Fulminate

Scheme 5. Detonation reaction of mercury fulminate.

Secondary explosives are quite insensitive to thermal and mechanical stimuli and require an initiator to explode but generally, there has a bigger shattering effect than primary explosives. Most of them are aliphatic and aromatic molecules, which contain nitro groups (NO_2). The strong electron withdrawing (oxidant) character of NO_2 groups results in extraordinary powerful explosives. Moreover, upon detonation, NO_2 groups provide themselves with the essential oxygen for the combustion of aromatic rings producing CO_2 and the nitrogen atoms are converted to N_2 increasing the volume of evolved gas. The others are organic peroxides, which contain the O-O bond as a source of oxygen for fast self-oxidation and detonation. The detonation velocity of the secondary explosives is between 5500 and 9500 m/s. Some of these explosives are used in the military field such as 2,4,6-trinitrotoluene (TNT), 1,3,5-trinitroperhidro-1,3,5-triazine (RDX) or, pentaerythritol tetranitrate (PETN).

Tertiary explosives or blasting agents are insensitive compounds in which the initiation of the decomposition by flame, shock or friction is more difficult than other high explosives. There are mainly oxidants that, combined with the exact proportion of fuel

can release large amounts of energy. Some examples are ammonium nitrate and ammonium perchlorate.

Table 1. VODs of some explosive materials.[11,14,33,34]

	Explosive substance	Density ($g \cdot cm^{-3}$)	VOD ($m \cdot s^{-1}$)
Propellant	Black powder	-	400-500
Primary explosive	Mercury fulminate	3.3	4480
	NG*	1.6	7700
Secondary explosive	TATP	1.2	5300
	TNT	1.55	6850
	PA	1.60	7900
	PETN	1.6	7920
	RDX	1.70	8440
	HMX	1.89	9110
Tertiary explosive	AN	1.72	3700

* NG is a primary explosive due to its sensitivity to an external stimuli.

1.5 Explosive thermodynamics

The thermochemistry of the explosives consists of the evaluation of different parameters to characterize the explosive compounds. There are oxygen balance, heat of explosion, volume of evolved gas, explosive power, and power index.

1.5.1 Oxygen Balance

The oxygen balance (OB) is a parameter, which measures the amount of oxygen required for a total transformation of C in CO_2, H in H_2O, and metal in metallic oxide and then, the reaction is adjusted with the amount of oxygen released or consumed.[20,35] Generally, the chemical reactions considered to determine the OB do not coincide with the decomposition reactions.

There are two different expressions for calculating the OB value. The first consist of using the Equation 1.1:

$$\mathrm{OB}\ (\%) = \left(\mathrm{n_O} - 2\mathrm{n_C} - \frac{\mathrm{n_H}}{2} - n_M\right) \cdot \frac{1599.940}{\mathrm{MW}} \qquad \text{Eq. 1.1}$$

where n_C, n_H, n_O, and n_M are the number of moles of carbon, hydrogen, oxygen, and metal respectively in the empirical formula of the explosive molecule and MW is the molecular weight of the explosive.

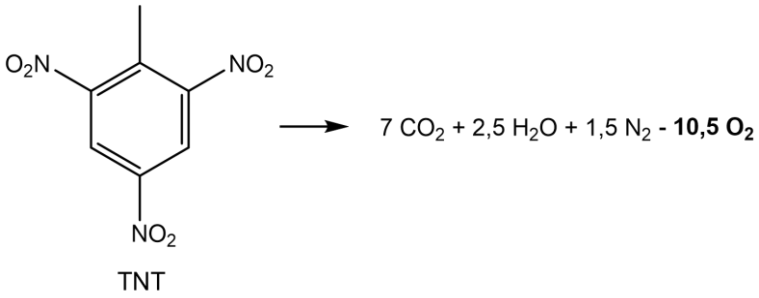

Scheme 6. Chemical reaction of the total oxidation of TNT.

For example, the empirical formula of the TNT is $C_7H_5N_3O_6$ and the molecular weight is 227.1312 g/mol. The decomposition reaction is shown in Scheme 6.

As a result, the oxygen balance of the TNT detonation is -73.96 %.

Moreover, it can also be obtained considering the amount of oxygen released or consumed (n_O) in the adjusted reaction of the total combustion of the explosive, the atomic weight of the oxygen (AW_O) and the molecular weight of the explosive ($MW_{explosive}$) as is shown in the Equation 1.2:

$$OB\ (\%) = \frac{n_O \cdot AW_O}{MW_{explosive}} \cdot 100 \qquad \text{Eq. 1.2}$$

For example, the molecular weight of NG ($C_3H_5N_3O_9$) is 227 g/mol and the decomposition reaction is illustrated in Scheme 7. Therefore, the oxygen balance for NG is 3.52 %.

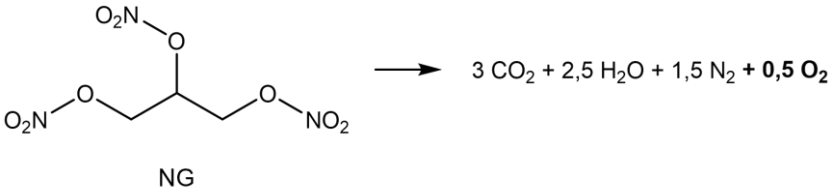

Scheme 7. Chemical reaction of the total combustion of NG.

Explosive compounds can also be classified using the OB (Table 2) because they may have positive, zero or negative values and it also gives information about the

decomposition products. A negative result indicates that the explosive molecule contains less oxygen than is required for its complete oxidation. As a consequence, harmful gases such as carbon monoxide (CO) will be released. When the oxygen balance is positive or zero indicates that the explosive contains more or the exact amount of oxygen, respectively for its oxidation. Most of the secondary explosives used in the military field have a negative oxygen balance.

1.5.2 Heat of Explosion

As mentioned before, the products of an explosive decomposition are mainly heat and gases. The heat of explosion (Q) provides information about the amount of energy liberated and also about the power of the explosive when the detonation or deflagration is initiated. The difference between the heat of formation of the products (ΔH_p) and the heat of formation of the explosive itself (ΔH_r) and the molecular weight of the explosive (MW_e) is used to calculate Q (Equació 1.3). A higher value of Q implies that the explosive will release more energy after initiation.[11]

$$Q = \frac{(\Delta H_p - \Delta H_e)}{MW_e} \cdot 1000 \qquad \text{Eq. 1.3}$$

For example, considering the PETN detonation, the heat of explosion is calculated using Hess's Law (Figure 6).

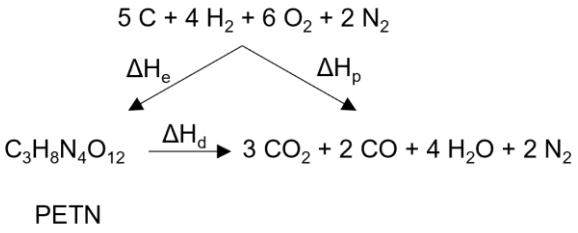

Figure 6. Enthalpy of detonation of PETN using Hess's law.

Therefore, if the Equation 1.3 is applied to the PETN decomposition (MW_{PETN} = 316.138 $g \cdot mol^{-1}$),

$$Q = \frac{[3 \cdot \Delta H_f\,(CO_2) + 2 \cdot \Delta H_f\,(CO) + 4 \cdot \Delta H_f\,(H_2O)] - [\Delta H_f\,(PETN)]}{MW_e} \cdot 1000$$

the value of Q is -5815 $kJ \cdot kg^{-1}$ (the negative sign indicates that it is an exothermic reaction).

As we can notice in Table 2, the heat of explosion is affected by the OB value. When it is zero, the heat of explosion reaches the maximum. Consequently, some secondary explosives with very negative values of OB such as TNT are mixed with others with positive OB such as AN due to approximate this value close to zero. Moreover, the heat of explosion can also be increased by mixing the explosive with another fuel with higher heat of combustion such as beryllium, aluminium, or boron.

1.5.3 Volume of gas liberated in the explosion

Another important parameter to evaluate the explosive power is the volume of gas (V) produced in the explosion. It can be calculated from the explosive decomposition reaction considering the volume of gaseous products, which are measured at “standard, temperature and pressure” or “stp” (1 atm, 273.15 K). Moreover, Avogadro’s law said that under these conditions 1 mol of gas will occupy 22.4 L. Therefore, the volume of gases released will be obtained using the Equation 1.4.

$$V_T = \frac{\sum n_{gas} \cdot 22.4}{MW} \cdot 1000 \qquad \text{Eq. 1.4}$$

In which n_{gas} is the number of moles of gaseous products in the decomposition reaction of the explosive molecule and MW is the molecular weight of the explosive.

For instance, the MW of the TNT is 227 $g \cdot mol^{-1}$ and the decomposition reaction is shown in Scheme 8.

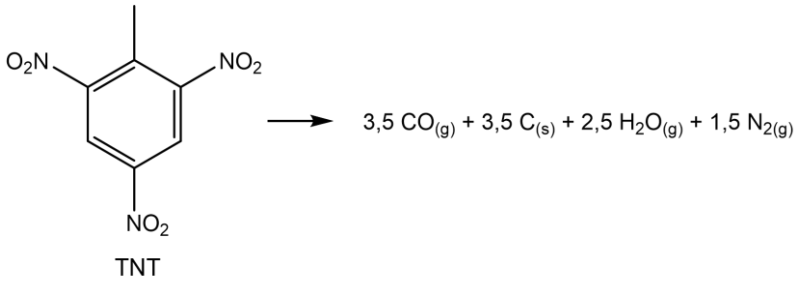

Scheme 8. Chemical reaction of the TNT detonation.

Therefore, the number of moles of gas generated in the TNT detonation is 7.5, and then the volume is 740 $dm^3 \cdot kg^{-1}$ as is illustrated in Table 2.

1.5.4 Explosive power and power index

The explosive power (EP) is defined as the combination of the heat of the explosion (Q) and volume of gases (V) released in the explosive detonation reaction (Equation 1.5).

$$EP = Q \cdot V \qquad \text{Eq. 1.5}$$

The power index (PI) is obtained when the value of the explosive power is compared with the power explosive of a standard, generally picric acid (Equation 1.6).

$$PI\ (\%) = \frac{Q_i \cdot V_i}{Q_{PA} \cdot V_{PA}} \cdot 100 \qquad \text{Eq. 1.6}$$

Table 2. Comparison of the different thermodynamic parameters of some high explosives.[11,23,35,36,37]

Explosive	OB (%)	Q ($kJ \cdot kg^{-1}$)	V_{gas} ($dm^3 \cdot kg^{-1}$)	EP·10^4 ($kJ \cdot dm^3 \cdot kg^{-2}$)	PI (%)
Mercury fulminate	- 16.9	1757	236	38	14
NG	+ 3.5	6228	740	461	168
EGDN	0.00	6716	737	495	180
PETN	- 10.1	5815	780	453	165
RDX	- 21.6	5076	908	461	168
HMX	- 21.6	5012	908	455	166
PA	- 45.4	3301	831	274	100
TNT	- 74.0	4092	740	303	110
HMTD	- 92.2	3450	1075	371	135
TATP	- 151.2	2745	855	235	86
AN	+ 20.0	1441	980	141	51

1.6 Explosive mixtures

Normally, explosive materials are composed of a mixture of one or more single explosives with some other compounds such as fuels, oxidizers, binders, and/or plasticizers to improve their properties depending on the application. As we mentioned before, TNT is mixed with AN to enhance the explosive properties due to the negative OB of TNT. Another example is the chemical composition of Goma-2 dynamite, which is based on AN mixed with ethylene glycol dinitrate (EGDN), sawdust and plasticizers.[25]

1.7 Explosive taggants

Explosive taggants (Figure 7) are nitro compounds, which show moderate vapour pressures, around three or four orders of magnitude higher than TNT (Table 3), and slowly evaporate from the explosive. The addition of taggants is mandatory in all legally manufactured explosives to identify commercial and military explosives at airports, entrances to public buildings and other appropriate sites, as well as for forensic detection after explosions.[38] Some nitroaromatic molecules such as 2-Nitrotoluene (2-NT), 3-Nitrotoluene (3-NT) and 4-nitrotoluene (4-NT) are used as taggant for TNT detection,[39] whereas 2,3-dimethyl-2,3-dinitrobutane (DMDNB) is used as a taggant in plastic explosives such as C-4 (91% RDX) and Semtex (40-76% PETN).[29,40,41,42] This work is focused on detecting some of these analytes, among other nitro containing compounds.

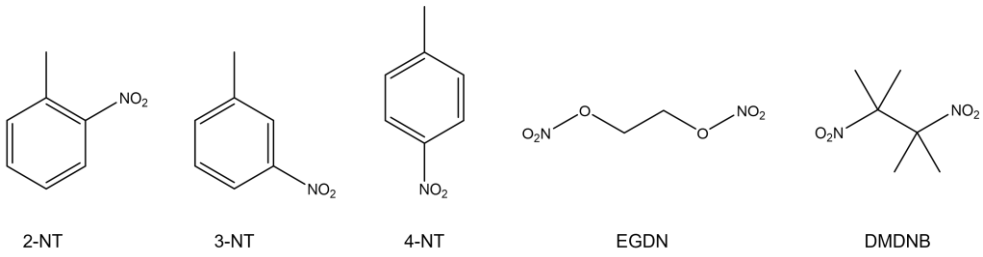

Figure 7. Chemical structure of the explosive taggants.

Table 3. Vapour pressure of some common explosives and explosive taggants at 25ºC.[43,44]

Substance	NM	NG	RDX	HMX	TNT	TATP	EGDN	DMDNB	4-NT
Vapor Pressure (atm)	$4.7\cdot10^{-2}$	$6.5\cdot10^{-7}$	$4.9\cdot10^{-12}$	$2.4\cdot10^{-17}$	$9.2\cdot10^{-9}$	$6.3\cdot10^{-5}$	$1.0\cdot10^{-4}$	$2.7\cdot10^{-6}$	$6.5\cdot10^{-5}$

1.8 Explosive detection techniques

Explosive detection has attracted considerable attention in homeland security, land mine detection, anti-terrorism operations, forensic research, human health, and environmental safety.[45,46]

However, as we have seen before, NO_2-based high explosives have a very low vapour pressure down to 10^{-7} atm at room temperature. As a result, only trace quantities of explosive molecules are found in air samples and making them extremely difficult to detect. For that purpose, commercially available explosives are formulated with volatile

molecules known as explosive taggants to enhance their detectability. To detect selectively trace amounts of explosives, different analytical tools are used for explosive identification and quantification.

1.8.1 Explosive detection by trained canines

Detection dogs are considered one of the most reliable methods for on-field explosive detection. It is possible due to the ability to detect three different types of compounds, which are directly related to the explosive molecule: the explosive itself, an explosive taggant or other minor compounds, and some product of the explosive decomposition.

Canines also show an extraordinary specificity, which means that they are able to distinguish between the analyte that it has been trained to detect and other similar targets, and sensitivity because their detection threshold has shown sensitivities below 10^{-16} M, but the sensitivity highly depends on their training.[47] Other drawbacks are related to the maintenance, the time-consuming training protocols and the training infrastructure, which makes it a rather expensive detection method.[48,49]

1.8.2 Instrumental detection techniques

Different analytical methods have been used to detect trace amounts of explosives in solid, liquid and vapour state.[20,50]

1.8.2.1 Chromatography-mass spectrometry

Chromatography consists of a group of separation techniques based on the different speeds of the components of a mixture when they travel through the column due to their different affinity between the mobile and the stationary phases. According to the physical state of the mobile phase, these techniques are classified as gas chromatography (GC), liquid chromatography (LC), and supercritical fluid chromatography (SFC).

Mass spectrometry (MS) is based on the separation and analysis of the ions of an organic molecule according to its mass-to-charge ratio (m/z). There are different mass analysers, such as quadrupole, ion trap, time-of-flight (TOF) and tandem based techniques.

Coupled techniques such as gas chromatography–mass spectrometry (GC–MS) when the analyte is volatile or liquid chromatography-mass spectrometry (HPLC-MS) have

been used to identify and quantify trace amounts of explosives because they combine the separation ability of chromatography with the sensitivity and selectivity of a mass spectrometer.[51,52,53]

However, most of the samples require some pre-treatment to remove some of the matrix compounds that could interfere in the analysis and to increase the selectivity and the concentration of the analyte.

1.8.2.2 Raman spectroscopy

Raman spectroscopy is based on the changes in vibrational levels when a molecule is irradiated with powerful radiation, normally a laser. As a consequence, the Raman spectrum provides information about the chemical structure of the analyte, which is specific for each analyte and therefore it consists of the fingerprint of the molecule. However, this technique is not adequate to determine trace amounts of analyte due to their low sensitivity. For that reason, an alternative to reach a lower limit of detection (LOD) is the Surface Enhanced Raman Scattering (SERS). It is based on an improvement of the response signal when the analytes are adsorbed on the nanoparticle surfaces, whether in solution or deposited on a substrate, and produces an alteration in the electronic states that induces a change in the polarizability of the molecule.[54,55]

1.8.2.3 X-ray diffraction (XRD)

X-ray diffraction (XRD) is a non-invasive tool, which provides information about the chemical structure of the samples. This technique is based on constructive interferences when a monochromatic X-ray beam impinges on the sample in the same angle as it is scattered. At this specific angle, the radiation, which obeys Bragg's law is scattered from each set of lattice planes of the sample toward the detector. XRD have been used for the explosive identification by using a spectra database to increase the effectiveness of the method.[56,57,58]

1.8.2.4 Electrochemical methods

The electrochemical methods are based on the measurement of the electron transfer processes due to a redox reaction, which has occurred at the electrode/solution interphase. These methods can be classified as conductimetric, amperometric or potentiometric depending on whether the variable is current, conductivity or potential

voltage, respectively. Nitro-explosive compounds have a particular redox character due to the presence of the NO_2 group in the molecule, which enables their electrochemical detection. Electrochemical systems offer fast response time with high sensitivity, but they are mostly applied to liquid-phase samples.[59,60]

1.8.2.5 Nuclear detection techniques

Nuclear methods are based on the analysis of the atomic nucleus to obtain information about the elemental composition of the molecule by measuring the radiation gamma or the emitted/transmitted neutrons. These methods are divided into two categories, those which use neutrons as an incident beam and those, which use other types of particles, such as protons or photons. When the sample impinges with a radiation source, they interact with the atomic nucleus of the sample, which allows to carry out an isotopic analysis to obtain an analyte fingerprint. Nuclear techniques have a great penetration capability due to the small probability of interaction between the incident beam and the nucleus particles, and high specificity, which makes them a useful tool for the detection of trace amounts of explosives in cargo ship containers, checked baggage, etc.[61,62,63] However, all of these techniques use radioactive isotopes as a source of radiation, which limits their applications due to the health and safety regulations.

Despite these techniques accomplish the requirements needed for the detection of trace amounts of explosive, such as high sensitivity, and selectivity, most of them are expensive and require bulky and sophisticated instrumentation, which limits their portability and on-field analysis. Because of these limitations, there is a constant search for a suitable sensing platform for different environments, from vehicle screening to strategic locations, such as airports and government buildings.

1.9 Explosive chemical sensors

A chemical sensor is a detection system, which indicates the presence or the absence of the target analyte due to the generation of a measurable response, which allows its identification and/or quantification.

Ideally, an explosive sensor should be small and compact to incorporate into portable devices and combine short response time and robustness, required for routine use in the field, with a wide linear range, low limit of detection, good sensitivity, and selectivity to detect trace quantities of explosive compounds. These requirements are very

challenging, especially because sensors should also be cost-effective and ready for mass production. During the last decade, strong attention of scientists has been focused on the development of sensors using nanomaterials, because of their outstanding optical, catalytic, electrical, and electrochemical properties. For this reason, they may offer many benefits, such as good portability, low-cost, high selectivity, and sensitivity.[64]

1.9.1 Optical sensors

Explosive sensors based on the electrochemical transduction mechanism are among the most preferred ones due to the redox properties of the NO_2-containing compounds and their easy operation, cost-effectiveness, high sensitivity, fast response, and suitability for portable devices.[65] Nevertheless, most of these sensors are limited to liquid phase detection.

Other approaches involve optical properties of nanomaterials such as absorbance (colourimetric) and fluorescence/photoluminescence. They show the same advantages as electrochemical sensors but they can be applied to vapour phase detection. Therefore, based on the optimal results obtained from the exposure of these types of sensors to different volatile organic compounds such as biogenic amines[66] or thiols as 2-mercaptoethanol,[67] they were proposed for the explosive detection.[68,69]

Moreover, the scientific and technological goal of the “High-selective nanoantenna for explosives detection” NATO project was based on developing novel sensitive elements based on nanosized artificial polymeric receptors with optical signaling capability for use in portable and inexpensive explosives detectors, which are capable of sensing trace amounts of explosive substances. For that reason, in this thesis, three different optical sensors were developed to detect and quantify trace amounts of explosive taggants in the vapour phase. Depending on the NP the optical response is generated due to different transduction mechanisms.

1.9.1.1 Localized Surface Plasmon Resonance (LSPR) sensing

Noble metal nanoparticles, such as Ag and Au, exhibit LSPR as the result of the interaction between the NPs and electromagnetic radiation with bigger or same wavelength as NPs size, which produces a resonance effect due to a collective oscillation of free electrons in the conduction band of the NP. Moreover, this phenomenon is

observed in the visible range, which allows the use of simple measurement methods.[70,71,72]

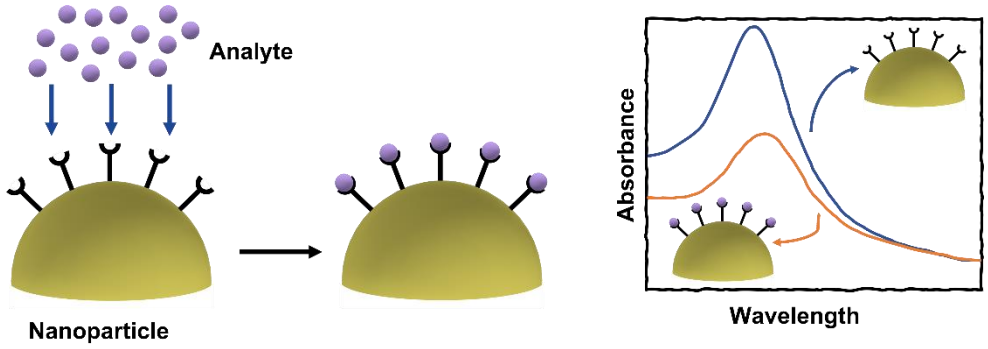

Figure 8. LSPR sensing mechanism.

The LSPR depends on the size, shape, and refractive index of the surrounding medium of the NPs. For that reason, the sensing mechanisms are based on the changes in the optical properties (LSPR intensity and linewidth and wavelength of the LSPR peak), which can occur when analyte molecules interact with the surface of the NPs (Figure 8).[73] These mechanisms consist of the variation of the refractive index on the surrounding medium of the metal surface,[74] the scattering at the NPs surface,[75] the NPs aggregation,[76] and the charge transfer between the NPs and the adsorbed analytes. [66,77]

1.9.1.2 Fluorescence sensing

Fluorescence-based sensors are employed to detect trace amounts of explosives and explosive taggants due to their advantages such as short response time, real-time response, low limit of detection (LOD) and high selectivity.[78] The sensing mechanism is mainly based on the changes in the fluorescence intensity (quenching or enhancement) when the analyte molecules interact with the fluorophores, as is shown in Figure 9.[30] The state of the art indicates that conjugated polymers,[79] nanoclusters,[80] metal-organic frameworks,[81] dendrimers,[42] luminescent quantum dots (QDs),[82] and hybrid perovskites,[83] among others,[84] have been used for the same purpose.

Fluorescence quenching mechanisms such as photo-induced electron transfer (PET), resonance energy transfer (RET), electron exchange, and intramolecular charge transfer (ICT) are predominant in the detection of the nitro-containing explosives. However, other mechanisms can be possible. When the NP is embedded into a polymer, the interaction

between the analyte and the surface of the NP can be possible if the analyte diffuses through the polymer. Consequently, this process produces a swelling, which affects the emission properties.

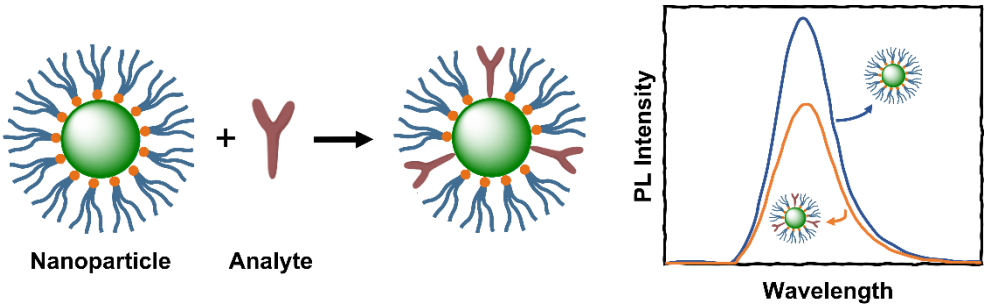

Figure 9. Fluorescence sensing mechanism.

1.10 Hybrid nanocomposites

Sensors based on NPs were used mainly in solution due to some drawbacks to deposit on a solid support such as NPs irregular distribution and poor mechanical properties.[85,86]

Nanocomposites consist of multicomponent materials in which at least one of the components is nanosized. In these materials, the NPs are incorporated into an organic or inorganic host matrix to improve their properties. In particular, polymer hybrid nanocomposites combine the optical properties of the NPs with the mechanical and thermal properties of the organic polymers such as flexibility, conductive/dielectric properties, good processability into thin films, etc. that makes possible the synthesis of thin films by conventional deposition techniques (spin-coating, inkjet printing, dip-coating, blade coating, etc).[86,87,88,89] Moreover, the chemical and thermal stability and the organization of the NPs are increased when they are embedded into the polymer matrix.

As we mentioned before, different techniques can be used to obtain thin films from precursor solutions. The deposition method, which is used in this PhD thesis is the spin coating. It consists of dropping a small amount of solution on a substrate and then, the substrate is rotated at high speed to obtain a homogeneous thin layer. Finally, to remove the remaining solvent and favour the adherence of the film to the substrate, it is baked on a hot plate. The thickness of the layer depends on the viscosity of the polymer, as well as the speed and time of rotation.

1.11 Molecularly imprinted technology (MIT)

One of the strategies to enhance the selectivity and sensitivity of optical sensors is the use of molecular imprinting approaches to generate artificial molecular recognition sites in a polymer.[90] In general, the conventional method of non-covalent MIPs synthesis consists of polymerizing the monomer and the cross-linker in the presence of template molecules. After that, the resulting polymer is washed with different solvents to remove the template and generate three-dimensional stereo-specific cavities (Figure 10A).[91,92,93,94]

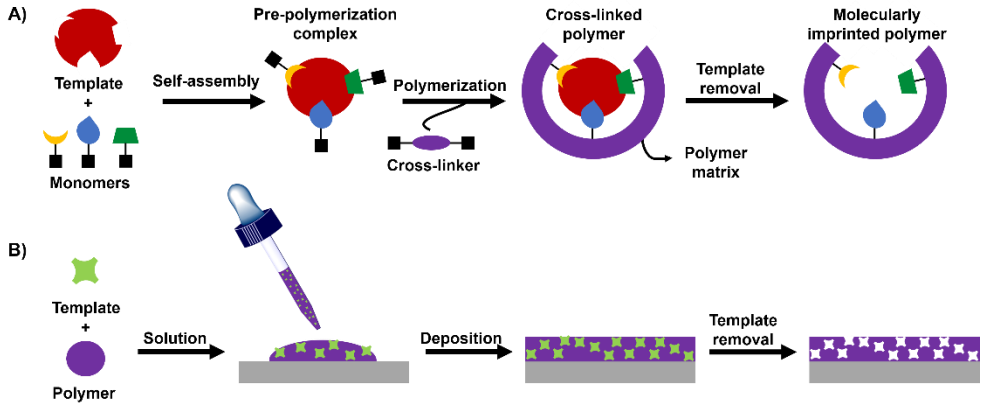

Figure 10. Synthesis of MIP by A) non-covalent method and B) encapsulation method.

In this work, the encapsulation method has been chosen to synthesize the MIP. As we can observe in Figure 10B, in this method the sensor is prepared by mixing the polymer with the template following a sol-gel or hydrothermal method.[90,95] When the template is removed from the polymer matrix, some nanocavities are generated in the polymer matrix.

The specific cavities in both methods have a similar size and shape as the template molecule and a chemical environment, which drive the molecular recognition phenomena.[96] In this way, the resulting molecularly imprinted polymer (MIP) would recognize and bind selectively only those molecules with similar size, shape, and functional groups as the template molecule as is shown in Figure 11.[97] Several authors have proposed different approaches toward the fabrication of MIP sensors for in solid state for explosive sensing[98,99] and another analyte sensing,[100,101] but all of them suffer from time-consuming and multistep procedures.

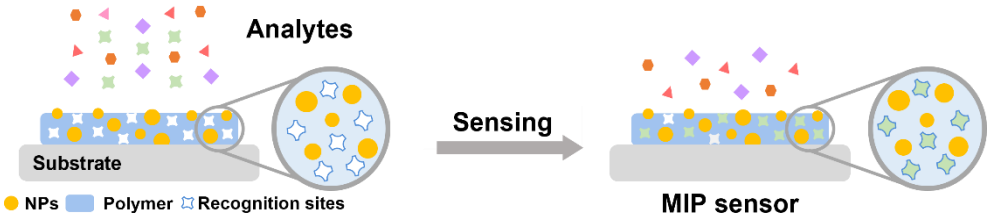

Figure 11. Sensing process of the molecularly imprinted polymer (MIP).

Chapter 2

Molecularly Imprinted Silver Nanocomposites

In this chapter, we report the synthesis of a solid-state plasmonic sensor based on a nanocomposite of Ag NPs embedded in a MIP for selective detection of 3-NT, an explosive taggant for TNT. In our approach, the in-situ synthesis of Ag NP and the molecular imprinting with 3-NT as a template take place simultaneously inside the polyethyleneimine (PEI) thin film during the baking step after spin-coating. The MIP sensor fabrication is done by a low cost, fast and scalable one-step procedure. We demonstrate the chemo-sensing capabilities of Ag-PEI MIP nanocomposite to 3-NT using the LSPR band intensity decay as a sensing parameter. The molecular imprinting approach results in a specific sensor response enhancement to the 3-NT, with a LOD of 54.8 ng 3-NT and a sensitivity of 24.0 ± 3.0%. We tested the MIP sensor specificity by comparing the sensor response to several NO_2-containing molecules. Ag-PEI MIP sensor demonstrated a robust, specific molecular recognition to 3-NT. Because the MIP nanocomposite sensor is easy-to-prepare, easy-to-use and inexpensive, these plasmonic sensors can be easily implemented with portable reading platforms into remote explosive detection and bomb disposal robots. Experimental results, discussions and conclusions of this chapter are entirely based on the article *"Molecularly Imprinted Silver Nanocomposites for Explosive Taggant Sensing"*.

2.1 Introduction

Noble metal nanoparticles (Au, Ag) have attracted much attention in sensing based on their optical properties due to the LSPR, which can be described as the resonant photon-induced collective oscillation of free electrons on metal NPs at a given resonant frequency. The excitation of LSPR bands of Au and Ag NPs shows a powerful light absorption and/or scattering in the visible, which strongly depends on their size, shape and surrounding medium (substrate, solvent, and adsorbates).[102,103,104,105,70,71] As a result, LSPR can be exploited as the transduction mechanism in high-performance sensing devices: the adsorption of molecules on the NP surface results in measurable spectral changes: wavelength and/or peak intensity of the LSPR spectrum.[106,107,108,109] Similar MIP sensors have been proposed to exploit surface plasmon resonance using noble metal thin films instead of NPs.[110]

A solution of polyethyleneimine (PEI), $AgNO_3$, and 3-NT as a template is spin-coated to fabricate the polymer-based solid-state explosive sensor in the vapour phase. The novelty of our approach is that Ag NP synthesis and molecular imprinting take place simultaneously inside the polymer in a one-step procedure during the baking step within a few minutes.[77] Secondary amine groups of PEI can reduce in-situ Ag(I) to Ag NPs,[87] and selective binding site generation occurs by the evaporation of the template. Moreover, PEI shows excellent film forming properties. The sensor fabrication is low-cost, straightforward, and very fast. This synthetic approach allows a tuneable control of both LSPR properties (peak wavelength, maximum intensity, and linewidth) and the sensor response to several analytes. We demonstrate the chemo-sensing capabilities of Ag-PEI nanocomposite to 3-NT. More interestingly, the MIP approach applied to the Ag-PEI nanocomposite results in a dramatic enhancement of its LSPR response to the target analyte, as compared to the Ag-PEI NIP sensor, and a robust specificity to 3-NT when exposed to vapours of 2,3-dimethyl-2,3-dinitrobutane (DMDNB), picric acid (PA) and 4-nitrophenol (4-NP). The sensor shows a LOD of 54.8 ng 3-NT, which is equivalent to 1.37 ng/mL and a sensitivity of 24.0 ± 3.0 %.

2.2 Experimental

2.2.1 Reagents and materials

PEI branched (average molecular weight 25 000, water-free), PA (98 %, moistened with water), DMDNB (98 %), and $AgNO_3$ were purchased from Aldrich. 3-NT (99 %) and 4-NP (99 %) were purchased from ACROS Organics. The chemical structure of the analytes of interest is depicted in Figure 12.

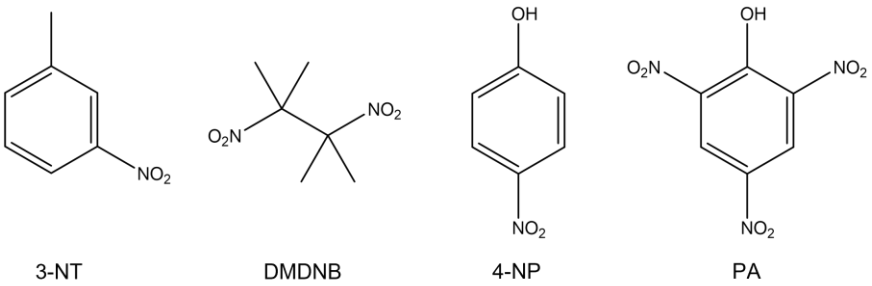

Figure 12. Chemical structure of the explosive taggants and analogues.

2.2.2 Nanocomposite synthesis and sensor fabrication

Two different nanocomposite precursor solutions were optimized by changing the amounts of PEI, $AgNO_3$, and 3-NT. Typically, the Ag-PEI MIP precursor solution consist of a solution of 1.33 wt. % of PEI, 0.03 M $AgNO_3$ and 10^{-3} M 3-NT in cyclohexanone/ethanol (1:2.5). The Ag-PEI NIP was prepared similar to the MIP, except that the template was not present in the precursor solution. Before coating, a glass slide substrate (1 cm^2) is ultrasonicated in a 3 M HCl solution for 10 min, rinsed with 3:1 isopropanol/acetone, dried with compressed air and exposed to UV/ozone cleaning for 10 min (Ossila Ozone Cleaner). The resulting precursor solutions are spin-coated on a glass substrate at 1000 rpm and baked between 120 and 240 ºC for 10 min to synthesize in-situ the Ag NPs inside the PEI.[87] The film thickness of the resulting sensors was measured to be around 90 nm using a mechanical profilometer (Veeco Dektak 150). Figure 14 illustrates all the steps involved in the generation of both Ag-PEI sensors.

2.2.3 Characterization techniques

The presence of Ag nanoparticles inside the PEI matrix was confirmed by UV-Vis spectroscopy with a reflectometer (Nanocalc 2000, Ocean Optics Inc.) to correlate their optical properties with the size and shape of NPs and their particle dispersion in the polymer matrix. The FTIR spectra were recorded to identify the organic structure of the sensor (FTIR Thermo Nicolet Nexus). The Ag-PEI thin films were also characterized by XRD (XPERT Pro, Panalytical). Transmission electron microscopy (TEM) studies of the particles were also carried out at an accelerating voltage of 100 kV using a JEOL 1010 microscope. TEM samples were prepared by ultrasonication in ethanol of small pieces of Ag-PEI nanocomposite coated on coverslips with the sensor. With this procedure, we obtained micrometre-sized fragments of the corresponding nanocomposites in suspension in ethanol. This suspension is dropped on a carbon-coated Cu grid. The microstructural information and chemical composition of the Ag-PEI sensors were carried out by HR-TEM (Tecnai G^2 F20 S-TWIN from FEI Company). The surface morphology of the nanocomposite patterns was characterized by atomic force microscopy (AFM system from Nanotec Electrónica S.L.).

2.2.4 Sensing protocol

The response of the Ag-PEI MIP/NIP thin films was investigated by exposing the sensors to a stream of 3-NT-containing water aerosol by bubbling a solution of 40 mL of 13.7 µg/mL (10^{-4} M) 3-NT in water using air as a gas carrier at room temperature for different times (Figure 13A).

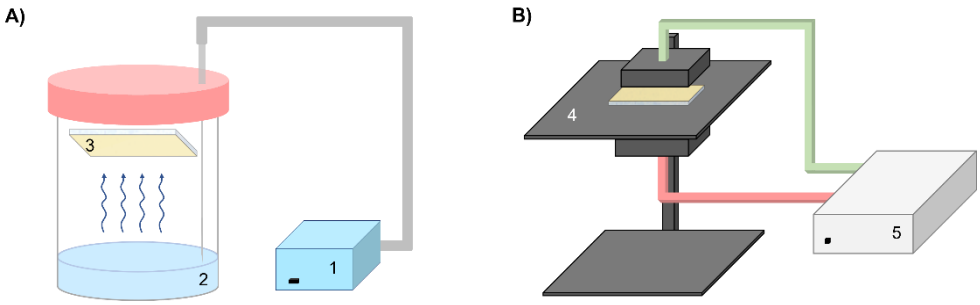

Figure 13. Schematic picture of A) the sensing system and B) the homemade experimental setup. The different elements of the sensing system and the setup are: 1) peristaltic pump; 2) analyte solution; 3) Ag-PEI sensor; 4) positioning system; 5) UV-Vis spectrophotometer.

The calibration curve was obtained using different 3-NT concentrations, from 10^{-10} to 10^{-2} M. To limit the experimental error, we always chose an area wherein the initial LSPR intensity was approximately the same value. All UV-vis spectra were carefully performed using a positioning system to measure at the same position to achieve accurate LSPR intensity values (Figure 13B).

2.3 Results and discussion

2.3.1 Synthesis and characterization of Ag-PEI NIP/MIP sensor

Figure 14 shows the steps involved in our approach to carry out the MIP nanocomposite synthesis. The in-situ synthesis of Ag NPs inside PEI and the molecular imprinting take place simultaneously by a one-step procedure. In the first stage, PEI, 3-NT, and $AgNO_3$ are dissolved in a 1:5 cyclohexanone/EtOH. The resulting solution is spin-coated on a glass substrate and baked, typically from 100 to 210 °C for several minutes. The in-situ synthesis of Ag NP takes place inside the polymer by the reduction of Ag(I) to Ag NPs by primary and secondary amine groups of PEI,[87] whereas the molecular imprinting occurs by the evaporation of the template during the baking step (encapsulation method).[90,95]

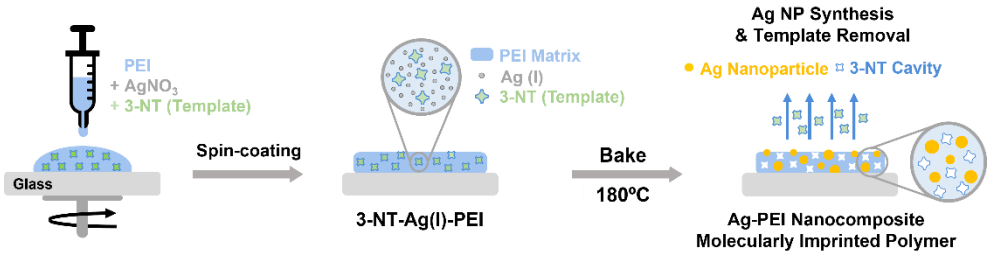

Figure 14. Schematic representation of the fabrication of the Ag-PEI MIP nanocomposite sensor.

PEI shows excellent film forming properties.[87] The synthesis of Ag NPs in the polymer matrix can be followed by UV-Vis spectroscopy. Figure 15A shows UV-Vis spectra of an Ag-PEI MIP baked at 180 °C for a different times. We observe that the reduction of Ag (I) to Ag (0) and the subsequent nucleation and growth of NPs in PEI is a fast reaction. As shown in Figure 15B, after only 15 s, a characteristic LSPR band absorption band appears at 415 nm with almost the maximum intensity. This LSPR band is attributed to spherical Ag NPs. From 15 to 600 s, the LSPR band remains practically constant in intensity but is red-shifted to 425 nm, and the absorbance linewidth strongly increases

from 40 to 76 nm due to the formation of larger NPs. This behaviour can be ascribed to a classical mechanism of nucleation and growth of NPs.[111,112] The size and shape of Ag NPs have a strong influence on the LSPR. Initially, nucleation takes place to produce nuclei or seeds that act as templates for crystal growth. In the in-situ synthesis approach, homogeneous nucleation occurs because Ag(I) is mixed at the molecular level with PEI, leading to nuclei uniformly distributed throughout the polymer film. The growth of NPs is autocatalytic and dependent on two mechanisms: the Ag(I) diffusion to the Ag nuclei surface and the surface reduction reaction. The glass transition temperature of the branched PEI is very low (T_g = -52ºC)[113] then, PEI films are in their rubbery state and behave like a liquid. For this reason, Ag (I) ions can diffuse within PEI with relatively good mobility, and NP can easily nucleate. As a result, Ag NPs synthesis in PEI follows a pseudo-first order rate reaction as shown in the similar in-situ synthesis of metal NPs in solid-state reactions.[114,115,116] After 10 minutes, we can consider that the reduction of Ag(I) to Ag(0) in PEI is finished. Unreacted Ag(I) in the surroundings of Ag NPs could reduce the sensing capabilities for a given analyte. Ag-PEI NIP films follow a very similar tendency: the addition of 3-NT in the film hardly affects the synthesis of Ag NPs.

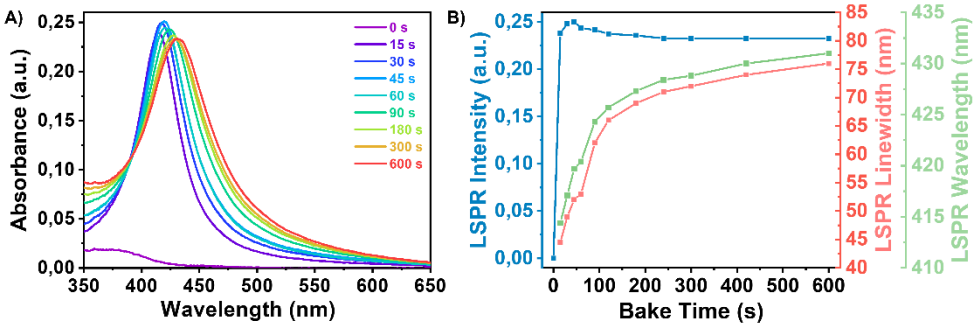

Figure 15. A) UV−vis absorbance spectra of Ag-PEI MIP films baked at 180 °C for different baking times. B) Evolution of the LSPR band (intensity, bandwidth, and wavelength) of Ag-PEI MIP films baked at 180 °C for different baking times.

Several reactions take place during the in-situ synthesis of Ag NPs. Primary and secondary amines of the branched PEI polymer chains play a determinant role in reducing Ag (I) to Ag (0). The FTIR spectra in Figure 16A show how the amine groups of PEI change after the in-situ synthesis of Ag NPs and check whether the molecular imprinting is successful, and the template (3-NT) is removed after the baking step. We observe that both Ag-PEI MIP and Ag-PEI NIP show very similar FTIR spectra. Unlike

PEI, NIP and MIP show a broad band at 3700 cm^{-1}, which may be attributed to N–H stretching vibration from amides. Besides, the band at 1500 cm^{-1} may also be assigned for C=O stretching and N-H bending of amides. The formation of amides is attributed to the oxidation of amines when Ag(I) atoms are reduced to Ag(0), which is the first step of the NP growth process.[117] This process then consists of the nucleation of new Ag nanoclusters and their growth via agglomeration or Ag(0) addition to form the Ag NPs. The final step involves passivation with the capping agents. Amino and amide functional group of branched PEI has an essential role in the capping and stabilization of Ag NP.[118,119] Additionally, we observe a peak at 1750 cm^{-1} from C=N stretching of imine or C=N-O stretching of oxime from the in-situ synthesis of Ag(0). The band at 2350 cm^{-1} is observed in both Ag-PEI MIP and NIP, which is characteristic of CO_2. This may indicate a superior CO_2 adsorption of Ag-PEI nanocomposite in comparison to PEI. As reported elsewhere, Ag NPs also show good surface affinity towards CO_2 capture.[120]

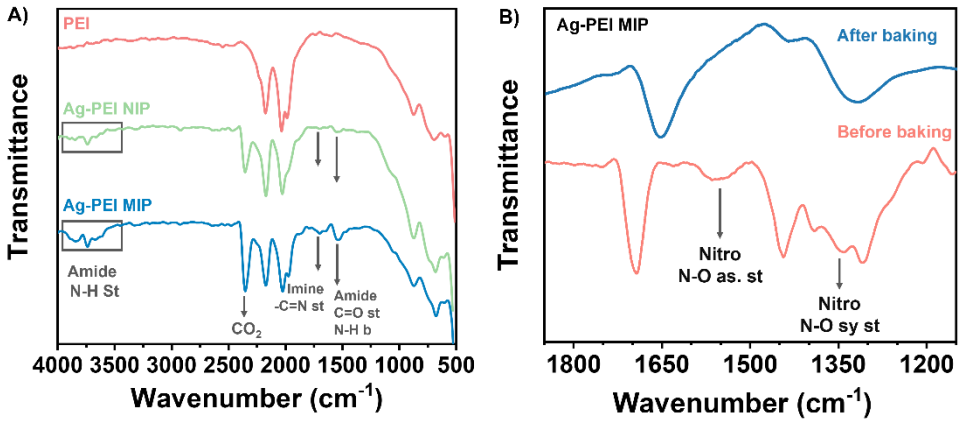

Figure 16. A) FTIR spectra for PEI, Ag-PEI MIP, and Ag-PEI NIP (Ag-PEI MIP composition: 1.3 wt % PEI, 0.03 M $AgNO_3$, and 10^{-3} M 3-NT; Ag-PEI NIP composition: 1.3 wt % PEI and 0.03 M $AgNO_3$; baking conditions: 180 °C for 10 min). B) FTIR spectra for Ag-PEI MIP before and after baking.

However, either PEI and Ag-PEI (MIP and NIP) show two bands at 2200 and 2000 cm^{-1} region arising from N=C=O and C=C=N stretching modes of isocyanate and ketenimide, respectively. These functional groups may be formed when amines react with CO_2.[121] The Ag-PEI MIP spectrum does not show traces of the typical N-O asymmetric and symmetric stretching vibration bands around 1550 and 1350 cm^{-1} associated to the NO_2-containing compound; hence, this absence confirms that 3-NT is completely removed after the baking process, forming the MIP nanocomposite. In Figure 16B, we show FTIR

spectra of Ag-PEI MIP before and after baking to show how template molecules are removed. We clearly observe the presence of typical asymmetric and symmetric N-O stretching vibrations at 1550 and 1340 cm^{-1}, respectively, before baking.

XRD further confirms the in-situ synthesis of Ag NPs inside PEI. Figure 17 shows the XRD pattern of the Ag-PEI nanocomposite and PEI thin films. Both Ag-PEI MIP and Ag-PEI NIP show a significant peak at 38.1º, corresponding to the (111) crystal plane of the face-centered cubic structure of silver nanocrystals (JCPDS 04-783). The broad diffraction peak centered at 25º is attributed to neat PEI. The average size of Ag NPs in Ag-PEI can also be determined by the Scherrer equation applied to the (111) reflection plane. We obtain values of 6.7 ± 0.6 nm for Ag-PEI MIP and 6.9± 0.8 nm for Ag-PEI NIP.

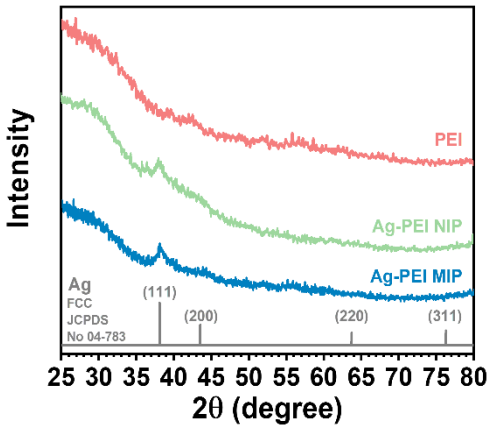

Figure 17. XRD spectra for PEI, Ag-PEI MIP, and Ag-PEI NIP.

The transmission electronic microscopy (TEM) image (Figure 18A) shows spherical Ag NPs uniformly distributed within the polymer matrix for both Ag-PEI MIP and the corresponding Ag NP size distribution. We measure an average size of 6.3 ± 1.3 nm and 6.2 ± 1.1 nm for Ag-PEI MIP and NIP (histogram in Figure 18B). These sizes are in good agreement with those measured by XRD. From the HRTEM image (Figure 18C), we measured a lattice spacing of 2.5 Å for Ag-PEI MIP, which corresponds again to the interspacing of the (111) plane measured by XRD (2.4 Å). Figure 18D shows a compositional mapping of the Ag-PEI MIP nanocomposite. Elemental mapping confirms the expected elements: Ag, C (mainly from C-coated Cu TEM grids), and N (from PEI). Atomic composition clearly shows how Ag NPs are homogeneously distributed inside the PEI film.

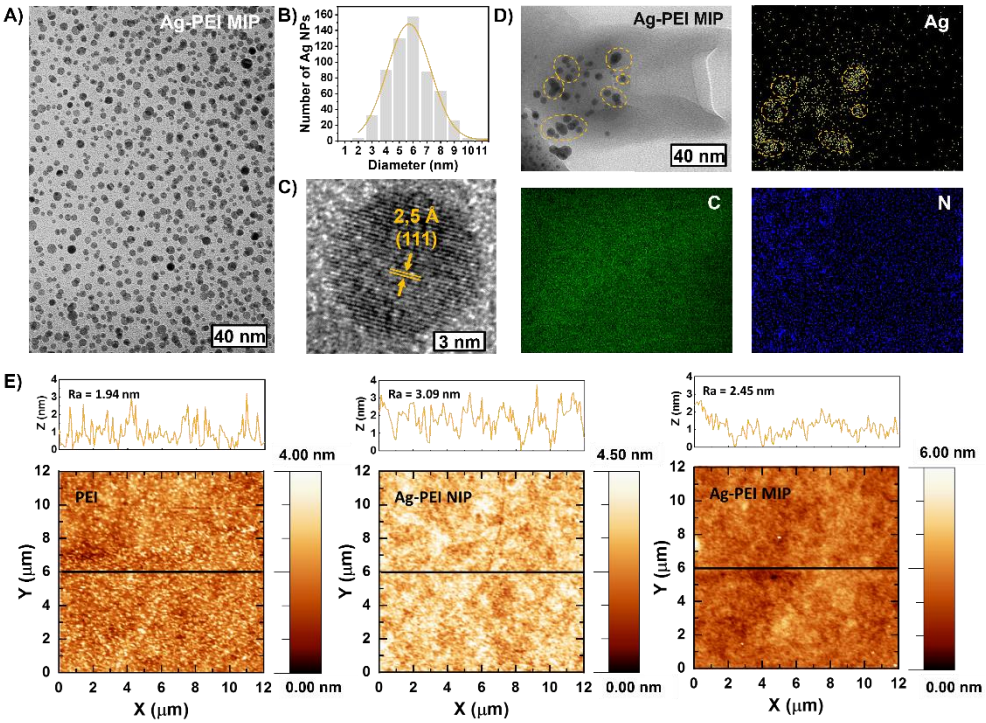

Figure 18. A) TEM B) Ag NP Size distribution C) HRTEM, and D) Mapping of Ag-PEI MIP. E) AFM images showing the morphology change from PEI (left panel) to Ag-PEI NIP (center panel) and Ag-PEI MIP (right panel) films.

The surface morphology of MIP and NIP Ag-PEI nanocomposite films was characterized by AFM in comparison to a PEI film (Figure 18E), from left to right panels, respectively). MIP and NIP Ag-PEI films exhibit a homogenous and smooth surface morphology with an average surface roughness (R_a) of 2.45 and 3.09 nm, respectively, whereas the neat PEI film shows the smoothest surface with a R_a of 1.94 nm. The difference in the roughness ranges only from 0.5 to 1.1 nm and is ascribed to the presence of the Ag NPs, even if one would expect that Ag NPs of 6 nm in diameter would affect more significantly the surface roughness. Therefore, this result suggests that Ag NPs are not located at the surface, but mainly embedded inside the PEI matrix. Ag NPs are probably strongly immobilized inside the PEI matrix by the amino and amide groups of PEI and do not tend to migrate to the surface. Amino groups have been reported to play an essential role in the immobilization of Ag NP.[118,119] The different surface roughness values of Ag-PEI MIP and NIP may also suggest that the imprinting effect of 3-NT enhances the binding properties that already exist in Ag-PEI NIP to immobilize Ag NPs.[122]

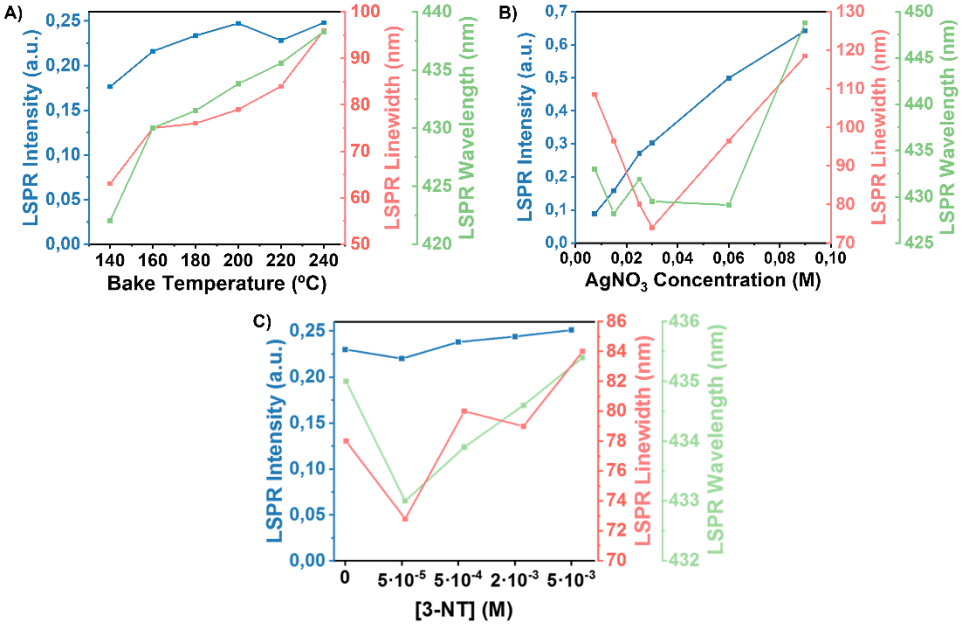

Figure 19. Evolution of LSPR band (intensity, bandwidth, and wavelength) of Ag–PEI MIP films baked for 10 minutes for different A) baking temperatures (1.3 wt % PEI, 0.03 M $AgNO_3$, and 10^{-3} M 3-NT), B) $AgNO_3$ concentration (1.3 wt % PEI and 10^{-3} M 3-NT at 180 ºC), and C) different 3-NT template concentrations (1.3 wt % PEI and 0.03 M $AgNO_3$ at 180 ºC).

The baking temperature plays a determinant role in the in-situ synthesis of Ag NPs in PEI thin films. Figure 19A shows how LSPR band (intensity, linewidth, and wavelength) of Ag–PEI MIP films prepared after annealing at different temperatures for 10 min. As shown in Figures 18A and 18B, the LSPR intensity of Ag-PEI increases notably from 140 to 180 °C of baking temperature, because the reduction reaction is not complete. From 200 ºC, the LSPR does not change significantly in intensity, indicating that the reduction of Ag (I) to Ag (0) NPs is complete after annealing for 10 min. However, the LSPR band redshifts 6-7 nm several and linewidth strongly increases from 76 to 96 nm. Both effects can be ascribed to the formation of larger NPs at the expense of small ones by the Ostwald ripening mechanism, other than increasing the size dispersion and, eventually, forming non-spherical shapes at the highest temperatures.[77] We observed a very similar tendency in the synthesis of Ag-PEI NIP films, in which the FWHM increases significantly from 73 to 127 nm.

The $AgNO_3$ concentration also significantly influences the optical properties,[77,87] as shown in Figure 19B. Particularly, we observe a correlation between the growth of the

LSPR peak intensity and the $AgNO_3$ concentration. In contrast, its linewidth first decreases (uniform size dispersion of spherical NPs) and again increases above 0.03 M (wide range of sizes and shapes). Finally, the influence of different concentrations of the template molecule (3-NT) on the in-situ synthesis of Ag NPs inside PEI-MIP was practically negligible, at least from the point of view of the LSPR spectrum associated to the Ag-PEI MIP nanocomposite.

Ideally, the Ag-PEI optical sensor should have an LSPR band with a noticeable intensity and a narrow linewidth. Any minimal change in the surrounding of the Ag NPs will lead to a measurable change on the LSPR band (peak wavelength shift and peak intensity decrease and/or linewidth increase, even if this parameter will have a direct influence on the peak intensity). Apart from that, the reduction of Ag(I) to Ag(0) must be complete, because the presence of Ag(I) in the surroundings of Ag NPs would reduce the sensing capabilities for a given analyte. Based on these requirements, the Ag-PEI nanocomposite fulfils such optimal optical properties for a 0.03 M $AgNO_3$ concentration and a bake at 180 °C for 10 min. Moreover, the template concentration (3-NT) in the molecularly imprinted nanocomposite does not significantly change its optical properties (Figure 19C). Thus, the ideal 3-NT concentration must be determined by performing sensing tests.

2.3.2 LSPR Sensing of 3-NT in Vapour Phase.

The response of the Ag-PEI MIP/NIP thin films was determined by exposing the sensors to a stream of 3-NT-containing water aerosol by bubbling a solution of 13.7 µg/mL 3-NT in water using air as a gas carrier. Figure 20A shows the evolution of the absorbance spectrum of the MIP sensor upon exposure to 3-NT for different times. As can be observed, the LSPR band is sensitive to the adsorption of 3-NT molecules on Ag NPs. The LSPR of the Ag-PEI sensor significantly changes in intensity and slightly changes the linewidth when exposed to the analyte for a given time. The LSPR intensity is, therefore, chosen as the most sensitive parameter to monitor the sensing performance of Ag-PEI. Figure 20B and 20C shows the real-time response of the MIP and NIP sensors upon exposure to 3-NT and water using LSPR intensity and linewidth as sensing parameters. Ag-PEI's response to water vapour is negligible, which indicates no interaction between H_2O and Ag NPs in PEI, whereas MIP sensors exhibited a significantly higher response to 3-NT than NIP sensors. This confirms that the proposed molecular imprint approach is successful. After 180 min, the LSPR peak intensity for the

MIP sensor is 54% of the initial intensity and shows an increase in the linewidth of 9 nm, while the NIP sensor only shows a decrease to 85% of the initial LSPR intensity and a linewidth increase of only 4 nm. The gradual intensity decay of the LSPR in both MIP and NIP sensors is explained by an increase of the attached 3-NT molecules on the surface of Ag NPs in the PEI matrix.

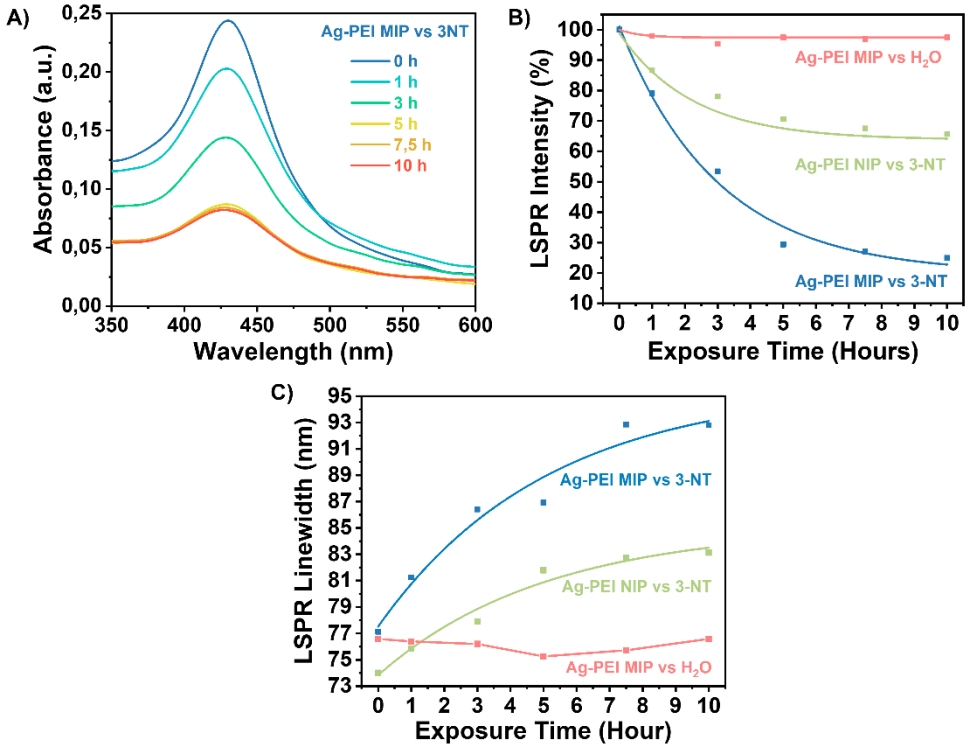

Figure 20. Ag-PEI MIP and NIP sensor response to 3-NT (vapour of a 13.7 µg/mL 3-NT) for different exposure times. A) UV-vis spectra of the Ag-PEI MIP sensor for different exposure times to 3-NT. B) LSPR intensity and C) linewidth response of Ag-PEI MIP and NIP sensors to 3-NT and water (Ag-PEI MIP composition: 1.3 wt % PEI, 0.03 M $AgNO_3$, and 10^{-3} M 3-NT; baking conditions: 180 °C for 10 min).

When molecules chemically bond to the surface of Ag NPs, two possible mechanisms can explain the LSPR decay (increase in linewidth and decrease in intensity).[123] The first one is the decrease in the electron density in the valence band of Ag NPs: 4d electrons of the silver atoms can be transferred to electron-accepting molecules, leaving a lower concentration of free electrons in the Ag NP for the LSPR. This mechanism influences the LSPR intensity. The second mechanism consists of the increase of the plasmon

resonance damping constant (scattering) when surface adsorbates induce electric dipoles (charge localization) at the Ag NPs surface. This mechanism would result in changes in the LSPR linewidth. Both mechanisms seem to be present in the interaction between 3-NT and Ag NPs, given that the LSPR linewidth increases monotonically but at a slower rate (a factor 1.19, from 77 to 92 nm) than the decrease in the peak LSPR intensity (a factor 3.00, from 0.24 to 0.08 in arbitrary units of absorbance), which would indicate that the charge transfer mechanism plays the main role. 3-NT is a π-electron acceptor molecule, because NO_2 is a strong electron-withdrawing group that makes the aromatic ring very electron-poor relative to benzene. The interaction between the Ag NPs and 3-NT molecules is via π-donor-acceptor charge transfer, which is in good agreement with the literature.[124,125,126] The analyte binding is almost irreversible: 3-NT cannot be desorbed to return the sensor to its initial state. However, this is not a limitation because these sensors are easy-to-prepare, easy-to-use, and inexpensive, which forms the basis of a fully disposable sensing platform technology.

The real-time kinetic response of both sensors to a vapour of 3-NT aqueous solution can be represented as a function of exposure time using the LSPR intensity and linewidth (Figure 20B and 20C) as a response variable. The following saturating function can fit the experimental behaviour: $A_t = A_\infty + B \cdot e^{-kt}$, where A_t is the absorption intensity at a given time, A_∞ is the saturation LSPR intensity, and k is the binding rate constant. Analyte binding to Ag NPs is a strongly time-dependent phenomenon determined by the vapour-phase analyte transport to the sensor surface and the subsequent chemical interaction rate.[77] The Ag-PEI sensor is exposed to a stream of 3-NT-containing water aerosol. Branched PEI is a hydrogel that can swell when exposed to an aqueous medium.[127] Here, water can help the 3-NT diffusion inside the Ag-PEI nanocomposite to improve the 3-NT adsorption onto Ag NPs. The binding rate (slope of the curve at any point) mainly depends on the quantity of accessible Ag NPs (binding sites) embedded into the PEI matrix and the analyte concentration. The molecular imprinting approach with 3-NT increases not only the surface area and accessibility of analytes to the binding sites but also may allow for the tunability of surface properties such as the wetting properties, enhancing the diffusion of 3-NT-containing water aerosol throughout the sensor.[128] The Ag-PEI sensor presents a cumulative response to 3-NT over time until most binding sites are occupied. The highest binding rate is achieved at the beginning of the reaction when all the binding sites are free. As a result, the relative importance of mass transport and analyte-Ag NP interaction can change during the sensing: analyte transport to the sensor can be limited at the beginning of the sensing test. In contrast, the interaction analyte-Ag

NP limits the observed binding rate at later stages, because most of the binding sites are occupied. Most of the analyte molecules accumulate on the binding sites near the surface of the sensor films, avoiding the accessibility of target molecules to Ag NPs located in the innermost areas of the thin films.

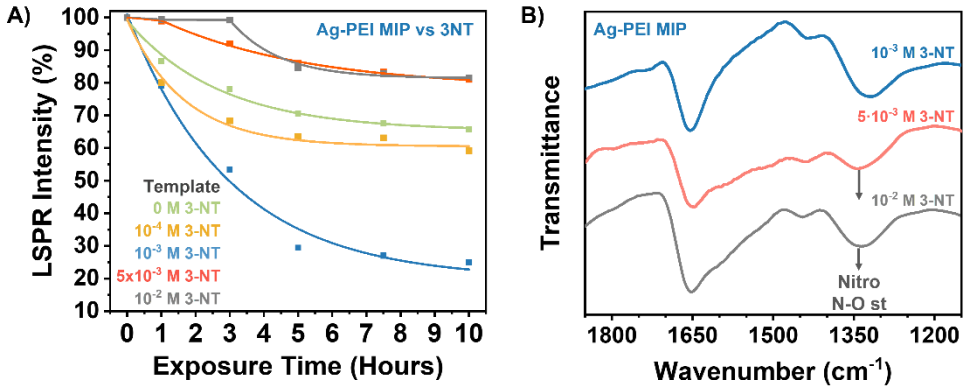

Figure 21. A) Real-time response of Ag-PEI sensor imprinted with different template concentrations upon interaction with the vapour of 13.7 µg/mL 3-NT. B) FTIR spectra for Ag-PEI MIP imprinted with different template concentrations (Ag-PEI MIP composition: 1.3 wt % PEI and 0.03 M $AgNO_3$; baking conditions: 180 ˚C for 10 min).

The concentration of the template plays a critical role in the sensing performance of the MIP sensor. Figure 21A shows how the response of Ag-PEI MIP nanocomposite changes significantly depending on the concentration of template molecules. The best MIP sensor response to 3-NT is obtained with a 10^{-3} M 3-NT concentration. LSPR peak intensity decreases from 70.6 % for Ag-PEI NIP (0 M 3-NT) to 29.4% for Ag-PEI MIP with 10^{-3} M 3-NT, after an exposure time of 5 hours. As the template concentration increases up to 10^{-3} M, more template cavities are created, and analyte binding sites are more accessible. However, the sensor response drops dramatically from $5x10^{-3}$ M template concentrations. FTIR spectra (Figure 21B) confirms an ineffective removal of the template. From $5x10^{-3}$ M, we observe typical N-O symmetry stretching vibration band at 1340 cm^{-1}, which is associated to the NO_2 of 3-NT. The removal of the template is an essential step in the molecular imprinting process for a suitable generation of the template cavities. At sufficiently high concentration, the segregation of 3-NT within the PEI thin film can occur, which in turn can favour the formation of intermolecular forces between 3-NT molecules that hinder evaporation, especially when the boiling temperature of the 3-NT is 232 °C, that is, higher than the baking temperature.

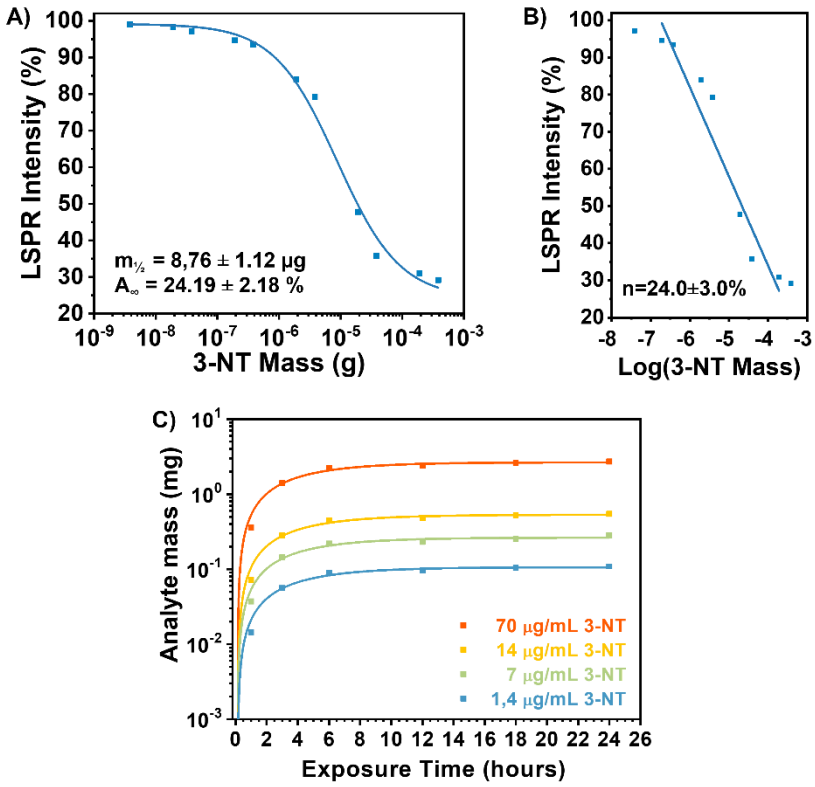

Figure 22. A) Calibration curve of the Ag–PEI MIP sensor. Absorption decay response as a function of the 3-NT concentration for an exposure time of 5 hours. B) Linear dependence and the corresponding regression line of the sensor response. (Ag-PEI MIP composition: 1.3 wt % PEI, 0.03 M $AgNO_3$, and 10^{-3} M 3-NT; baking conditions: 180 ºC for 10 min). C) Amount of 3-NT in vapor phase for different concentrations and times.

Figure 22A shows the Ag-PEI MIP sensor response to different amount of 3-NT after an exposure time of 5 hours. The mass of 3-NT has been determined by gas chromatography (Figure 22C). The calibration curves for analyte binding assays are generally characterized by a sigmoidal relationship between the sensor response and the analyte concentration. The four-parameter logistic (4PL) function (Equation 2.1) was used for fitting the concentration-response curve because it is recognized as the reference standard for immunoassays such as ELISAs or dose-response curves.[129]

The equation describing the 4PL function is[130]

$$A = A_{\infty} + \frac{(A_0 - A_{\infty})}{1+(m/m_{1/2})^s} \qquad \text{Eq. 2.1}$$

where A is the LSPR intensity response, A_∞ is the response at infinite analyte concentration, A_0 is the response at zero analyte concentration, m is the analyte concentration, $m_{1/2}$ is the concentration of analyte necessary to produce a response of 50 %, and s is the slope at $m_{1/2}$ of the calibration curve.

From Figure 22A, we can determine an LOD of the Ag-PEI MIP sensor to 3-NT around 54.8 ng, which is equivalent to 1.37 ng/mL (1.37 ppb) or 10 nM (for a sample volume of 40 mL). 3-NT has a vapour pressure of 0.1 mmHg (20°C), which corresponds to a concentration of 10^{-6} M. Therefore, the LOD of the Ag-PEI MIP sensor is two orders of magnitude lower than the 3-NT concentration.

From the calibration curve, we can also determine the binding affinity (K_A), which is the equilibrium binding constant and measures the propensity of the analyte to bind reversibly to the sensor. Under the assumption of a linear relationship between sensor occupancy and response, binding affinity is equal to the inverse of $m_{1/2}$.[131,132] Thus, we found $m_{1/2}$ = 8.76 ± 1.12 µg and $K_A = (1.10 \pm 0.89) \cdot 10^5$ g^{-1}. The higher the value of K_A, the higher affinity between sensor and analyte, and the less analyte is required to achieve 50% occupancy of the sensor's binding sites. We found a linear response range for 3-NT of three orders of magnitude, from $2 \cdot 10^{-7}$ to $2 \cdot 10^{-4}$ g. The sensitivity was determined to be 24.0 ± 3.0 % from the linear regression slope of the calibration curve shown in Figure 22B. Here the sensitivity is defined as the change in the LSPR intensity per order of magnitude of the analyte mass. High sensitivity without saturation is the key to a wide linear range. An ideal sensor is sensitive to low analyte concentrations without saturating at high concentrations. The maximum sensitivity of a sensor is attained within the linear response range. A wide linear range of detection is important for accurate quantification of analytes. Out of the linear range, the sensor shows low sensitivity and response do not reflect the sample concentration compromising quantification accuracy. Below the linear response range, the analyte concentration is too low to produce a measurable change in the LSPR band. The observed LSPR changes present great uncertainty because they cannot be distinguished from noise. Above the linear response range, sensor saturation may occur. Upon exposure to high concentrations, the analyte molecules accumulate on the sensor's surface, preventing accessibility of target molecules to Ag NPs located in the innermost areas.

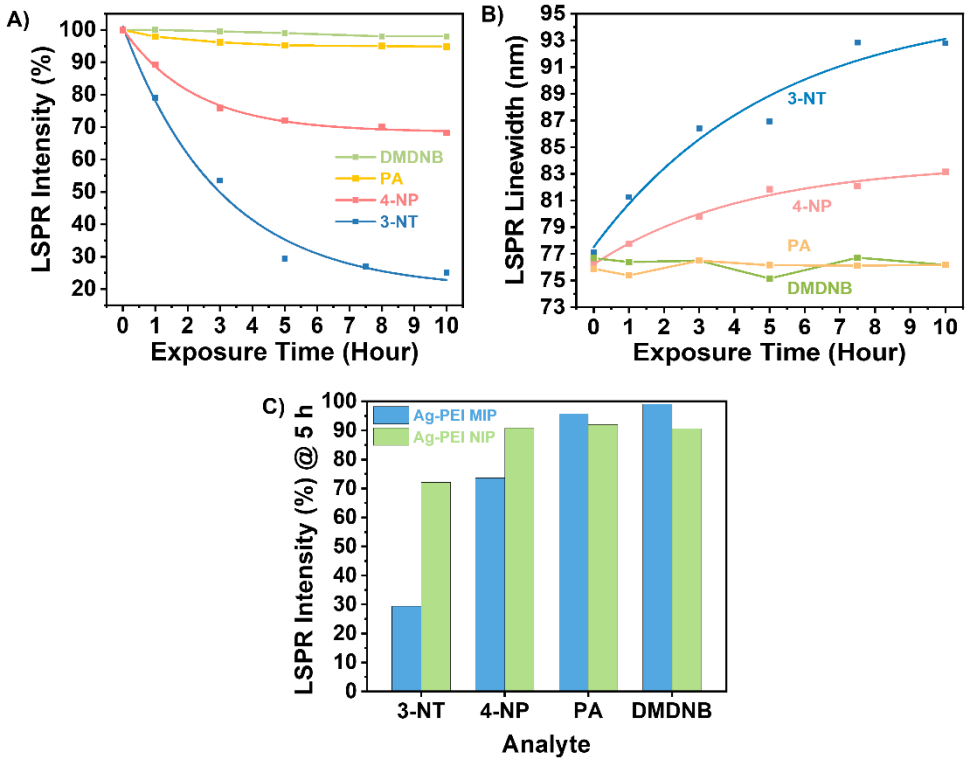

Figure 23. Selectivity of Ag-PEI sensor. A) Real-time response of Ag-PEI MIP to vapours of a 13.7 µg/mL aqueous solution of 3-NT, DMDNB, PA and, 4-NP; B) Linewidth response of Ag-PEI MIP sensors to vapours of a 13.7 µg/mL aqueous solution of 3-NT, DMDNB, PA and, 4-NP; C) MIP and NIP sensor response to 3-NT, DMDNB, PA, and 4-NP after 5 hours.

To further study the molecular recognition properties of Ag-PEI sensor, the selectivity of 3-NT-molecularly imprinted Ag-PEI was investigated with different nitro-compounds. Figure 23A shows the real-time Ag-PEI MIP response to 3-NT, 4-NP, DMDNB, and PA. The sensor exposure to DMDNB and PA produces a negligible decay in the LSPR intensities (90-95 %), but a moderate LSPR change for 4-NP (73%), and as shown above, the strongest response is observed for 3-NT (29.4%). The results showed that the Ag-PEI MIP nanocomposite recognizes and selectively targets 3-NT with respect to the other analytes. Again, the LSPR intensity decreases at a faster rate than the increase in the LSPR linewidth (Figure 23B). Therefore, we chose LSPR intensity as the sensing parameter to follow. In Figure 23C, we compare sensing performance of MIP versus NIP. The exposure of Ag-PEI NIP to various NO_2-containing compounds shows low non-specific response before molecular imprinting. Our molecular imprinting approach

provides a great specific molecular recognition to 3-NT and a certain selectivity towards 4-NP with respect to PA and DMDNB. This is somehow expected because 3-NT and 4-NP and have a similar molecular structure (toluene vs phenol) in terms of size and volume.

2.4 Conclusions

We reported a new approach to the fabrication of a MIP nanocomposite sensor based on Ag NPs embedded in PEI and 3-NT as a template for detection and quantification of trace amounts of 3-NT. Both the in-situ synthesis of Ag NPs and molecular imprinting takes place simultaneously during the baking step after the deposition. This nanocomposite combined the optical properties of the silver NPs with the characteristics of the MIP. Ag-PEI MIP sensors show a significantly higher response to 3-NT than NIP sensors. This confirms that the proposed molecular imprint approach is successful. The MIP sensor provides a great specific molecular recognition to 3-NT and a certain selectivity towards 4-NP with respect to other analytes, as PA and DMDNB. We found an LOD to 3-NT of 54.8 ng, which is equivalent to 1.37 ng/mL (1.37 ppb) or 10 nM. We also observe a linear sensing behaviour within a concentration range between $2 \cdot 10^{-7}$ and $2 \cdot 10^{-4}$ g, which allows us to use it as a quantitative sensor for 3-NT. Further research is needed to improve the sensor response time from hours to minutes. This may be accomplished by enhancing the analyte transport to the binding sites of MIP Ag-PEI by operating at higher temperature. This will lead to faster response times, because of the Arrhenius law.[133] Similarly, operating with higher analyte vapor pressures could also accelerate the sensor response time. However, long response time may not be limiting for certain applications such as in sentinels in cargo ship containers, for example.

This work confirms that the molecularly imprinted PEI containing metal NPs can be used as plasmonic optical sensors for 3-NT. We believe that the Ag-PEI MIP nanocomposite can be the basis for the development of a plasmonic sensor to perform chemosensing in security (i.e. detection of explosives and chemical weapons). Giving that MIP nanocomposite sensor is easy-to-prepare, easy-to-use and inexpensive, simple and cost-effective optical devices can be easily implemented with portable reading platforms.

Chapter 3

Luminescent CdSe Quantum Dot Arrays

Chemical sensors based on fluorescent quantum dots have attracted intense interest because of their excellent optical and electronic properties compared to the routinely employed fluorescent organic dyes. This study reports a CdSe QD-polymer-based luminescent chemosensor, which is based on an array containing either green-emitting or red-emitting CdSe QDs embedded in polycaprolactone (PCL) as a polymer host matrix. We evaluate the sensing capability of the nanocomposites by exposing both sensors to vapours of explosive taggants, explosive-like molecules and some common solvents. Both nanocomposites exhibit a very fast response time < 30s. The limit of detection of the sensors for 3-nitrotoluene, 4-nitrotoluene 2,3-dimethyl-2,3-dinitrobutane and picric acid was found to be 0.055 ng, 2.7 ng, 0.7 ng and 916.4 ng respectively. The sensor array constitutes a powerful tool to discriminate between explosive taggants (3-nitrotoluene, 4-nitrotoluene and 2,3-dimethyl-2,3-dinitrobutane) and shows specific molecular recognition towards picric acid. This type of miniaturized luminescent QD-based nanocomposites might form the basis of a sensing platform technology to perform effective chemical detection and identification of explosive taggants for preblast and postblast. Experimental results, discussions and conclusions of this chapter are entirely based on the article *"Luminescent CdSe Quantum Dot Arrays for Rapid Sensing of Explosive Taggants"*.

3.1 Introduction

Explosive sensors based on quantum dots (QDs) have been studied because of their excellent properties such as photoluminescence quantum yield (PLQY), easiness surface functionalization with different ligands, size-tuneable emission, good solution processability and photostability.[134,135] Moreover, these materials can be used in other applications such as photodetectors,[136,137,138] LEDs,[139] photocatalysts,[140] and solar energy converters.[141] To increase the mechanical properties and the stability of the solid-state QDs sensors, the QDs can be embedded into a polymer matrix and combine their properties to approach multifunctional materials. [86,142,143] Moreover, the possibility of the QD functionalization with the desired ligands helps to obtain a homogeneous dispersion inside the polymer and makes them an excellent active material to build a sensing platform. The transduction mechanism of the sensor is based on changes in the QD emission when analytes interact with the QD surface. Because the PL of QDs is very sensitive to any change in their surroundings, eventual chemical or physical interactions between the analyte and the QD surface may result in noticeable changes in the PL parameters such as the peak wavelength, intensity, and bandwidth.[144] For that reason, QD nanocomposites have been reported to sense humidity,[145] temperature,[146] metal ions,[147] amines,[67] thiols,[67] nitro-compounds,[148,149] providing fast response time, high selectivity and sensitivity. Depending on the functionalization of the surface of the QDs, the sensor's sensitivity can also be improved.[150] For instance, Freeman et al.[151] synthesize NADH-capped CdSe/ZnS QDs to detect 1,3,5-trinitrotriazine (RDX) in solution with a limit of detection of 0.1 nM. The authors reported that the Zn^{2+} ions of the QDs shell could activate the reduction of the RDX by NADH and transform it into the non-fluorescent NAD^{+}-CdSe/ZnS form. Komikawa et al.[152] reported the application of peptide-modified CdTe/CdS QDs in an aqueous solution for TNT detection with high sensitivity and selectivity; after a few seconds, the fluorescent quenching can be observed by a naked eye. As can be observed, due to the low volatility of the explosives, most of the research in the state-of-the-art literature is based on solution detection.

Nevertheless, detecting explosives and explosive-like molecules directly on-field is vital to developing optical sensors for vapour phase sensing. Wu et al.[153] fabricated a sensor array of ZnS QD loaded in nanofibrous membranes to detect nitroaromatic explosive vapours. The sensing platform was synthesized by changing the ligands on the ZnS QD surface to detect and distinguish between four different explosives after 2 min of

exposure. QDs sensing processes are mainly based on photo-induced electron transfer (PET) or fluorescence resonance energy transfer (FRET) mechanisms between the QD and the analyte, causing a fluorescence quenching.[84,144]

The application of QDs sensor arrays for explosive sensing can enhance the sensitivity and also the selectivity of the sensors due to the combination of multiple outputs, which is possible because of the narrow size-tunability light emission of the QDs.[154,155,156] Peveler et al.[82] reported a sensor array based on CdSe QDs with different surface ligands to detect and discriminate five types of explosives in solution with a LOD lower than 0.2 ppm. The different interactions between the ligands and the analytes produce a fluorescent fingerprint for each analyte, providing both high sensitivity and selectivity. Bright et al.[157] developed a sensor array based on a nanocomposite of CdSe QDs and five organic polymers to identify some analytes in the vapour phase. The sensing platform was exposed to the vapours of two series, one of 14 different substituted benzene compounds and the other with 14 analytes related to security concerns. Linear discriminate analysis was used to distinguish the different analytes with more than 93% accuracy. Although most of the explosive sensors reported up to now show good sensitivity and selectivity, the identification and quantification of trace amounts of explosives in the vapour phase are still challenging.

In this part of the thesis, we report a cross-reactive heterogeneous sensing array consisting of two nanocomposites, which are formulated with CdSe QDs emitting at 560 nm (green QDs) and 597 nm (red QDs) embedded in polycaprolactone (PCL) as a host polymer matrix. The sensing system was evaluated for the fast detection and analyte discrimination capability when exposed to different explosive taggants and other nitro containing compounds in the vapour phase. The transduction mechanism of the sensor is based on changes in the PL intensity when molecules are adsorbed on the QD surface. We found that green and red QD nanocomposite sensor array shows a different response when exposed to different analytes. Therefore, it was possible to build up reliable fingerprints in a two-dimensional map, which enables the detection and identification of the analyte while maintaining low false alarm rates. Different cycles of 3-NT/bake determined the partial reversibility of the sensing process in both CdSe QDs. These facts confirm the weak interaction between the analyte and the surface of the QDs. The green CdSe-PCL nanocomposite shows a LOD of 54.8 pg, equivalent to 1.37 ppt or 10 pM.

3.2 Experimental

3.2.1 Reagents and materials

Polycaprolactone (PCL, average molecular weight: 80000, pellets), cadmium oxide powder (CdO), oleic acid (OA), selenium powder, trioctylphosphine (TOP), 2-mercaptoethanol (2-MET, 98%), ethylenediamine (EDA, 99%), 3-nitrotoluene (3-NT, 99%), picric acid (PA, 98%, moistened with water), 1-nitronaphtalene (1-NN, 98%), and 2,3-dimethyl-2,3-dinitrobutane (DMDNB, 98%) were purchased from Sigma-Aldrich. 1-Octadecene (ODE, 90%) was purchased from Merck. O-xylene, toluene, acetonitrile (ACN), acetone, hexane and methanol (MeOH) were purchased from Fisher Chemical. 4-Nitrotoluene (4-NT, 99%), 5-Nitroisoquinoline (5-NI, 98%), Nitromethane (NM, 99+%) and 4-Nitrophenol (4-NP, 99%) were purchased from ACROS Organics. The chemical structure of the analytes of interest is illustrated in Figure 24.

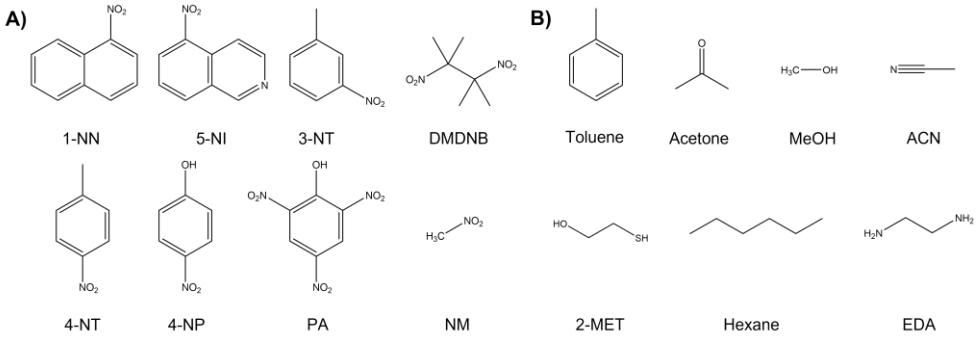

Figure 24. Chemical structure of the analytes of interest. A) Explosive taggants and analogues. B) Volatile organic compounds (VOCs).

3.2.2 Synthesis and Purification of CdSe QDs

CdSe QDs were synthesized by a conventional synthesis route based on a hot injection method with some modifications.[158] In brief, a mixture of CdO (9 mmol), oleic acid (54 mmol), and ODE was loaded in a 100 mL three-neck flask and heated under vacuum at 120ºC for 30 minutes. Consequently, this mixture was heated up to 230ºC for the complete dissolution of precursors under an N_2 atmosphere. After that, a mixture of Se (6 mmol) and TOP (29.8 mmol) was heated to obtain a transparent solution, and then it was swiftly injected into the CdO solution. To obtain the green-emitting CdSe QDs, the

reaction system was cooled, and after 30 seconds, 10 mL of ODE was injected. The procedure to obtain the red-emitting QDs are similar, but after the injection, the mixture reacted for 5 min for the growth of the QDs. Both CdSe QDs were purified by several successive precipitations and redispersion steps with a mixture of acetone and methanol and redispersed in o-xylene with a final concentration of 20 mg/mL.

3.2.3 CdSe-PCL nanocomposite preparation and device fabrication

Solutions of CdSe QDs and PCL was prepared in o-xylene. The solution was mixed under stirring for 15 min to obtain a homogeneous dispersion. The final CdSe-PCL solutions consists of 8.0 wt. % PCL and 0.4612 mg/mL green-emitting CdSe QDs or 0.1678 mg/mL for and red-emitting CdSe QDs. The sensor was fabricated by spin-coating the CdSe-PCL solutions on a 0.5 cm^2 glass slide substrate at 2000 rpm for 30 seconds. Afterwards, the sensors were baked at 100ºC for 10 min to remove the solvent and achieve good adhesion of the nanocomposite to the substrate and enhance the chemical stability of the layer. Both sensors were glued on a 2x2 cm glass slide substrate to obtain a multichannel array. Sensors with green and red QDs have been chosen to avoid the overlapping of their PL spectra, which allows to measure the response of both sensors simultaneously. The film thickness of the resulting sensors was measured to be around 750 nm using a mechanical profilometer (Veeco Dektack 150).

3.2.4 Characterization techniques

Optical absorbance spectra of the colloidal solution containing CdSe QDs in o-xylene and the CdSe QDs embedded in the PCL host matrix were measured at room temperature using a UV-Visible spectrophotometer (Perkin-Elmer lambda 20 UV-VIS spectrophotometer). The photoluminescence spectra of the nanocomposite thin films containing CdSe QDs are obtained upon the sensors' excitation with a CW GaN laser (404 nm) for green- and red-emitting nanocomposites. The PL quantum yield was determined to be 30 % for both green and red CdSe QDs using an integrated sphere (Hamamatsu model C9920-0). Transmission electron microscopy (TEM) were carried out at an accelerating voltage of 100 kV using a JEOL 1010 microscope.

3.2.5 Sensing protocol

The sensing capability of the CdSe-PCL sensors was tested by exposing the nanocomposites to the vapours of 0.2 g of the different nitro-compounds and common solvents in a closed 100 mL vessel at room temperature for different times (Figure 25A). The calibration curve was obtained by exposing the green CdSe sensor to the vapours of 40 mL aqueous solution using different concentrations of the analyte. The PL sensitivity and response time of the nanocomposites were measured by a homemade setup (Figure 25B) based on a CW GaN laser (404 nm) focused onto the sensor using a lens and positioning system to obtain precise and reproducible results and a commercial spectrophotometric system NanoSPR103 (NANOSPR). The sensing and detection conditions were performed in the dark to obtain good PL measurements. Moreover, all experiments were performed three times to evaluate the stability of the sensors and the reproducibility of the data, obtaining good results.

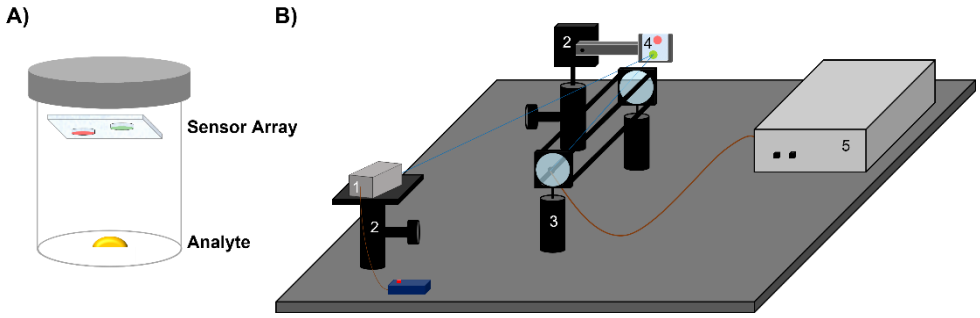

Figure 25. Schematic picture of A) the sensing system and B) the homemade experimental setup. The different elements of the setup are: 1) laser source; 2) positioning system; 3) lens system; 4) sensor array; 5) detector.

3.3 Results and discussion

3.3.1 Synthesis and characterization of CdSe-PCL sensor

The synthesis of the CdSe-PCL sensors is straightforward and consists of a single step, as is illustrated in Figure 26. Firstly, a solution of PCL and green or red CdSe QDs in o-xylene are and spin-coated on a glass substrate and baked at 100ºC to remove the solvent. The sensor array consisted of two different nanocomposite films formulated with green and red CdSe QDs embedded in PCL. This system was designed to detect and

discriminate a range of explosives and explosives-like molecules. PCL is a biodegradable, hydrophobic, and inexpensive polymer with a low melting point (59 – 64ºC) and glass transition temperature (-60ºC) and is considered an excellent host matrix for CdSe QDs because it shows exceptional film-forming properties and outstanding blend compatibility with oleate-capped CdSe QDs.[79,159,160]

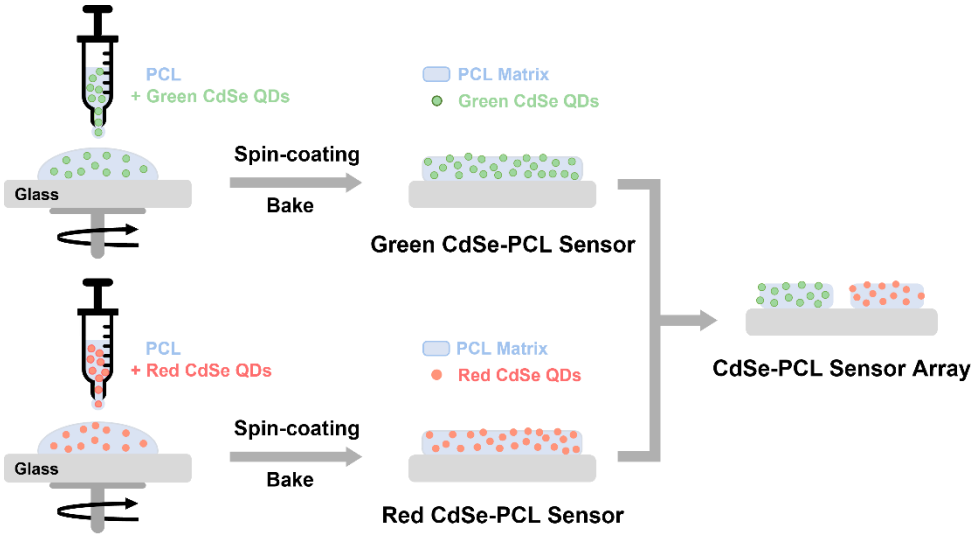

Figure 26. Schematic approach to synthesize the CdSe-PCL sensor array.

Figure 27A shows the absorbance and PL spectra of the green and red CdSe QD-PCL thin film. The first energy exciton state of the CdSe-PCL nanocomposites was observed at 515 nm for green-emitting QDs and 558 nm for red-emitting QDs. The emission peak of the green and red CdSe QDs embedded into the PCL was located at 543 nm (FWHM of 40 nm) and 588 nm (FWHM of 49 nm), respectively. The absorbance and PL of the nanocomposite thin films shows a blue shift with respect to the green and red CdSe QD solution in o-xylene (Figure 27B and 27C). Mainly PL shows a significant blue shift from 560 and 596 nm to 543 and 588 nm when the green and red QDs are embedded into the polymer. Figure 27D and 27E shows TEM images of the green and red CdSe QDs and their corresponding size distribution. We calculated an average size of 2.2 ± 0.5 nm for green CdSe-PCL and 3.6 ± 0.7 nm for red CdSe-PCL. The average size of colloidal green and red CdSe QDs was 2.4 ± 0.3 nm and 3.6 ± 0.8 nm, respectively (Figure 27F and 27G). These results confirm that the size distribution of the green and red CdSe QDs remain constant after the formation of the nanocomposite. The PL blue shift after the formation of the nanocomposite may mainly be attributed to a decrease of the effective

refractive index surrounding the QDs caused by the porosity of the polymer matrix. SEM images of both nanocomposites reveal a homogeneous, flat, and smooth surface (Figure 27H and 27I).

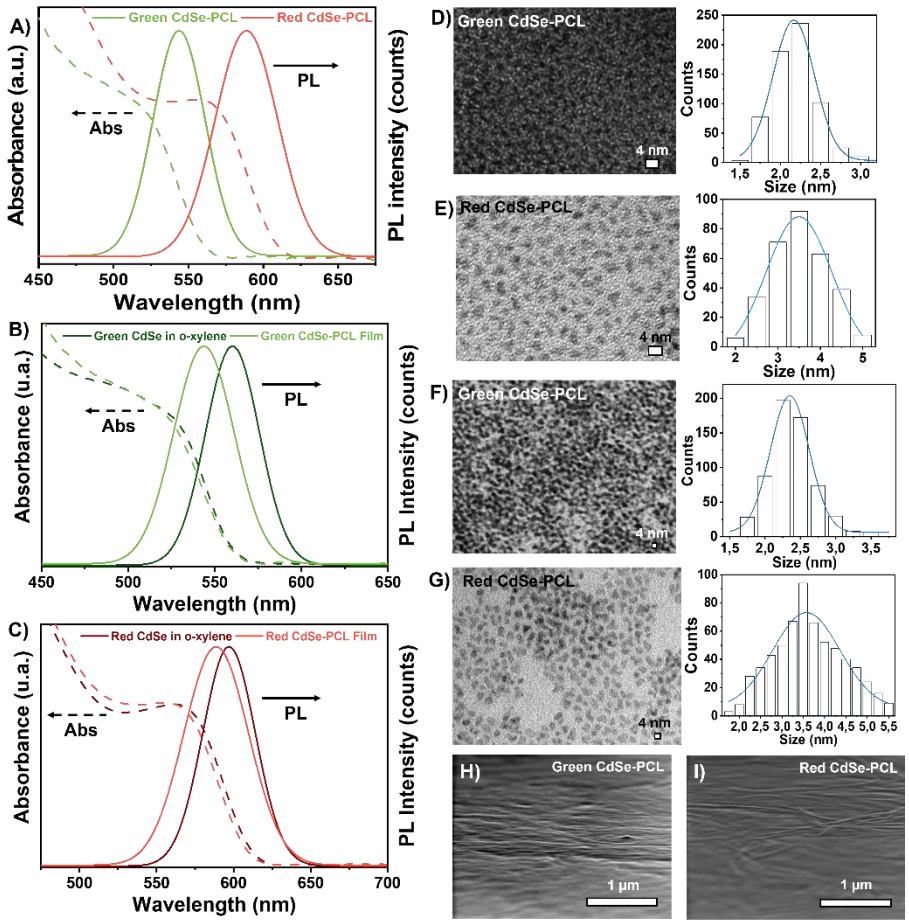

Figure 27. A) UV-Visible absorption and emission spectra of both green and red CdSe QD-PCL thin films. UV-vis absorption and emission spectra of B) green CdSe QDs in o-xylene (dark green line) and embedded in PCL (light green line) and C) red CdSe QDs in o-xylene (dark red line) and embedded in PCL (light red line). TEM image and size distribution of D) green CdSe QD-PCL, E) red CdSe QD-PCL, F) colloidal green CdSe QDs, and G) colloidal red CdSe QDs. SEM images of H) green-CdSe-PCL film and I) red-CdSe-PCL film.

3.3.2 Analyte Sensing

The evaluation of the sensing capability of the nanocomposites was performed by exposing the sensor array to 3-NT vapours in a 100 mL closed vessel at room temperature. The concentration of the 3-NT in the vapour phase depends on the vapour pressure of the analyte because the mass transport is caused by a diffusion process. Figure 28 exhibits the PL response of the green CdSe-PCL (Figure 28A) and red CdSe-PCL (Figure 28B) nanocomposites upon exposure to vapours of 3-NT for different times. The measurements were done, providing enough time to interact the analyte with the sensor. The exposure of the sensor array to 3-NT led to a significant PL enhancement. Remarkably, the change in the PL intensity is quite different depending on the nanocomposite. As can be observed, the exposure of the sensor array to 3-NT led to a significant PL enhancement within the first 30 seconds in both nanocomposites (138.2 % green CdSe-PCL and 165.6 % red CdSe-PCL). Wu et al.[153] reported a time response of 2 min for ZnS QDs for nitroaromatic compounds, whereas Bright et al.[157] reported 60 s for CdSe QDs nanocomposite array.

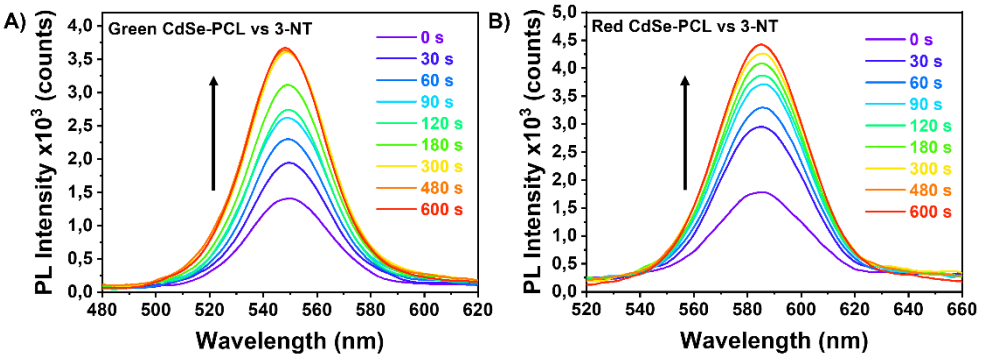

Figure 28. Fluorescent spectral changes of the CdSe-PCL sensor array containing A) green CdSe QDs and B) red CdSe QDs upon exposure to 3-NT.

The time-dependent PL changes of the sensor array containing green and red QDs to 3-NT vapours is plotted as a function of exposure time using PL intensity as a response variable (Figure 29A). The experimental data obtained for the 3-NT exposure can be fitted by the following pseudo-first order kinetic equation proposed by Lagergren, which describes the diffusion of the analytes:[67,161,162] $PL_t = PL_\infty + A \cdot e^{-k \cdot t}$, where PL_t is the PL intensity at a given time, PL_∞ is the response when the sensor is saturated by the analyte,

and k is the binding rate constant. The results obtained from fitting the real-time PL response are listed in Table 4.

Table 4. Maximum PL intensity and kinetic binding constant for CdSe-PCL sensor array exposed to 3-NT vapours.

	PL_∞ (%)	k (ms^{-1})
Green CdSe-PCL	260 ± 3	8.35 ± 0.11
Red CdSe-PCL	249 ± 4	13.61 ± 0.13

As can be observed, the interaction between the analyte molecules and the CdSe QDs embedded in the PCL matrix depends on the time exposure, which is determined by the diffusion of the analyte and the subsequent chemical interaction rate.[66,67] The kinetic constant depends on the amount of available CdSe QDs (binding sites) embedded in the polymer matrix and also on the mass concentration of analyte in the vapour phase, which is directly related to the vapour pressure of the analyte. For that reason, the maximum binding rate is achieved at the beginning of the sensing process, when almost all of the binding sites are unoccupied. As a result, the limiting step changes during the sensing process. While the mass transport from the vapour phase to the QDs surface principally controlled the first stages of the sensing test, the interaction between the analyte and CdSe QDs limited the later steps. Red CdSe QD-PCL show a faster analyte binding kinetics (k = 13.61 ms^{-1}) than green QD-PCL (k = 8.35 ms^{-1}). The differences are more significant at low sensing times. After 30 s green and red CdSe QD-PCL exhibits a PL enhancement of 138.2% and 165.6% respectively. However, after 180 s of exposure to 3-NT vapours, both sensors show more than 220% PL enhancement. Both sensors shows similar PL_∞.

The mechanism of the PL enhancement is not fully understood, but some mechanism are stated in the literature. The increase of fluorescence can be explained in a hybrid steric/electronic mechanism. The change in the PL intensity might be based on the disruption of the steady-state complex formed by the CdSe QD and PCL in the nanocomposite. The polymer matrix probably created trap states on the QD surface that affected the QD fluorescence properties. When the vapour analytes diffuse within the matrix, and they can cause the polymer swelling. As a result, the steady-state complex can be interrupted by the detachment of the polymer chains from the CdSe QD surface, leading to a change in the fluorescence properties.[157,163] Therefore, the observed PL enhancement can mainly ascribed to the swelling induced in the polymer when exposed

to the volatile organic compound analytes. Moreover, once the PCL chains separate from the QD surface, the analyte can interact directly with the QDs' surface. Analytes can act as pseudoligands to passivate trap states with different effectiveness depending on their composition. This affect the PL properties of QDs accordingly, as shown by other ligand exchange studies.[136,140] Interestingly, PL enhancement when exposed to 3-NT is generally faster in red CdSe-PCL than in green CdSe PCL. Swelling rate of the CdSe-PCL is probably dependent on the QD size. The size of the QDs can be affected the swelling because of the spacing between the polymer chains increases with the size of the QDs. Because the green QDs are smaller (2.2 nm) than red QDs (3.6 nm), the steady-state complex between the polymer matrix and green QD is stronger because more intermolecular bonds are formed. It is well accepted that properties of nanocomposite are strongly affected by the nanoparticle size. Several works report that the nanoparticle size clearly affect various material mechanical properties such as the Young's modulus,[164] the thermal expansion coefficient the thermal conductivity, and the electrical conductivity. Therefore, one could expect that as the QD size decreases, the steady-state complex between CdSe QD and PCL is stronger.

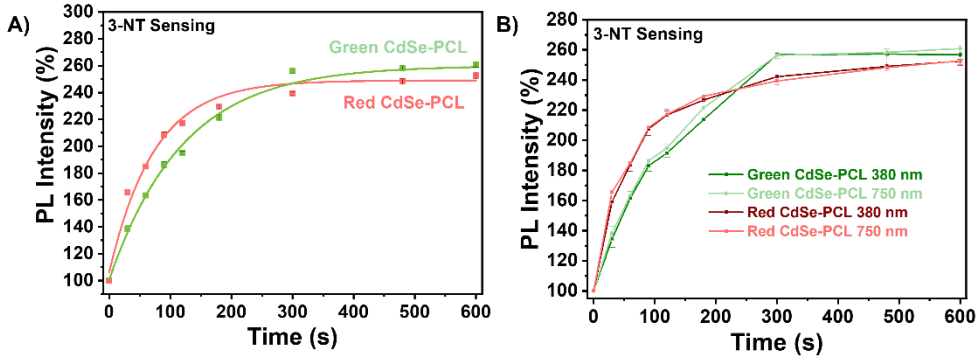

Figure 29. A) Real time response of the two-segmented sensor upon the exposure to a 3-NT vapours. B) Real-time response of the different thickness sensing platforms upon exposure to 3-NT vapours.

We also evaluate the influence of the film thickness on the sensing response. As can be observe in the Figure 29B, the 380 nm and 750 nm- thick sensors show comparable response to 3-NT. These results suggests that the polymer matrix allows a complete diffusion of the nitro-containing analytes in the film at these two-film thickness.

Figure 30A shows the sensor reversibility. Every sensing cycle involves an exposure to 3-NT flow for 240 s followed by a recovering cycle by a baking at 100ºC for 240 s. The

PL intensity increases when the nanocomposites is exposed to 3-NT vapours. After the baking step, the green CdSe-PCL sensors recover around 75 % of the initial PL but red CdSe-PCL sensor improve the initial PL around 110 %. Because most of the 3-NT molecules are weakly adsorbed on the surface of the sensors, and they can be easily desorbed after a mild thermal annealing. However, both sensors show a certain hysteresis after every sensing/recovering cycle but with different behaviour. Whereas the green CdSe-PCL sensor exhibit a gradual PL loss after every sensing/recovering cycle, the red CdSe-PCL sensor shows a constant PL increase. In the case of green CdSe-PCL, the loss of PL is attributed to the degradation of the CdSe QD after the baking. In fact, every sensing/recovering cycle the ratio of PL before and after sensing decays. This is expected because small QDs are thermodynamically more unstable. On the other hand, the increase of PL in the red CdSe-PCL sensor is ascribed for a non-complete removal of analyte after the baking. Every sensing/recovering cycle a greater number of analyte molecules are attached to the QD surface and PL increases. In fact, the red CdSe-PCL sensor shows a constant ratio of PL before and after sensing. This confirms that the red CdSe-PCL sensor is reversible unlike the green CdSe-PCL sensor.

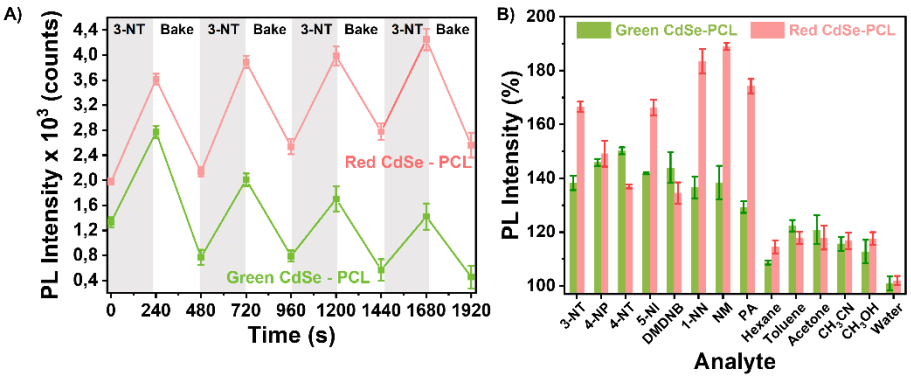

Figure 30. A) Real-time response of green and red CdSe-PCL sensors to periodic cycles of 3-NT vapours (grey area) and mild thermal annealing at 100ºC (white area). B) Selectivity of CdSe-PCL sensor array to different NO_2-containing compounds and some common solvents after 30 s of exposure.

Figure 30B shows the PL of the CdSe-PCL sensor array after 30 s of exposure to vapours of some explosive taggants (3-NT, 4-NT, DMDNB), other NO_2-containing compounds (4-NP, 5-NI, 1-NN, NM, PA) and some solvents (hexane, toluene, acetone, acetonitrile (CH_3CN), methanol (CH_3OH), and water). The response of both sensors toward the explosive taggants and nitro-containing molecules were higher than toward the common

solvents (Figure 31A for green CdSe-PCL sensor and Figure 31B for red CdSe-PCL sensor). These results indicate that the sensor array interacts more selectively with nitro-containing molecules. Because the sensor array is label-free, it does not provide a highly specific sensing, but a certain selective sensing. The interaction between the analytes and the QD surface depends on the chemical structure of analytes. In addition, the PCL matrix provide certain degree of selectivity because it does not allow the diffusion of all analytes in the same way. This means that PCL shows specific permeability to nitro compounds, as already observed in our previous work.[165] More interesting, both sensors shows different response to nitro-containing analytes. Specifically, red CdSe-PCL sensor exhibited an extraordinary response to NM (188.0 % PL), 1-NN (182.5 % PL) and PA (173.2 % PL), whereas green CdSe-PCL sensor showed high affinity to 4-NT (150.2 % PL) and DMDNB (144.0 % PL). This is an extraordinary tool to fingerprint analytes.

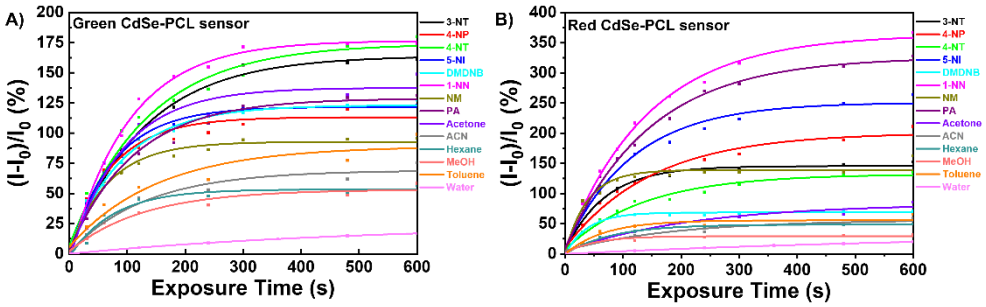

Figure 31. Selectivity of the sensor array. Time-dependent fluorescence intensity of A) green CdSe-PCL sensor and B) red CdSe-PCL sensor to vapours of different nitro-containing compounds and some common solvents.

When the sensor array is exposed to well-known ligand molecules like thiols (2-mercaptoethanol (2-MET)) or diamines (ethylenediamine (EDA)) (Figure 32A and 32B), a very fast chemical interaction between 2-MET and EDA and the CdSe QD surface is observed due to their strong affinity to the transition metals like Cd(II).[67] As a result, the red and green CdSe-PCL PL decays abruptly and irreversibly.

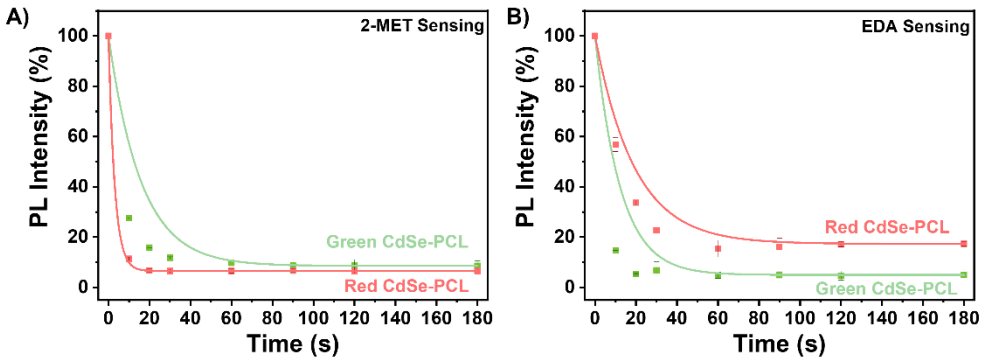

Figure 32. Real time response of the two-segmented sensor upon the exposure to A) 2-MET vapours and B) EDA vapours.

On the basis of the different responses of the green and red CdSe-PCL sensor to the analytes, the sensor array was examined for their ability to fingerprint analytes by multiparameter analysis. Monitoring the changes in the PL of the green and red CdSe-PCL sensor array allowed to pinpoint each analyte on a two-dimensional (2D) map. To generate such response patterns, the PL response of green and red CdSe-PCL nanocomposites were plotted after 30 s exposure to analytes in Figure 33A. By using these two parameters, we can classify the analytes in three different groups. The first group consists of the common solvents with the lowest response (low affinity for both nanocomposites). The second group is formed by those analytes with the greatest interaction with green CdSe-PCL sensor (DMDNB, 4-NT and 4-NP). The third group is composed of the analytes which showed the highest response with red CdSe-PCL sensor (NM, 1-NN, PA, 3-NT and 5-NI). These results demonstrate that we can discriminate between the explosive taggants 3-NT, 4-NT and DMDNB. Moreover, the sensor array shows specific molecular recognition towards PA, an explosive of great importance. Wu et al.[153] and Peveler et al.,[82] describe a sensing platform in which can distinguish between 4 and 5 explosive compounds, respectively.

Figure 33B represents the green CdSe-PCL sensor response to vapours of different concentrations of 3-NT, 4-NT, DMDNB and PA in water for a constant exposure time of 20 min. We focused on PA (explosive compound) and 3-NT, 4-NT and DMDNB (explosive taggants). From the calibration curves, we can determine the limit of detection (LOD) to quantify the minimum analyte amount that the sensor would be able to detect.

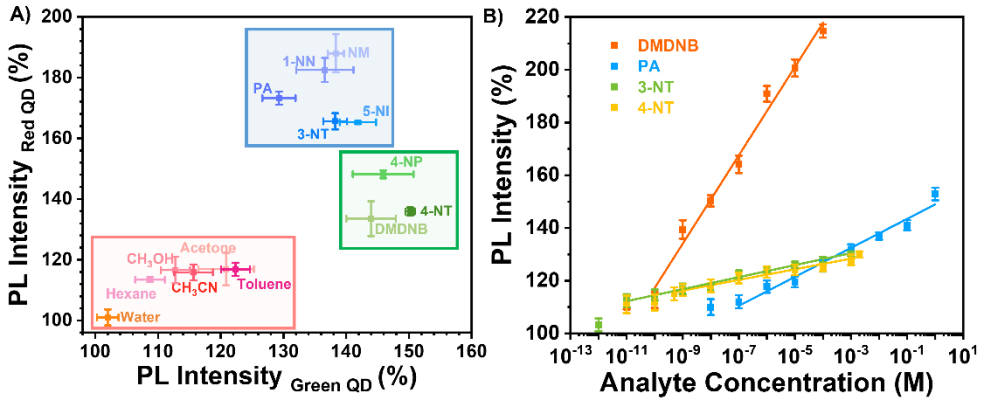

Figure 33. A) Two-dimensional (2D) map of the PL efficiency of both nanocomposites after 30 s of exposure. B) Calibration curve of the green CdSe-PCL sensor. PL enhancement as a function of 3-NT, 4-NT, DMDNB and PA concentration after 20 min of exposure.

We can also calculate the sensor sensitivity, which is defined as the sensor response per logarithmic unit of analyte concentration. The response of the green CdSe-PCL nanocomposite to water vapours shows only a PL increase of 10 % after 20 min (Figure 34), which is consider the blank from which the detection is feasible. The assumption is that if analyte is present, the sensor will produce a response greater than the analytical noise in the absence of analyte. The experimental LOD, sensor sensitivity and linear range are listed in Table 5.

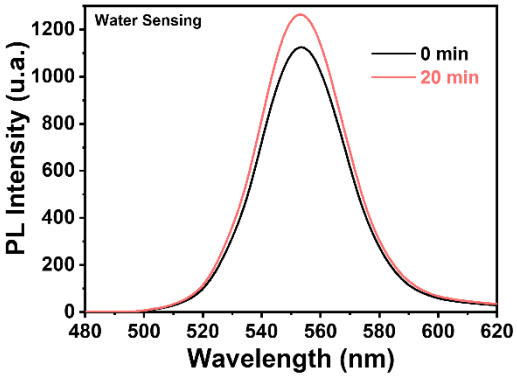

Figure 34. Green CdSe-PCL nanocomposite response to water vapours after 20 min of exposure.

Table 5. LOD, sensitivity and linear range for green CdSe-PCL sensor exposed to different analyte vapours.

Analyte	LOD (ppb)	Sensitivity (% PL)	Linear Range (M)
3-NT	0.0014	2.28 ± 0.11	$10^{-11} – 10^{-3}$
4-NT	0.068	2.01 ± 0.12	$5 \cdot 10^{-10} – 10^{-3}$
DMDNB	0.088	16.76 ± 0.91	$10^{-10} – 10^{-4}$
PA	22.9	5.50 ± 0.37	$10^{-7} – 1$

The sensor shows the lowest LOD for 3-NT, which was determined to be 0.055 ng, this is 1.37 ppt or 10 pM. Generally, the green CdSe-PCL sensor shows an excellent linear response within a wide range of concentrations. For example, the sensor response to 3-NT shows a linear behaviour from 10^{-11} to 10^{-3} M, this is, 8 orders of magnitude. A wide-range linear response is desirable to develop a quantitative sensor. The sensor sensitivity is another important parameter, which can be determined from the slope of the linear regression of the calibration curve. The sensor has the highest sensitivity for DMDND, this is 16.76 % PL per logarithmic unit of analyte concentration. The sensitivity reported by Wu et al.[153] and Peveler et al.[82] is 4 ppb and lower than 0.2 ppm, respectively.

3.4 Conclusions

The majority of the current detection methodologies focus on the fluorescent intensity change (quenching/enhancing) of a single transducer, which may be efficient in identifying analytes from different categories but will be unable to distinguish analytes having similar properties. To overcome this limitation, we reported a sensor array based on green or red-emitting CdSe QDs embedded in PCL as a host matrix allowing the identification and quantification of trace amounts of explosive taggants and explosive-like molecules. The experimental LOD of the green CdSe-PCL for 3-NT, 4-NT, DMDNB and PA was found to be 0.055 ng, 2.7 ng, 0.7 ng and 916.4 ng respectively. This sensor response was very fast and showed a very wide linear response to explosive taggants (up to 8 orders of magnitude), which forms the basis to be used as a quantitative sensor. Combining two transducers constitutes a powerful tool to discriminate between some of the most commonly used explosive taggant 3-NT, 4-NT and DMDNB. Moreover, the sensor array shows specific molecular recognition towards PA, an explosive of great importance. Multiparametric analysis allow us to improve sensitivity and selectivity significantly and to minimize false-positive responses. This type of miniaturized

luminescent QD-based nanocomposites might form the basis of a sensing platform technology to perform effective chemical detection and identification of explosive taggants for preblast and postblast.

Chapter 4

Molecularly imprinted nanocomposites of $CsPbBr_3$ nanocrystals

Chemical sensors based on metal halide perovskites have recently attracted tremendous interest because of their excellent photophysical properties. In this work, we report the synthesis of a solid-state luminescent gas sensor based on a nanocomposite of $CsPbBr_3$ nanocrystals (NCs) embedded in a molecularly imprinted polymer (MIP) using 3-nitrotoluene (3-NT) and nitromethane (NM) as template molecules. The MIP sensor fabrication is straightforward and low-cost: the molecular imprinting process occurs inside the nanocomposite of $CsPbBr_3$ NCs in polycaprolactone (PCL) during the baking step after spin-coating. The sensing capability of the MIP sensors was evaluated and compared to that of the non-imprinted polymer (NIP) by monitoring photoluminescence (PL) upon exposure to vapours of different explosive taggants, nitro-containing molecules and some organic solvents. The nanocomposite sensors show a fast response time to analytes below 5 s. The molecular imprinting enhances the PL response of MIP sensors and a robust specificity to 3-NT, and an excellent selectivity towards nitro-containing molecules, particularly when NM is used as the template molecule. Chromatography confirms that molecular imprinting of $CsPbBr_3$-PCL with NM provides two times more selective binding sites than 3-NT and four times more sites than non-imprinted polymer sensors. Surface topography also suggests that the molecular imprinting in NM MIP is higher than in 3-NT MIP. These facts confirm that molecular imprinting successfully generates specific recognition sites, allowing fast detection of 3-NT below 3 s with a limit of detection as low as 0.218 µg/mL. Experimental results, discussions and conclusions of this chapter are entirely based on the article *"Molecularly imprinted nanocomposites of CsPbBr3 nanocrystals: an approach towards fast and selective gas sensing of explosive taggants"*.

4.1 Introduction

In recent years, metal halide perovskites (PVKs) have attracted tremendous interest because of their excellent optoelectronic properties such as large absorption co-efficient, long carrier lifetime, and large diffusion coefficient.[166] Owing to their excellent properties and the possibility of processing them into thin films from solution, these materials are ideal candidates for use in applications such as lighting devices, photodetectors, photocatalysts and flexible solar cells.[167] PVKs show an ionic-rich labile surface, but this apparent drawback could be helpful for sensing.[168] Therefore, metal halide PVKs have been proposed to sense ozone,[169] oxygen,[170,171] humidity,[172,173] metal ions,[174] ammonia,[175] nitro-compounds,[176] etc. PVKs show outstanding results as active materials in sensors with high selectivity and sensitivity. In general, the photo-induced electron transfer between the PVK and the analyte ultimately will cause variations in the PL features (intensity, mainly). Compared with bulk PVKs, nanocrystals (NCs) of metal halide PVK are more interesting for sensing applications because they show superior optical properties, like very narrow photoluminescence (PL) and near-unity PL quantum yield (PLQY) due to the high tolerance to defects.[177] The transduction mechanism of PVK NCs-based sensor is generally based on the quenching of the PL when the analyte reaches the PVK NC surface. The exact sensing mechanism behind PL quenching is still controversial: some authors propose a charge transfer mechanism between the PVK NCs and the analyte, and other authors propose trap-state generation in PVK NCs.[178,179]

In the past years, conventional chalcogenide nanocrystalline semiconductors and their composite structures, graphene and several organic compounds were employed to sense explosives.[180,181,182] Similar to the traditional semiconductor nanomaterials, the explosive sensing capability of PVK nanostructures can be of potential interest, and the necessary efforts can be undertaken to find the possible ways to explore them for such applications. Because of the electron-withdrawing ability of the nitro group, the photo-induced charge transfer mechanism between PVK NCs and nitro explosives is speculated to help for the sensing characteristics.[178,183] The electrostatic-assisted electron transfer was proposed as the origin of the measured PL quenching. Most of the research in the state-of-the-art literature is based on detecting explosives in solution because of their low vapour pressure, as previously mentioned. However, to develop optical sensors directly on-field, their primary purpose will be to detect explosives and explosive-like molecules in the vapour phase.[83]

One of the main drawbacks of NCs thin films is the poor long-term stability of their PL, which makes it essential to stabilize the PVK NCs in ambient environments to improve reproducibility and repeatability to achieve reliable sensing results and avoid false positives. These are prerequisites for the integration for commercial purposes. An approach to enhance the stability of PL properties against moisture, heat and light is to embed PVK NCs into a polymer matrix to form a nanocomposite.[179] However, these sensors suffer from low selectivity and sensitivity. A promising way to improve the sensitivity and selectivity of sensors is to use molecularly imprinted technology (MIT) to create specific molecular recognition sites in a polymer.[184]

Most of the explosive sensors reported up to now show good sensitivity and selectivity, mostly in solution. However, the development of explosive gas sensors is still necessary for the accurate detection of explosives and is still challenging.

In this chapter, we report a gas explosive MIP sensor based on $CsPbBr_3$ NCs embedded in a polycaprolactone (PCL) matrix, using 3-nitrotoluene (3-NT) or nitromethane (NM) as template molecules. The MIP sensor fabrication is very fast and low-cost. A precursor solution of OAm/OA capped $CsPbBr_3$ NCs, PCL, and template molecules is spin-coated onto a substrate to generate a thin film and baked. The template is removed in the drying process. Selective binding sites are generated in the solid-state sensor. The resulting nanocomposite combines the sensitivity of the $CsPbBr_3$ NCs with the selectivity of the MIPs, showing a speedy sensing response upon exposure to analytes in the gas phase. We have demonstrated the vapour sensing capabilities of the $CsPbBr_3$-PCL MIP sensor to some explosive taggants and other nitro containing compounds. Different cycles of 3-NT/air determined the partial reversibility of the sensing process in MIP sensors. FTIR and gas chromatography confirm the template removal in the MIP sensor after the baking and also that molecular imprinting with NM provides two times more selective binding sites than 3-NT and four times more than the reference sensor without MIT. Surface topography also suggests that the molecular imprinting in the NM MIP is higher than in the 3-NT MIP. These facts confirm that the specific recognition sites have been successfully generated, allowing the detection of 3-NT in vapour phase under concentrations of around 0.218 µg/mL and a response time of a few seconds.

4.2 Experimental

4.2.1 Reagents and materials

PCL (average molecular weight: 80000, pellets), cesium carbonate (99%), oleic acid (OA, 90%), 1-NN (98%), DMDNB (98%), 3-NT (99%) and chlorobenzene (ClBz) were purchased from Sigma-Aldrich. Lead (II) Bromide (98+%), o-xylene, ethyl acetate (EtOAc), toluene, acetonitrile (ACN), chloroform, acetone, and methanol (MeOH) were purchased from Fisher Chemical. 4-NT (99%), 5-NI (98%), NM (99+%), 4-NP (99%) and oleylamine (OAm, 80-90%) were purchased from ACROS Organics. 1-Octadecene (ODE, 90%) was purchased from Merck. The chemical structure of the analytes of interest is illustrated in Figure 35.

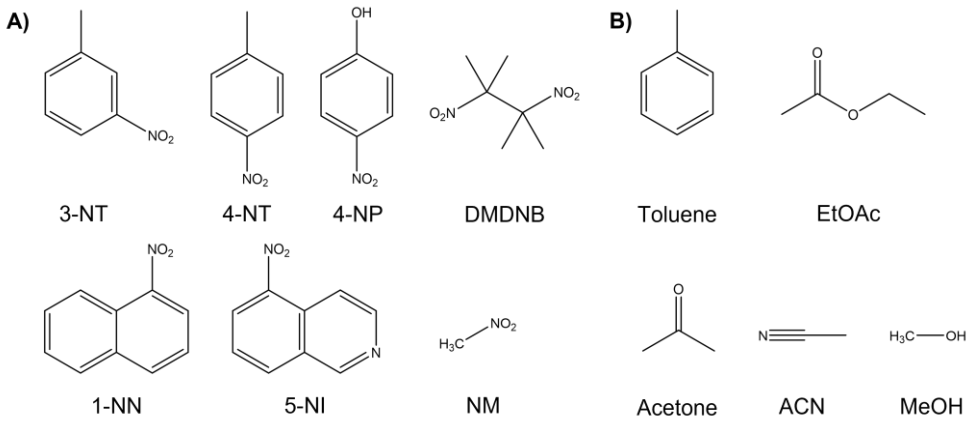

Figure 35. Chemical structure of the analytes of interest. A) Explosive taggants and analogues. B) Volatile organic compounds (VOCs).

4.2.2 Synthesis and Purification of $CsPbBr_3$ Nanocrystals

The $CsPbBr_3$ NCs were synthesized via the hot-injection method with some modifications.[185] On the one hand, 0.16 g Cs_2CO_3, 10 mL 1-ODE and 5 mL OA is mixed into a 50 mL three-neck flask and heated under vacuum for 1 h at 120 ºC, and the temperature is then increased to 150 ºC under N_2 atmosphere to form a Cs-oleate precursor. On the other hand, a mixture of 0.55 g $PbBr_2$ and 20 mL ODE is loaded into a 100 mL three-neck flask and dried under vacuum at 120 ºC for 1 h. After that, 5 mL OAm and 5 mL OA is added under N_2 atmosphere, and the solution is heated to 160 ºC for 1

h. Then, the solution is heated to 195 ºC, and the Cs-oleate solution is swiftly injected and 1 min later, the reaction system is cooled in an ice-water bath. The $CsPbBr_3$ NCs are purified by several successive centrifuging and redispersion steps with a mixture of n-hexane and EtOAc. The purification is an essential step to reach the isolation of the $CsPbBr_3$ NCs for further embedding into a polymer to form thin films by spin-coating. Finally, the $CsPbBr_3$ NCs are redispersed in o-xylene with a concentration of 32 mg/mL.

4.2.3 $CsPbBr_3$-PCL nanocomposite preparation and sensor fabrication

$CsPbBr_3$-PCL solution was prepared dispersing $CsPbBr_3$ NCs (28.5 mg) and PCL (200 mg, 4 wt. %) in o-xylene (5 mL). The resulting solution was mixed with 3-NT or NM in a ratio 4:1. The final composition achieved for PVK-PCL MIP solutions was: PCL (24 mg/mL, 2.40 wt. %), $CsPbBr_3$ NCs (3.58 mg/mL), and 3-NT (229.02 mg/mL, 1.67 M) or NM (219.74 mg/mL, 3.6 M) for 3-NT and NM MIP. NIP solution was prepared without template keeping the same concentrations of PCL and $CsPbBr_3$.

The MIP- and NIP-based sensors are deposited by spin-coating a precursor solution onto a 0.5 cm^2 glass slide substrate at 2000 rpm for 30 seconds and baked at 100 ºC for 10 min to remove the solvent and the template. The fabrication of MIP nanocomposites are illustrated in Figure 36. The film thickness of the sensors is measured to be around 180 nm on a mechanical profilometer (Veeco Dektak 150).

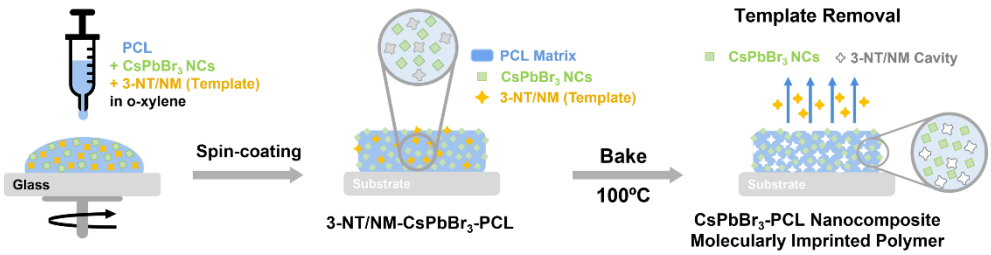

Figure 36. Schematic steps of the fabrication of the $CsPbBr_3$-PCL 3-NT or NM MIP sensor.

4.2.4 Characterization techniques

The absorbance spectra of the colloidal solution containing $CsPbBr_3$ NCs in o-xylene and the nanocomposite films containing $CsPbBr_3$ NCs are measured at room temperature using a UV-Visible spectrophotometer (V-770 UV-Visible/NIR Spectrophotometer,

Jasco). The photoluminescence spectra of $CsPbBr_3$ NCs embedded in the PCL host matrix are obtained upon the excitation of the sensors with a CW GaN laser (404 nm) for NIP and MIP nanocomposites. The $CsPbBr_3$ NCs PLQY was determined to be 70 % using an integrated sphere (Hamamatsu model C9920-0). The functional groups of the sensor were identified on a FT-IR spectrometer (ATR-FTIR Thermo Nicolet Nexus).

Quantification of 3-NT was carried out by gas chromatography (GC) using a chromatograph (Agilent 6890+ series) coupled to a flame ionization detector (FID), equipped with a cross-linked 5% phenyl-methylsiloxane column (30 m×0.32 mm×0.25 µm film thickness). This technique provides information about the number of molecular recognition sites depending on the amount of 3-NT detected. Figure 37 shows the calibration line obtained from blends prepared by mixing 3-NT solutions (0.05, 0.1, 0.5, 1, and 5 mM in chloroform) and chlorobenzene as the internal standard (10^{-4} M). The calibration line presented a good correlation (R=0.999) between the analyte concentration and the detector response. Twenty films of NIP, 3-NT MIP, and NM MIP were prepared by spin-coating and baked at 100 ºC. These films, which have internal average concentrations in the range of the calibration blends, were dissolved in chloroform and analysed by GC.

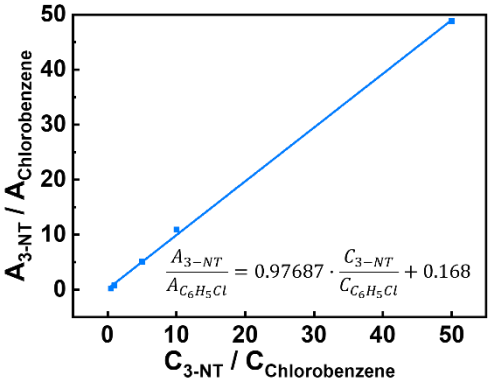

Figure 37. Gas chromatography calibration curve of 3-NT using an internal standard.

The $CsPbBr_3$-PCL films were also characterized by XRD (XPERT Pro, Panalytical). The surface morphology of the films was studied by scanning electron microscopy (SEM, Hitachi S4800). To obtain the size and shape of the $CsPbBr_3$ NCs embedded in the polymer, transmission electron microscopy (TEM) were carried out at an accelerating voltage of 100 kV using a JEOL 1010 microscope. TEM samples were prepared by

ultrasonication in o-xylene of small pieces of $CsPbBr_3$ NCs nanocomposite coated on coverslips with the sensor. This procedure led to a suspension of micrometre-sized fragments of nanocomposites that was dropped on a carbon-coated Cu grid. The microstructural information and chemical composition of the $CsPbBr_3$-PCL sensors were obtained by HR-TEM (Tecnai G2 F20 S-TWIN from FEI Company).

4.2.5 Sensing protocol

The sensing capability of the $CsPbBr_3$-PCL films was measured by a homemade setup (Figure 38) based on a CW GaN laser (404 nm) focused onto the sensor using a lens and positioning system to measure the fluorescence spectra in the same position to achieve accurate and reproducible PL intensity values. $CsPbBr_3$-PCL sensors are introduced into a cuvette of 4.5 cm^3 and are exposed to vapours of different organic volatile compounds. This process was carried out using air as a gas carrier at room temperature at different times pumped using a peristaltic pump at a constant flow of 0.57 µL/min. The PL sensitivity and response time of the various sensors were obtained by means of the commercial spectrophotometric system NanoSPR103 (NANOSPR).

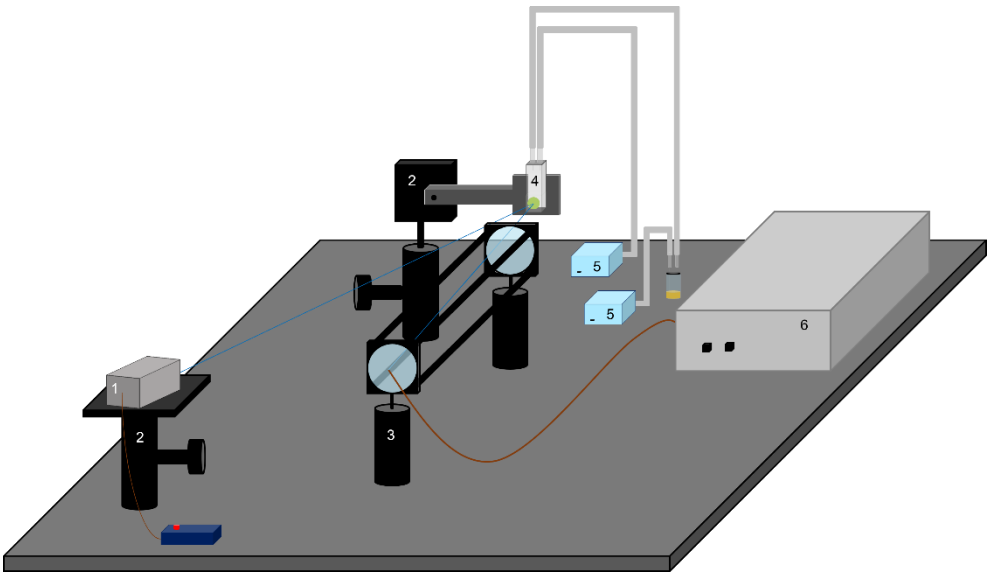

Figure 38. A schematic picture of the homemade experimental setup. The different elements of the setup are: 1) laser source; 2) positioning system; 3) lens system; 4) cuvette; 5) peristaltic pump; 6) detector.

4.3 Results and discussion

4.3.1 Synthesis and characterization of $CsPbBr_3$-PCL NIP/MIP sensor

As is mentioned before in the fabrication of MIP nanocomposites, an o-xylene solution containing PCL, $CsPbBr_3$ NCs and 3-NT or NM is spin-coated onto a glass substrate and baked at 100 ºC. The molecular imprinting process occurs by evaporation of the template during the baking step (encapsulation method).[90,95] PCL is a semicrystalline biodegradable polymer that exhibits a hydrophobic character and good processability due to the extraordinary blend compatibility, low melting point and low glass transition temperature (-60 ºC).[186,187] Moreover, the electron pairs from the C=O bond in PCL can form an intermediate adduct with the under-coordinated lead atoms in the perovskite, enhancing the perovskite grain size, achieving the grain boundary regulation, and obtaining high-quality perovskite films with low defect density and high flexibility.[188,189,190]

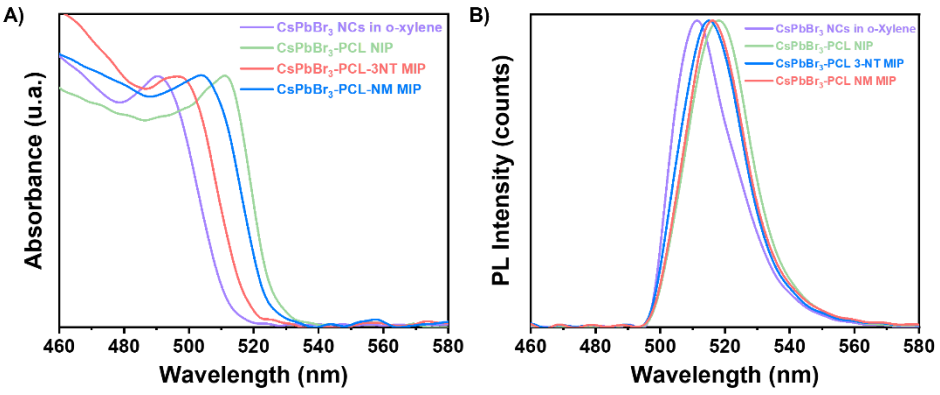

Figure 39. A) UV-vis absorbance spectra and B) emission spectra of $CsPbBr_3$ NCs in o-xylene (purple line) and embedded in the PCL polymer matrix without (green line), with 3-NT (blue line) and NM (red line) template.

The optical properties (absorbance and PL) of the $CsPbBr_3$ NCs colloidal solution and the three thin films (i.e., the sensors) were examined. Figure 39A shows the UV-Vis spectra of colloidal $CsPbBr_3$ NCs in o-xylene and embedded in the polymer matrix. The exciton absorption resonance of the colloidal NCs is observed at 490 nm. When the $CsPbBr_3$ NCs are embedded into PCL, the exciton peak is observed at 511 nm for NIP,

495 nm for 3-NT MIP, and 503 nm for NM MIP. The different exciton absorptions of $CsPbBr_3$ NCs when they are embedded in PCL is attributed to the presence of the polymer and nanocavities in MIPs.

Figure 39B illustrates the PL spectra of the colloidal $CsPbBr_3$ NCs in o-xylene solution and in the different nanocomposite thin films measured upon excitation at 404 nm. The maximum emission band of the $CsPbBr_3$ colloidal solution in o-xylene is around 511 nm with a 22 nm of FWHM. When the $CsPbBr_3$ NCs are embedded in the PCL matrix, the emission spectra changes depending on the nanocomposite composition. The $CsPbBr_3$-PCL NIP and $CsPbBr_3$-PCL-3NT MIP were red-shifted to 513 nm with an FWHM of 21 nm and 512 nm with an FWHM of 21 nm, respectively, but the emission of the $CsPbBr_3$-PCL-NM MIP was blue-shifted to 509 nm with an FWHM of 19 nm. In any case, the difference in the PL peak wavelength is significantly smaller than the one observed in the exciton absorbance. On the other hand, the shape of the emission bands of the nanocomposites is similar to that of the $CsPbBr_3$ NCs in solution. This fact indicates that the NCs embedded into the polymer matrix are well-dispersed with no aggregation.

The different optical properties of NIP and MIP are ascribed to the various porosity levels generated during the molecular imprinting of the nanocomposite. As discussed below, molecular imprinting with NM results in $CsPbBr_3$-PCL films with higher porosity than that imprinted by 3-NT. Therefore, $CsPbBr_3$ NCs have different electronic surroundings in NIP, 3-NT MIP, and NM-MIP, which can affect their optical properties (both absorbance and PL).[90]

Figure 40A shows FTIR spectra of PCL, NIP, 3-NT MIP, and NM MIP. We observed that all spectra are similar to that of PCL. The absorption bands at 2940 cm^{-1} and 2863 cm^{-1} are correlated with the asymmetric and symmetric stretching of PCL C-H alkyl chains. Moreover, the C=O stretching vibration of the ester carbonyl group could be assigned to the peak at 1722 cm^{-1}. Additionally, the peaks at 1238 cm^{-1} and 1161 cm^{-1} may be attributed to C-O-C asymmetric and symmetric stretching bands, respectively.[191] We do not observe the presence of $-NO_2$ groups in 3-NT MIP and NM-MIP nanocomposites. This indicates that the approach used to imprint the $CsPbBr_3$-PCL nanocomposite molecularly is successful: both templates (3-NT and NM) are removed entirely after the baking step.

Figure 40B shows the XRD patterns of PCL and $CsPbBr_3$-PCL nanocomposites. We observe two diffraction peaks at 15.1º and 30.5º that are assigned to the (100) and (200) planes of the cubic phase of the $CsPbBr_3$ NCs. This confirms the presence of $CsPbBr_3$ NCs embedded in the polymer matrix. The peak at 11.7º corresponds to the $CsPb_2Br_5$ phase[192] and the broad diffraction centred at 13.5º is assigned to neat PCL. Moreover, we can determine the average size of the $CsPbBr_3$ NCs in the different nanocomposites using the Scherrer equation to the (200) plane. The calculated sizes are 7.6 ± 0.5 nm for the NIP sensor, 7.2 ± 0.5 nm for the 3-NT MIP sensor and 7.3 ± 0.5 nm for the NM MIP sensor. These different NC sizes can also be consistent with the blueshifts of excitonic absorption from NIP to MIP shown in Figure 39A. These results suggest that the dispersion of $CsPbBr_3$ NCs into PCL for 3-NT and NM MIP decreases the NCs size. Recently we reported that the ageing of $CsPbBr_3$ NCs under ambient conditions might lead to an apparent reduction of the NC size.[193] Therefore, it is plausible that cavities in the MIP nanocomposite can induce a similar effect.

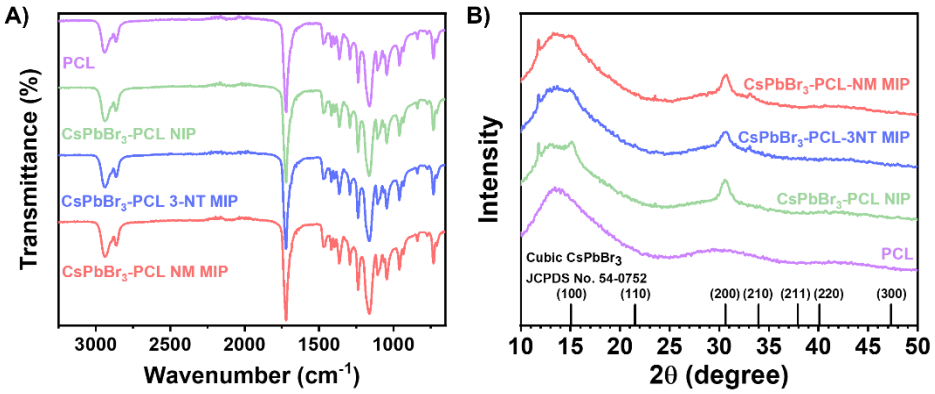

Figure 40. A) FTIR and B) XRD spectra for PCL, $CsPbBr_3$-PCL NIP, $CsPbBr_3$-PCL 3-NT MIP, and $CsPbBr_3$-PCL NM MIP.

The cubic morphology of the $CsPbBr_3$ NCs is confirmed by TEM (Figure 41A), revealing a uniform size distribution of $CsPbBr_3$ NCs. From TEM images, we measured an average size of 7.4 ± 1.7 nm for the NIP, 7.0 ± 1.3 nm for 3-NT MIP and 7.3 ± 1.2 nm for NM MIP. These sizes are in good agreement with those deduced from XRD. Figure 41B represents the size distribution of the 3-NT MIP sensor. From the HRTEM image (Figure 41C), the measured interplanar distance of 5.6 Å for the 3-NT MIP sensor corresponds to the spacing of the (100) plane measured by XRD (5.8 Å). The elemental mapping of the

$CsPbBr_3$-PCL 3-NT MIP was also performed by HRTEM (Figure 41D) and confirmed the presence of Cs, Pb and Br from the perovskite nanocrystals.

The surface morphology of the NIP, 3-NT MIP, and NM MIP thin films was characterized by SEM and compared to a PCL film (Figure 41E). Both PCL and NIP films show a flat and smooth surface. The presence of $CsPbBr_3$ NCs (average size 7 nm) inside the PCL matrix does not influence the surface topography. This reveals that $CsPbBr_3$ NCs are homogeneously dispersed inside PCL, and they do not aggregate. On the other hand, both MIP sensors exhibit a rougher surface with some topographic defects like bumps. These defects are generated after the removal of the template and are therefore related to molecular imprinting. Specifically, the average size of the surface defects is 350 nm and 800 nm for NM MIP and 3-NT MIP sensor, respectively. Therefore, NM MIP shows a higher number of defects per area than 3-NT MIP. These results would suggest that the molecular imprinting in NM MIP is higher than in 3-NT MIP.

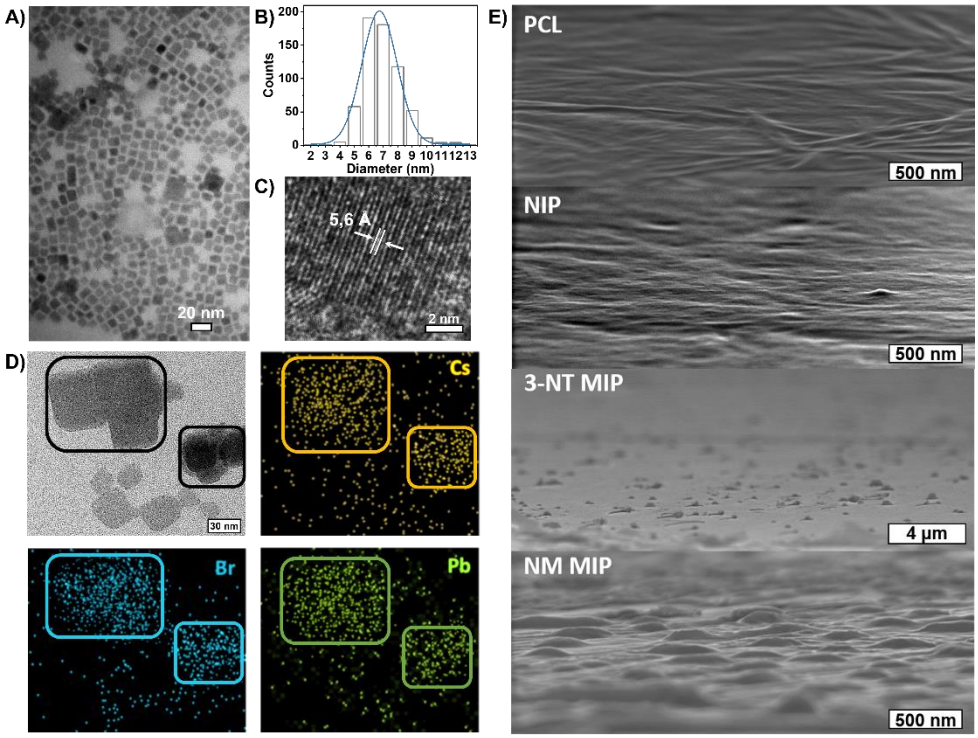

Figure 41. A) TEM image B) size distribution of $CsPbBr_3$ NCs C) HRTEM, and D) HRTEM compositional mapping of $CsPbBr_3$-PCL 3-NT MIP. E) SEM images of the surface morphology of PCL, NIP, 3-NT MIP, and NM MIP thin films.

4.3.2 Sensing of 3-NT in the vapour phase

The sensing capability of the $CsPbBr_3$-PCL MIP and NIP nanocomposites was evaluated by exposing the sensors to vapours of 3-NT using air as a gas carrier at a constant flow of 0.57 µL/min. The scheme of the MIP sensing process is shown in Figure 42A. Figure 42B exhibits the PL spectra of the $CsPbBr_3$-PCL 3-NT MIP thin film upon exposure to vapours of 3-NT for different times. Time intervals were chosen to provide enough time for the analyte to interact with the sensor. As can be observed, the interaction between the analyte and the $CsPbBr_3$ NC surface is speedy, and after only 6 s, we can already measure a noticeable PL quenching (28.2% NIP, 27.9% 3-NT MIP and 16.4% NM MIP).

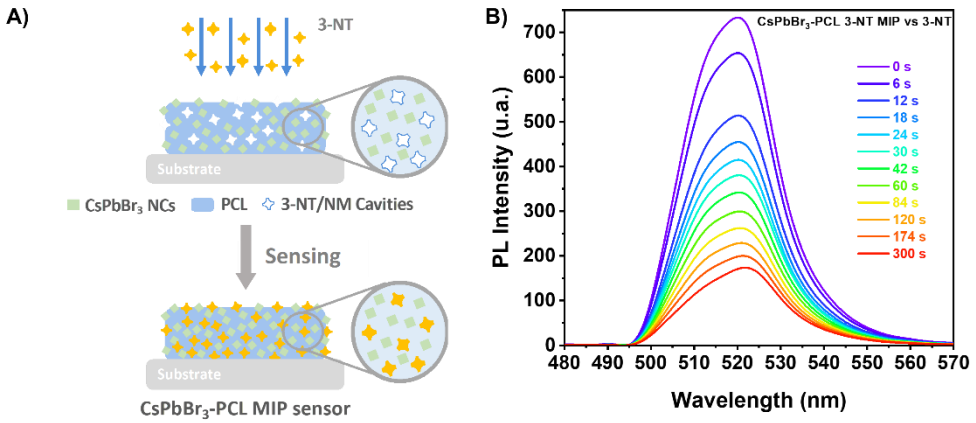

Figure 42. A) Schematic representation of the MIP sensing process. B) Fluorescence response of the $CsPbBr_3$-PCL 3-NT MIP sensor to 3-NT vapours.

Figure 43A illustrates the real-time kinetic response of the $CsPbBr_3$ nanocomposites upon exposure to vapours of 3-NT as a function of exposure time and 3-NT mass using the PL Intensity as a response variable. Both MIP sensors exhibit a remarkably higher response to 3-NT than NIP sensors. This confirms that the molecular imprinting approach successfully creates specific molecular recognition sites facilitating the interaction and the diffusion process of the taggants to the $CsPbBr_3$ NCs.[96] This increases the porosity and permeability of the thin film. After 120 s of exposure, about 69% quenching is observed for both MIP sensors, while the PL quenching of the NIP sensor is only 53%. The progressive PL decay in all sensors is caused by the increase of the number of 3-NT molecules attached to the surface of the $CsPbBr_3$ NCs. The response of all sensors to the laser without any gas exposure is negligible, which indicated a good shelf stability

as is shown in Figure 43B. The mechanism of the PL quenching when analyte molecules interact with the $CsPbBr_3$ NC surface could be attributed due to an electronic energy transfer from the sensor (electron donor) to the 3-NT (electron acceptor) because the nitro group has a strong electron-withdrawing ability that makes the aromatic ring very electron-poor relative to benzene.[161,178,183,184]

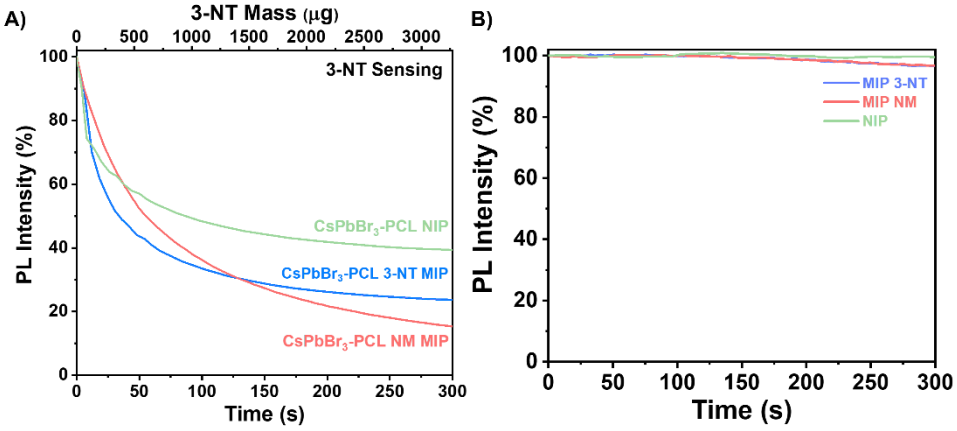

Figure 43. A) Time- and 3-NT mass-dependent PL intensity of NIP, $CsPbBr_3$-PCL 3-NT MIP and, $CsPbBr_3$-PCL NM MIP nanocomposites sensing 3-NT and B) Shelf stability of NIP, CsPbBr3-PCL 3-NT MIP and, CsPbBr3-PCL NM MIP nanocomposites to the blue laser.

The PL quenching in this system can be fitted by the following exponential curve:

$$PL_t = PL_\infty + A \cdot e^{-k \cdot t} \qquad \text{Eq. 4.1}$$

where PL_t is the PL intensity at a given time, PL_∞ is the response when the sensor is saturated by the analyte, and k is the binding rate constant.

Table 6. Kinetic binding constants and maximum PL quenching for $CsPbBr_3$-PCL sensors exposed to 3-NT vapours

Sensor	PL_∞ (%)	k (μs^{-1})
$CsPbBr_3$-PCL NIP	-60.3 ± 0.7	23.1 ± 2.0
$CsPbBr_3$-PCL 3-NT MIP	-73.8 ± 0.9	29.9 ± 1.9
$CsPbBr_3$-PCL NM MIP	-83.5 ± 0.5	14.3 ± 0.4

The results obtained from fitting the saturating function are listed in Table 6. NM MIP sensor shows the highest response to 3-NT (PL_∞ = -83.5 %) followed by 3-NT MIP (PL_∞

= -73.8 %) and NIP (PL_∞ = -60.3 %). The adsorption of 3-NT molecules on the surface of the $CsPbBr_3$ NCs is a strongly time-dependent phenomenon, which is determined by the vapour-phase analyte transport to the NCs and the subsequent chemical interaction rate.[83] The analyte binding rate (slope of the curve at any point) is mainly determined by the number of accessible $CsPbBr_3$ NCs (binding sites) embedded into the PCL matrix and the analyte concentration in the vapour phase, which is correlated to their vapour pressure. The molecular imprinting of the $CsPbBr_3$-PLC nanocomposite with 3-NT or NM generates nano- or microcavities and increases the porosity of the sensor and the permeability. This is in good agreement with the surface topography shown in Figure 41E. Consequently, the accessibility of analytes to the binding sites is strongly enhanced. Furthermore, the selectivity is enhanced because the sensors can recognize the target analytes.[194] The response of the different sensors to the analyte is cumulative over time until almost no more binding sites are available.

The maximum binding rate is achieved at the beginning of the sensing process when all the binding sites are empty. The limiting step of the process changes during the sensing. In the beginning, the limiting factor is mainly the analyte mass transport from the gas to the $CsPbBr_3$ NC binding sites, while the interaction analyte-$CsPbBr_3$ NCs controls the later stages. Figure 44A shows the sensor's response within the first 30 s of the sensing process. As we can observe, the PL decays rapidly with increasing the amount of 3-NT up to 300 µg. Within the first 10 s, the NIP sensor shows a faster response than 3-NT MIP and NM MIP sensors. This can be explained by the different porosities generated during the molecular imprinting (Figure 44B). In the NIP sensor we can assume that 3-NT molecules should attach to those $CsPbBr_3$ NCs at the surface of the nanocomposite film because there are no pores to circulate the vapour with analytes. This will produce a fast decrease of binding sites and saturation to PL_∞. It is well known that we need a minimum number (tens or hundreds) of molecules bound to PVK NCs to generate surface defects and produce a change in the PL. When sensor films are more porous (MIP ones), vapours will circulate deeper in the film and more NCs will be accessible to the analytes (this leads to higher PL_∞), and hence the analyte/NC ratio is lower at a given time. For this reason, we expect a relatively slower sensor response. According to previous results, the porosity of the sensors follow the order NM MIP > 3-NT MIP > NIP. This would explain why NIP exhibit a shorter response time than 3-NT MIP and NM MIP.

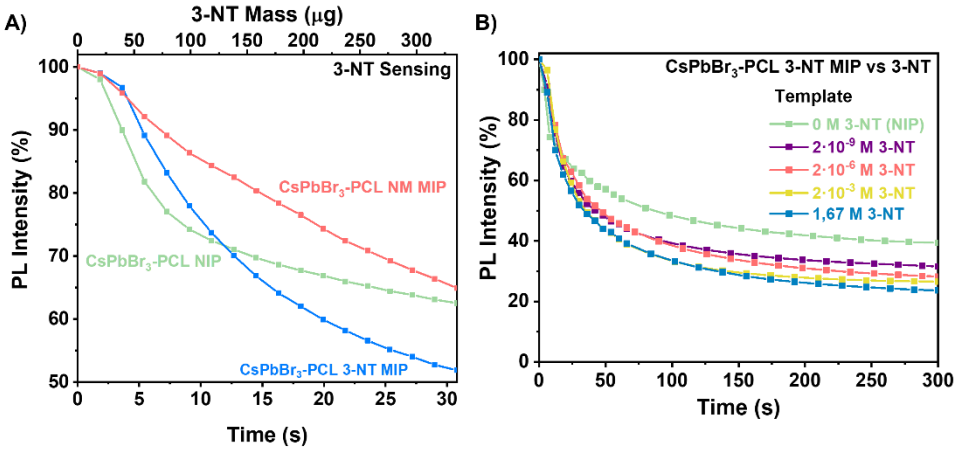

Figure 44. A) PL intensity as a function of the amount of 3-NT and time exposure and B) Real-time response of the $CsPbBr_3$-PCL nanocomposite imprinted with different concentrations of 3-NT upon exposure to 3-NT vapours.

To evaluate the quenching efficiency of the analyte, the sensing results were fitted to the Stern-Volmer equation (Figure 45):

$$\frac{I_0}{I} = 1 + K_{SV} \cdot C_{3-NT} \qquad \text{Eq. 4.2}$$

where I_0 is the PL intensity before sensing, I is the PL intensity at a given concentration of quencher, K_{SV} is the quenching constant of 3-NT and, $C_{3\text{-}NT}$ is the concentration of the 3-NT.

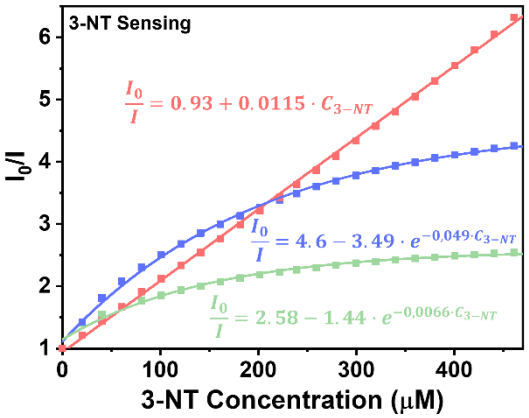

Figure 45. Stern-Volmer plots for NIP (green line), CsPbBr3-PCL 3-NT MIP (blue line) and, CsPbBr3-PCL NM MIP (red line) sensors with increasing concentration of 3-NT.

As can be observed, the exposure of the $CsPbBr_3$-PCL NIP and $CsPbBr_3$-PCL 3-NT MIP to 3-NT vapours follows an exponential relationship, whereas a good linear correlation is shown with $CsPbBr_3$-PCL NM MIP (R^2=0.9996). This upward deviation from the linear Stern-Volmer law has been reported in many experimental systems depending on the underlying quenching mechanism: contact quenching and collisional quenching. On the other hand, non-linear Stern-Volmer plots can also occur in the case of purely collisional quenching if some of the fluorophores are less accessible than others.[195] The linear Stern-Volmer relation of the NM MIP sensor suggests that the PL dropping mechanism is predominantly due to a collisional quenching between the $CsPbBr_3$ NCs and the analyte. However, the exponential fitting of the NIP and 3-NT MIP data to 3-NT vapours may indicate that some PVK NCs are less accessible than others for 3-NT MIP and NIP sensors. This is in good agreement with the real-time kinetic results shown in Figure Figure 43A with as shown in the surface topography shown in Figure 41E and gas chromatography (see below in Figure 48). For that reason, the different number of accessible binding sites between in each sensor might be related to the deviation from the linearity. From Figure 44A, we can also determine the limit of detection (LOD) of the sensors; this is the lowest analyte concentration to produce a reliably distinguished PL decay from the blank. LOD is determined to be 19.7 µg, which corresponds to 218 ppb, 1.59 µM or a PL quenching of 2% for the NIP sensor and 1% for both MIP sensors.

The sensitivity and the response time of the MIP sensor depend on the concentration of the template. Figure 44B illustrates the influence of the template concentration on the 3-NT MIP sensor upon exposure to 3-NT vapours. After 300 s, the PL intensity decays from 60% for the NIP sensor (0 M 3-NT) to 76 % for the 3-NT MIP sensor with 1.67 M 3-NT concentration, i.e., the highest response (PL quenching percentage) to 3-NT. However, this response is practically the same as that prepared from $2{\cdot}10^{-3}$ M 3-NT (73 %), whereas, for $2{\cdot}10^{-6}$ M and $2{\cdot}10^{-9}$ M 3-NT, the MIP sensor response at 300 s clearly decreases to 71% and 68%, respectively. The number of molecular recognition sites would increase with the template concentration. The maximum response is reached when the template concentration is 10^{-3} M. The number of molecular sites generated during the molecular imprint does not increase proportionally with 3-NT concentration: only a finite number of molecular sites are generated when the solution is formulated from 10^{-9} to 10^{-3} M 3-NT. Further increase does not result in more accessible selective sites. For that reason, the amount of 3-NT has an essential role in the sensing performance.

The reversibility of the sensors is also tested to have a deeper insight into the nature of the analyte binding between the $CsPbBr_3$ NCs and 3-NT vapours. Every exposure cycle consists of an exposure to an analyte flow for 60 s followed by exposure to airflow for 60 s. Figure 46 shows that the PL intensity decreases significantly when the sensor is exposed to 3-NT for 60 s. Afterwards, when exposed to airflow, they recover the PL of around 83%, 78% and 72% for NIP, 3-NT MIP and NM MIP, respectively. The reversibility is possible because the OAm and OA ligands (amino and carboxylate ligands) are remarkably labile, dynamic and are suitable leaving ligands. OAm and OA can be easily exchanged by other ligands, as already observed in PbS QDs.[140] As a result, OAm and OA can exchange their position in the $CsPbBr_3$ NC by the analyte. Once the analyte is removed, OAm and OA can return to the original positions.[83,196]

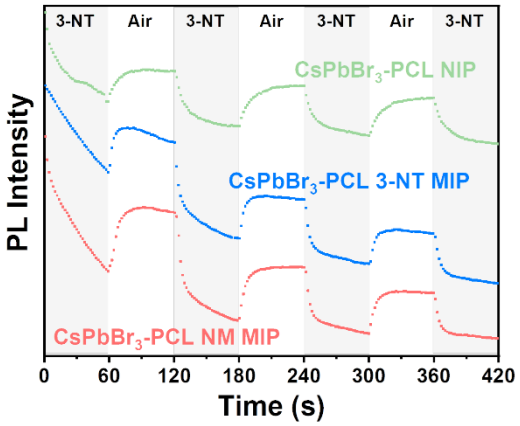

Figure 46. Real-time response of the $CsPbBr_3$-PCL NIP and $CsPbBr_3$-PCL 3-NT and NM MIP sensors under repeated exposure cycles to 3-NT vapours (grey areas) and air (white areas).

After four sensing and recovering cycles, the NIP sensor response decays and recovers approximately to the initial PL intensity after every cycle. The NIP sensor is almost reversible. Figure 47 shows the possible mechanism. The reversibility of NIP sensor is because 3-NT molecules are only adsorbed within the first few nanometres (Figure 47) of the 100 nm-thick film. As a result, 3-NT can be easily desorbed when exposed to an airflow with an average recovery time of 22 s. On the other hand, both 3-NT MIP and NM MIP sensors exhibit a certain hysteresis after every sensing and recovery cycle. Therefore 3-NT MIP and NM MIP sensors are partially reversible with an average recovery time of 12 and 14 s respectively. As suggested in Figure 47, after the molecular imprinting, the 3-NT molecules are adsorbed not only at the surface of the 100 nm-thick sensing films, but also deeper in the film due to the specific cavities generated after the

template removal. Only those 3-NT molecules located at the surface are desorbed during every recovering cycle, but not those located at the bottom of the film.

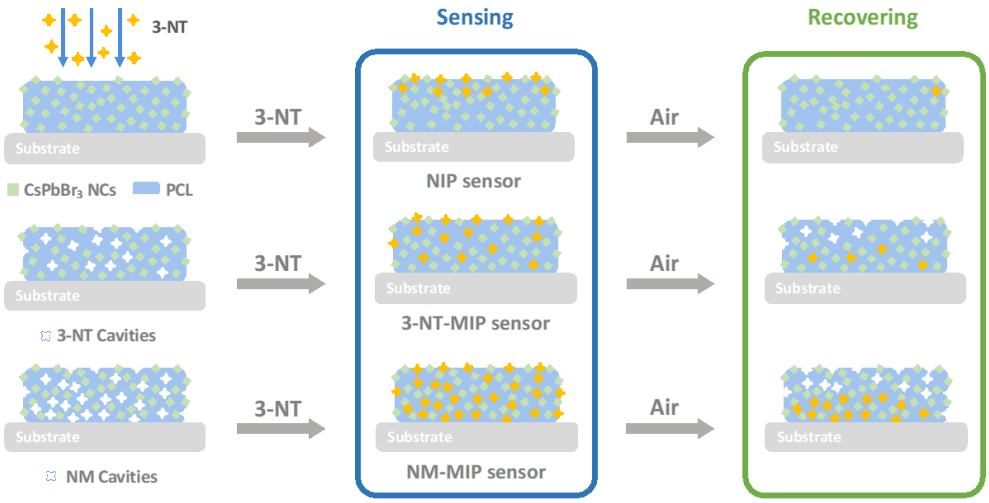

Figure 47. Schematic representation of the NIP/MIP sensing process

Gas chromatography was employed to measure quantitatively how effective the adsorption of 3-NT in NIP, 3-NT MIP and NM MIP sensor is. Gas chromatograms before sensing are shown in Figure 48A. In the case of 3-NT MIP, chromatography confirms the complete removal of the template, in total agreement with the results obtained in the FTIR (Figure 40A).

$CsPbBr_3$-PLC NIP/MIP nanocomposite films were exposed to 3-NT vapours for 180 s and then analyzed by gas chromatography. The chromatograms of NIP, 3-NT MIP, and NM MIP after sensing are shown in Figure 48B. The quantification was carried out by interpolation in the calibration curve (Figure 37) of the peak areas of 3-NT measured in Figure 48B. The quantity of 3-NT adsorbed by the sensors was 75 ng for NIP, 151 ng for 3-NT MIP and 285 ng for NM MIP. Chromatography confirms that molecular imprinting of $CsPbBr_3$-PCL with NM provides two times more selective binding sites than 3–NT and four times more than NIP. This suggests that the molecular imprinting in NM MIP is higher than in 3-NT MIP, as shown in the surface topography Figure 41E. The sensing performance of 3-NT follows the order NM MIP > 3-NT MIP > NIP, which is consistent with the real-time kinetic results shown in Figure 43A.

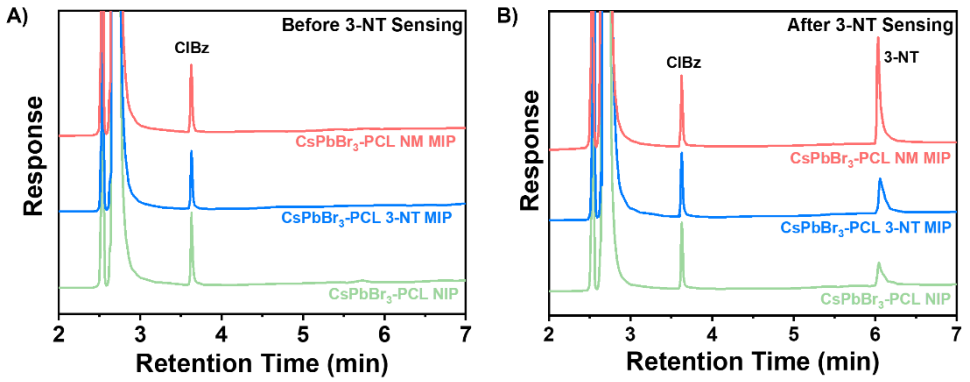

Figure 48. Gas chromatograms of the $CsPbBr_3$-PCL NIP and $CsPbBr_3$-PCL 3-NT and NM MIP sensors A) before and B) after exposure to 3-NT vapours for 180 s. C) Gas chromatography calibration curve of 3-NT using an internal standard.

Figure 49A shows the selective response of the NIP, 3-NT MIP, and NM MIP sensors to vapours of explosive taggants (3-NT, 4-NT, DMDNB) and other NO_2-containing molecules (4-NP, NM, 1-NN, 5-NI) as well as to some common solvents (acetone, acetonitrile (ACN), ethyl acetate (EtOAc), methanol (MeOH), and toluene).

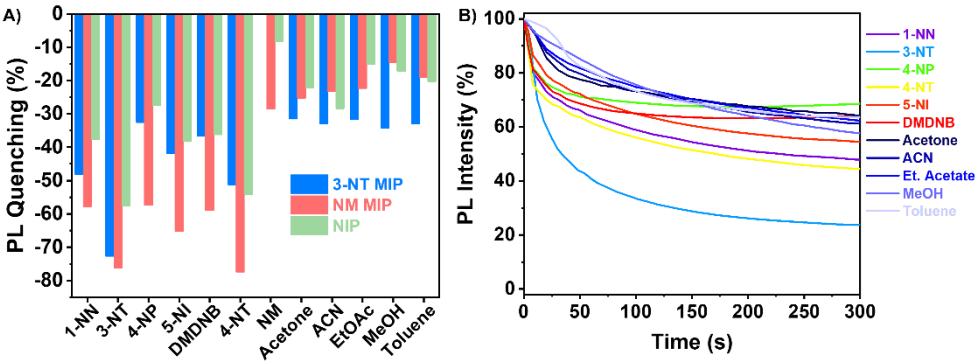

Figure 49. Selectivity of $CsPbBr_3$-PCL sensor. A) 3-NT/NM MIP and NIP sensor response to different nitro-containing compounds and some common solvents after 180 s of exposure. B) Time-dependent fluorescence intensity of $CsPbBr_3$-PCL 3-NT MIP sensor to vapours of different nitro-containing compounds and some common solvents

Generally, the results show that 3-NT MIP (Figure 49B) and NM MIP sensors interact more selectively with the explosive taggants and nitro-containing molecules than with common solvents. This trend is already observed for the NIP, but molecular imprinting significantly improves selectivity. This means that PCL shows specific permeability to

nitro compounds. The NM analyte is an exception to this tendency. This low sensor response can be attributed to rapid analyte desorption from the $CsPbBr_3$ NC surface due to the high volatility of NM. 3-NT MIP does not show sensitivity to NM.

The NM MIP sensor shows the highest response to nitro compounds, particularly when it is exposed to explosive taggants like 3-NT (76.3 %) and 4-NT (77.5 %). For the other nitro-containing analytes, the NM MIP exhibits a PL quenching of around 60 %. In the case of NM, NM MIP shows remarkable selectivity to NM compared to NIP and 3-NT MIP sensors. In contrast, NM MIP shows a low affinity for common solvents, although NM MIP is the most porous sensor. On the other hand, 3-NT MIP shows a specific response to 3-NT (72.7%), whereas, for the rest of nitro compounds, 3-NT MIP shows a similar response as that measured for NIP. This is especially striking for some compounds like 4-NT and 4-NP, which have similar sizes and shapes to 3-NT. The selectivity results confirm that molecular imprinting contributes to create specific molecular recognition towards nitro compounds, more specifically 3-NT and 4-NP.

4.4 Conclusions

In the present study, we have developed two fluorescent MIP nanocomposites based on $CsPbBr_3$ NCs embedded in PCL as a host matrix and 3-NT and NM as a template to sense and quantify trace amounts of 3-NT. Molecular imprinting takes place simultaneously during the baking step after the deposition. Both MIP sensors combine the high PL quantum yield of the $CsPbBr_3$ NCs and the high selectivity provided by the MIP to show a higher quenching response (> 75 %) than our reference NIP sensors (> 60 %) after exposure to 3-NT for 3 min. Chromatography confirms that molecular imprinting of $CsPbBr_3$-PCL with NM provides two times more selective binding sites than 3-NT and four times more than NIP. Surface topography also suggests that the molecular imprinting in NM MIP is higher than in 3-NT MIP. Consequently, our results show that 3-NT MIP and NM MIP sensors interact more selectively with the explosive taggants and nitro-containing molecules than with common solvents. This trend is already observed for the NIP, but molecular imprinting significantly improves the higher responsivity and selectivity. Particularly, NM MIP sensor exhibits the highest response to nitro compounds. These facts confirm that the specific recognition sites have been successfully generated, allowing a fast detection of 3-NT in the range of 2-3 s with LOD as low as 0.218 µg/mL.

Chapter 5

Conclusions and Future Prospects

This PhD thesis has been elaborated to develop different chemical sensors to detect explosive vapours in different environments. For this purpose, different sensing platforms based on Ag nanoparticles, CdSe quantum dots and $CsPbBr_3$ NCs embedded in a polymer matrix were synthesized, characterized, optimized, and tested. The most relevant results achieved to meet the requirements mentioned above are:

- The fabrication of solid-state hybrid nanocomposites to combine the optical properties of the nanoparticles with the polymer characteristics to enhance the chemical stability and the mechanical attributes.

- The synthesized sensing platforms can detect trace amounts of explosive or explosive taggants in the vapor phase selectively and reproducibly and also, they can be incorporated into portable systems that allow on-field analysis.

- The easy fabrication of the Ag-PEI sensor by the in-situ synthesis of the Ag NPs inside the polymer makes them cost-effective, simple, and easy-to-use optical devices. Despite the long response time, this sensors can be useful for certain applications such as in sentinels in cargo ship containers.

- The fast response time showed by the green or red CdSe-PCL sensor array and $CsPbBr_3$-PCL sensors makes them an effective real-time sensing platform to fight against an increasing terrorist threat.

- The use of the molecularly imprinting technology in the Ag-PEI or $CsPbBr_3$-PCL sensing platforms provides an excellent specific molecular recognition to different explosive taggants, which allows the effective detection and quantification.

- The multiparametric analysis of the luminescent QD-based nanocomposites response enable and effective identification of some explosive taggants.

- All sensors show a wide linear response to explosive taggants which forms the basis to be used as a quantitative sensor.

- Despite the good results obtained by the Ag-PEI sensor, fluorescence-based nanocomposites, such as CdSe QDs and $CsPbBr_3$ NCs, provide better results than LSPR-based sensors. It is because a small change in their environment causes a large response due to their high sensitivity.

- When both fluorescence sensors are compared, the recognition sites generated in the $CsPbBr_3$-PCL nanocomposites by the molecularly imprinted technology contribute to enhance their selectivity and sensitivity with respect to the CdSe QDs sensors. As a result, $CsPbBr_3$-PCL MIP sensors are the most promising sensor for the explosive detection.

On the basis of our results, different aspects of the sensors can be improved, as well as other works can be carried out in the future.

- The response time of the Ag-PEI sensor might be reduced operating with higher analyte vapor pressures or temperature.

- The combination of plasmonic and fluorescent nanoparticles might increase the sensitivity and the selectivity of the sensors.

- The replacement of cesium lead halide perovskite by other lead-free halide perovskites would contribute to reduce the environmental footprint.

- All sensors can be exposed to homemade explosives, such as TATP or HMTD to test the effectivity because they do not contain explosive taggants in their composition.

Capítol 5

Conclusions i perspectives de futur

Aquesta tesi doctoral s'ha elaborat amb la finalitat de desenvolupar diferents sensors químics per detectar vapors explosius en diferents ambients. Amb aquest propòsit, es van sintetitzar, caracteritzar, optimitzar i provar diferents plataformes de detecció basades en nanopartícules Ag, punts quàntics de CdSe i NCs de $CsPbBr_3$ embeguts en una matriu polimèrica. Els resultats més rellevants aconseguits per complir els requisits esmentats anteriorment són:

- La fabricació de nanocompòsits híbrids en estat sòlid per combinar les propietats òptiques de les nanopartícules amb les del polímer per tal de millorar l'estabilitat química i les propietats mecàniques.

- Les plataformes de detecció sintetitzades poden detectar traces de marcadors d'explosius o explosius en fase de vapor de manera selectiva i reproduïble i, a més, es poden incorporar a sistemes portàtils que permeten l'anàlisi sobre el terreny.

- La facilitat de fabricació del sensor d'Ag-PEI degut a la síntesi in situ de les Ag NPs dins del polímer, els fa dispositius òptics rendibles, senzills i fàcils d'utilitzar. Malgrat el llarg temps de resposta, aquests sensors poden ser útils per a determinades aplicacions com en sentinelles en els contenidors de vaixells de càrrega.

- El temps de resposta ràpid que mostren la matriu de sensors verd o roig de CdSe-PCL i els sensors de $CsPbBr_3$-PCL els converteix en una plataforma de detecció eficaç en temps real per a lluitar contra una creixent amenaça terrorista.

- L'ús de la tecnologia d'impressió molecular a les plataformes de detecció d'Ag-PEI o $CsPbBr_3$-PCL proporciona un excel·lent reconeixement molecular específic per a diferents marcadors d'explosius, el que permet la seua detecció i quantificació de forma efectiva.

- L'anàlisi multi-paramètric de la resposta dels nanocompòsits basats en QDs luminescents permet la identificació eficaç d'alguns marcadors d'explosius.

- Tots els sensors mostren una resposta lineal àmplia als marcadors d'explosius que constitueixen la base per a poder ser utilitzat com a sensor quantitatiu.

- Malgrat els bons resultats obtinguts pel sensor d'Ag-PEI, els nanocompòsits basats en el mecanisme de fluorescència, com els de QDs de CdSe i NCs de $CsPbBr_3$, proporcionen millors resultats que els sensors basats en LSPR. Això es degut a que un petit canvi en el seu entorn provoca una gran resposta a causa de la seua alta sensibilitat.

- Quan es comparen ambdós sensors de fluorescents, els llocs de reconeixement generats en els nanocompòsits de $CsPbBr_3$-PCL amb la tecnologia d'impressió molecular contribueixen a millorar la seua selectivitat i sensibilitat respecte als sensors formats per QDs de CdSe. Com a resultat, els sensors impresos molecularment de $CsPbBr_3$-PCL són els més prometedors per a la detecció d'explosius.

A partir dels nostres resultats es poden millorar diferents aspectes dels sensors, així com també es poder dur a terme altres treballs en el futur.

- El temps de resposta del sensor Ag-PEI es podria reduir treballant amb pressions de vapor o temperatures més elevades.

- La combinació de nanopartícules plasmòniques i fluorescents podria augmentar la sensibilitat i la selectivitat dels sensors.

- La substitució de la perovskita d'halogenur de plom i cesi per altres perovskites sense plom contribuirien a reduir la petjada ambiental.

- Tots els sensors es poden exposar a explosius casolans, com ara el TATP o l'HMTD per provar la seua efectivitat ja que aquests no contenen marcadors explosius en la seua composició.

Chapter 6

Bibliography

(1) Singh, S. Sensors-An Effective Approach for the Detection of Explosives. *J. Hazard. Mater.* **2007**, *144*, 15–28.

(2) Zhang, C. Review of the Establishment of Nitro Group Charge Method and Its Applications. *J. Hazard. Mater.* **2009**, *161*, 21–28.

(3) Agrawal, J. P.; Hodgson, R. D. *Organic Chemistry of Explosives*; John Wiley & Sons, Ltd, 2006.

(4) Farrell, M. E.; Holthoff, E. L.; Pellegrino, P. M. Laser-Based Optical Detection of Explosives. In *Laser-Based Optical Detection of Explosives*; CRC Press, 2018; pp 1–3.

(5) Mohanty, B. Physics of Explosion Hazards. In *Forensic Investigation of Explosions*; 2011; pp 19–52.

(6) Meyers, S.; Shanley, E. S. Industrial Explosives - a Brief History of Their Development and Use. *J. Hazard. Mater.* **1990**, *23*, 183–201.

(7) Field, S. Boom!: The Chemistry and History of Explosives. 2017, p 200.

(8) Urbanski, T.; Laverton, S.; Ornaf, W. *Chemistry and Technology of Explosives. Vol. 1.*; 1964.

(9) Klapötke, T. M. *Chemistry of High-Energy Materials*, 4th ed.; Walter de Gruyter GmbH, 2017.

(10) Elbeih, A.; Pachman, J.; Zeman, S.; Trzcinski, W. A.; Akstein, Z. Advanced Plastic Explosive Based on BCHMX Compared with Composition C4 and Semtex 10. *New Trends Res. Energ. Mater., Proc. Semin. 14th* **2011**, 119–126.

(11) Akhavan, J. *The Chemistry of Explosives*; Royal Society of Chemistry, 2011.

(12) Widmer, L.; Watson, S.; Schlatter, K.; Crowson, A. Development of an LC/MS

Method for the Trace Analysis of Triacetone Triperoxide (TATP). *Analyst* **2002**, *127*, 1627–1632.

(13) Türker, L. Peroxide Based Organic Explosives. *Earthline J. Chem. Sci.* **2021**, *6*, 165–208.

(14) Marshall, M.; Oxley, J. C. Explosives: The Threats and the Materials. In *Aspects of Explosives Detection*; Elsevier, 2009; pp 11–26.

(15) U.S. Department of Alcohol Tobacco and Firearms. Triacetone Triperoxide (TATP): Indicators of Acquisition and Manufacture, and Considerations for Response. **2019**.

(16) *Reducing the Threat of Improvised Explosive Device Attacks by Restricting Access to Explosive Precursor Chemicals*; The National Academies Press: Washington, DC., 2018.

(17) Gamble, S. C.; Campos, L. C.; Morgan, R. M. Detection of Trace Peroxide Explosives in Environmental Samples Using Solid Phase Extraction and Liquid Chromatography Mass Spectrometry. *Environ. Forensics* **2017**, *18*, 50–61.

(18) Jensen, L.; Mortensen, P. M.; Trane, R.; Harris, P.; Berg, R. W. Reaction Kinetics of Acetone Peroxide Formation and Structure Investigations Using Raman Spectroscopy and X-Ray Diffraction. *Appl. Spectrosc.* **2009**, *63*, 92–97.

(19) Almenar, E.; Costero, A. M.; Gaviña, P.; Gil, S.; Parra, M. Towards the Fluorogenic Detection of Peroxide Explosives through Host–Guest Chemistry. *R. Soc. Open Sci.* **2018**, *5*, 171787.

(20) Goodpaster, J. Explosives. In *Forensic Chemistry : Fundamentals and Applications*; Siegel, J. A., Ed.; John Wiley & Sons, Inc., 2015.

(21) Benson, S. J.; Lennard, C. J.; Maynard, P.; Hill, D. M.; Andrew, A. S.; Roux, C. Forensic Analysis of Explosives Using Isotope Ratio Mass Spectrometry (IRMS) — Preliminary Study on TATP and PETN. *Sci. Justice* **2009**, *49*, 81–86.

(22) Oxley, J. C.; Smith, J. L.; Porter, M.; McLennan, L.; Colizza, K.; Zeiri, Y.; Kosloff, R.; Dubnikova, F. Synthesis and Degradation of Hexamethylene Triperoxide Diamine (HMTD). *Propellants, Explos. Pyrotech.* **2016**, *41*, 334–350.

(23) Matyáš, R.; Pachman, J. Organic Peroxides. In *Primary Explosives*; Springer-

Verlag Berlin Heidelberg, 2013; pp 255–287.

(24) Espinosa-Fuentes, E. A.; Peña-Quevedo, A. J.; Pacheco-Londoño, L. C.; Infante-Castillo, R.; Hernández-Rivera, S. P. A Review of Peroxide Based Homemade Explosives: Characterization and Detection. In *Explosive Materials: Classification, Composition and Properties*; Janssen T. J., Ed.; Nova Science Publishers, Inc, 2011.

(25) Zapata, F.; García-Ruiz, C. Determination of Nanogram Microparticles from Explosives after Real Open-Air Explosions by Confocal Raman Microscopy. *Anal. Chem.* **2016**, *88*, 6726–6733.

(26) Keshavarz, M. H.; Pouretedal, H. R. Predicting the Detonation Velocity of CHNO Explosives by a Simple Method. *Propellants, Explos. Pyrotech.* **2005**, *30*, 105–108.

(27) Venugopalan, S. Two Faces of Explosion: Deflagration and Detonation. In *Demystifying Explosives*; Elsevier, 2015; pp 51–69.

(28) Pekalski, A. A.; Zevenbergen, J. F.; Lemkowitz, S. M.; Pasman, H. J. A Review of Explosion Prevention and Protection Systems Suitable as Ultimate Layer of Protection in Chemical Process Installations. *Process Saf. Environ. Prot.* **2005**, *83*, 1–17.

(29) O'Mahony, A. M.; Wang, J. Nanomaterial-Based Electrochemical Detection of Explosives: A Review of Recent Developments. *Anal. Methods* **2013**, *5*, 4296.

(30) Sun, X.; Wang, Y.; Lei, Y. Fluorescence Based Explosive Detection: From Mechanisms to Sensory Materials. *Chem. Soc. Rev.* **2015**, *44*, 8019–8061.

(31) Lu, D.; Cagan, A.; Munoz, R. A. A.; Tangkuaram, T.; Wang, J. Highly Sensitive Electrochemical Detection of Trace Liquid Peroxide Explosives at a Prussian-Blue 'Artificial-Peroxidase' Modified Electrode. *Analyst* **2006**, *131*, 1279.

(32) Senesac, L.; Thundat, T. G. Nanosensors for Trace Explosive Detection. *Mater. Today* **2008**, *11*, 28–36.

(33) Zapata, F.; García-Ruiz, C. Chemical Classification of Explosives. *Crit. Rev. Anal. Chem.* **2020**, *51*, 1–18.

(34) Jeunieau, L.; Lefebvre, M. H. Mixtures of TATP with Oxidizing Components:

Explosive and Thermal Properties. In *49th International Annual Conference of the Fraunhofer ICT*; 2018.

(35) Agrawal, J. P. *High Energy Materials: Propellants, Explosives and Pyrotechnics*; WILEY-VCH Verlag GmbH & Co. KGaA, 2010.

(36) Meyer, R.; Köhler, J.; Homburg, A. *Explosives*, 6th ed.; John Wiley & Sons, Inc., 2007.

(37) Sinditskii, V. P.; Kolesov, V. I.; Egorshev, V. Y.; Patrikeev, D. I.; Dorofeeva, O. V. Thermochemistry of Cyclic Acetone Peroxides. *Thermochim. Acta* **2014**, *585*, 10–15.

(38) Witko, E. M.; Korter, T. M. Terahertz Spectroscopy of the Explosive Taggant 2,3-Dimethyl-2,3-Dinitrobutane. *J. Phys. Chem. A* **2012**, *116*, 6879–6884.

(39) Roucou, A.; Kleiner, I.; Goubet, M.; Bteich, S.; Mouret, G.; Bocquet, R.; Hindle, F.; Meerts, W. L.; Cuisset, A. Towards the Detection of Explosive Taggants: Microwave and Millimetre-Wave Gas-Phase Spectroscopies of 3-Nitrotoluene. *ChemPhysChem* **2018**, *19*, 1056–1067.

(40) Loch, A. S.; Stoltzfus, D. M.; Burn, P. L.; Shaw, P. E. High-Sensitivity Poly(Dendrimer)-Based Sensors for the Detection of Explosives and Taggant Vapors. *Macromolecules* **2020**, *53*, 1652–1664.

(41) Wang, J.; Thongngamdee, S.; Lu, D. Sensitive Voltammetric Sensing of the 2,3-Dimethyl-2,3-Dinitrobutane (Dmnb) Explosive Taggant. *Electroanalysis* **2006**, *18*, 971–975.

(42) Hutchinson, K. L.; Stoltzfus, D. M.; Burn, P. L.; Shaw, P. E. Luminescent Poly(Dendrimer)s for the Detection of Explosives. *Mater. Adv.* **2020**, *1*, 837–844.

(43) Ewing, R. G.; Waltman, M. J.; Atkinson, D. A.; Grate, J. W.; Hotchkiss, P. J. The Vapor Pressures of Explosives. *TrAC Trends Anal. Chem.* **2013**, *42*, 35–48.

(44) Thomas III, S. W.; Amara, J. P.; Bjork, R. E.; Swager, T. M. Amplifying Fluorescent Polymer Sensors for the Explosives Taggant 2,3-Dimethyl-2,3-Dinitrobutane (DMNB). *Chem. Commun.* **2005**, 4572.

(45) Salinas, Y.; Martínez-Máñez, R.; Marcos, M. D.; Sancenón, F.; Costero, A. M.; Parra, M.; Gil, S. Optical Chemosensors and Reagents to Detect Explosives.

Chem. Soc. Rev. **2012**, *41*, 1261–1296.

(46) Yuan, C. X.; Fan, Y. R.; Tao-Zhang; Guo, H. X.; Zhang, J. X.; Wang, Y. L.; Shan, D. L.; Lu, X. Q. A New Electrochemical Sensor of Nitro Aromatic Compound Based on Three-Dimensional Porous Pt-Pd Nanoparticles Supported by Graphene-Multiwalled Carbon Nanotube Composite. *Biosens. Bioelectron.* **2014**, *58*, 85–91.

(47) Lotspeich, E.; Kitts, K.; Goodpaster, J. Headspace Concentrations of Explosive Vapors in Containers Designed for Canine Testing and Training: Theory, Experiment, and Canine Trials. *Forensic Sci. Int.* **2012**, *220*, 130–134.

(48) Furton, K. The Scientific Foundation and Efficacy of the Use of Canines as Chemical Detectors for Explosives. *Talanta* **2001**, *54*, 487–500.

(49) Oxley, J. C.; Waggoner, L. P. Detection of Explosives by Dogs. In *Aspects of Explosives Detection*; Elsevier, 2009; pp 27–40.

(50) Yinon, J. Field Detection and Monitoring of Explosives. *TrAC Trends Anal. Chem.* **2002**, *21*, 292–301.

(51) Mu, R.; Shi, H.; Yuan, Y.; Karnjanapiboonwong, A.; Burken, J. G.; Ma, Y. Fast Separation and Quantification Method for Nitroguanidine and 2,4-Dinitroanisole by Ultrafast Liquid Chromatography–Tandem Mass Spectrometry. *Anal. Chem.* **2012**, *84*, 3427–3432.

(52) Holmgren, E.; Ek, S.; Colmsjö, A. Extraction of Explosives from Soil Followed by Gas Chromatography–Mass Spectrometry Analysis with Negative Chemical Ionization. *J. Chromatogr. A* **2012**, *1222*, 109–115.

(53) Barron, L.; Gilchrist, E. Ion Chromatography-Mass Spectrometry: A Review of Recent Technologies and Applications in Forensic and Environmental Explosives Analysis. *Anal. Chim. Acta* **2014**, *806*, 27–54.

(54) Gillibert, R.; Huang, J. Q.; Zhang, Y.; Fu, W. L.; Lamy de la Chapelle, M. Explosive Detection by Surface Enhanced Raman Scattering. *TrAC - Trends Anal. Chem.* **2018**, *105*, 166–172.

(55) Hakonen, A.; Andersson, P. O.; Stenbæk Schmidt, M.; Rindzevicius, T.; Käll, M. Explosive and Chemical Threat Detection by Surface-Enhanced Raman

Scattering: A Review. *Anal. Chim. Acta* **2015**, *893*, 1–13.

(56) Wells, K.; Bradley, D. A. A Review of X-Ray Explosives Detection Techniques for Checked Baggage. *Appl. Radiat. Isot.* **2012**, *70*, 1729–1746.

(57) Harding, G.; Harding, A. X-Ray Diffraction Imaging for Explosives Detection. In *Counterterrorist Detection Techniques of Explosives*; Elsevier, 2007; pp 199–235.

(58) Crespy, C.; Duvauchelle, P.; Kaftandjian, V.; Soulez, F.; Ponard, P. Energy Dispersive X-Ray Diffraction to Identify Explosive Substances: Spectra Analysis Procedure Optimization. *Nucl. Instruments Methods Phys. Res. Sect. A Accel. Spectrometers, Detect. Assoc. Equip.* **2010**, *623*, 1050–1060.

(59) Cetó, X.; O' Mahony, A. M.; Wang, J.; del Valle, M. Simultaneous Identification and Quantification of Nitro-Containing Explosives by Advanced Chemometric Data Treatment of Cyclic Voltammetry at Screen-Printed Electrodes. *Talanta* **2013**, *107*, 270–276.

(60) Wang, J. Electrochemical Sensing of Explosives. *Electroanalysis* **2007**, *19*, 415–423.

(61) Griffin, P. J. Nuclear Technologies. In *Aspects of Explosives Detection*; Elsevier, 2009; pp 59–87.

(62) Lanza, R. C. Neutron Techniques for Detection of Explosives. In *Counterterrorist Detection Techniques of Explosives*; Elsevier, 2007; pp 131–155.

(63) Anferov, V. P.; Mozjoukhine, G. V.; Fisher, R. Pulsed Spectrometer for Nuclear Quadrupole Resonance for Remote Detection of Nitrogen in Explosives. *Rev. Sci. Instrum.* **2000**, *71*, 1656–1659.

(64) Li, Z.; Askim, J. R.; Suslick, K. S. The Optoelectronic Nose: Colorimetric and Fluorometric Sensor Arrays. *Chem. Rev.* **2019**, *119*, 231–292.

(65) Guo, C. X.; Lei, Y.; Li, C. M. Porphyrin Functionalized Graphene for Sensitive Electrochemical Detection of Ultratrace Explosives. *Electroanalysis* **2011**, *23*, 885–893.

(66) Abargues, R.; Rodriguez-Canto, P. J.; Albert, S.; Suarez, I.; Martínez-Pastor, J. P. Plasmonic Optical Sensors Printed from Ag–PVA Nanoinks. *J. Mater. Chem.*

C **2014**, *2*, 908–915.

(67) Rodríguez-Cantó, P. J.; Abargues, R.; Gordillo, H.; Suárez, I.; Chirvony, V.; Albert, S.; Martínez-Pastor, J. UV-Patternable Nanocomposite Containing CdSe and PbS Quantum Dots as Miniaturized Luminescent Chemo-Sensors. *RSC Adv.* **2015**, *5*, 19874–19883.

(68) Andres-Penares, D.; Canet-Albiach, R.; Noguera-Gomez, J.; Martínez-Pastor, J. P.; Abargues, R.; Sánchez-Royo, J. F. Two-Dimensional Indium Selenide for Sulphur Vapour Sensing Applications. *Nanomaterials* **2020**, *10*, 1396.

(69) Behera, P.; Mohanty, A.; De, M. Functionalized Fluorescent Nanodots for Discrimination of Nitroaromatic Compounds. *ACS Appl. Nano Mater.* **2020**, *3*, 2846–2856.

(70) Abargues, R.; Albert, S.; Valdés, J. L.; Abderrafi, K.; Martínez-Pastor, J. P. Molecular-Mediated Assembly of Silver Nanoparticles with Controlled Interparticle Spacing and Chain Length. *J. Mater. Chem.* **2012**, *22*, 22204.

(71) Marqués-Hueso, J.; Abargues, R.; Canet-Ferrer, J.; Agouram, S.; Valdés, J. L.; Martínez-Pastor, J. P. Au-PVA Nanocomposite Negative Resist for One-Step Three-Dimensional e-Beam Lithography. *Langmuir* **2010**, *26*, 2825–2830.

(72) Lu, X.; Rycenga, M.; Skrabalak, S. E.; Wiley, B.; Xia, Y. Chemical Synthesis of Novel Plasmonic Nanoparticles. *Annu. Rev. Phys. Chem.* **2009**, *60*, 167–192.

(73) Haes, A. J.; Van Duyne, R. P. A Nanoscale Optical Biosensor: Sensitivity and Selectivity of an Approach Based on the Localized Surface Plasmon Resonance Spectroscopy of Triangular Silver Nanoparticles. *J. Am. Chem. Soc.* **2002**, *124*, 10596–10604.

(74) Wang, J.; Lin, W.; Cao, E.; Xu, X.; Liang, W.; Zhang, X. Surface Plasmon Resonance Sensors on Raman and Fluorescence Spectroscopy. *Sensors* **2017**, *17*, 2719.

(75) Seydack, M. Nanoparticle Labels in Immunosensing Using Optical Detection Methods. *Biosens. Bioelectron.* **2005**, *20*, 2454–2469.

(76) Toderas, F.; Baia, M.; Baia, L.; Astilean, S. Controlling Gold Nanoparticle Assemblies for Efficient Surface-Enhanced Raman Scattering and Localized

Surface Plasmon Resonance Sensors. *Nanotechnology* **2007**, *18*, 255702.

(77) Gradess, R.; Abargues, R.; Habbou, A.; Canet-Ferrer, J.; Pedrueza, E.; Russell, A.; Valdés, J. L.; Martínez-Pastor, J. P. Localized Surface Plasmon Resonance Sensor Based on Ag-PVA Nanocomposite Thin Films. *J. Mater. Chem.* **2009**, *19*, 9233.

(78) Yang, Y.; Wang, H.; Su, K.; Long, Y.; Peng, Z.; Li, N.; Liu, F. A Facile and Sensitive Fluorescent Sensor Using Electrospun Nanofibrous Film for Nitroaromatic Explosive Detection. *J. Mater. Chem.* **2011**, *21*, 11895.

(79) Toal, S. J.; Trogler, W. C. Polymer Sensors for Nitroaromatic Explosives Detection. *J. Mater. Chem.* **2006**, *16*, 2871.

(80) Enkin, N.; Sharon, E.; Golub, E.; Willner, I. Ag Nanocluster/DNA Hybrids: Functional Modules for the Detection of Nitroaromatic and RDX Explosives. *Nano Lett.* **2014**, *14*, 4918–4922.

(81) Hu, Z.; Deibert, B. J.; Li, J. Luminescent Metal–Organic Frameworks for Chemical Sensing and Explosive Detection. *Chem. Soc. Rev.* **2014**, *43*, 5815–5840.

(82) Peveler, W. J.; Roldan, A.; Hollingsworth, N.; Porter, M. J.; Parkin, I. P. Multichannel Detection and Differentiation of Explosives with a Quantum Dot Array. *ACS Nano* **2016**, *10*, 1139–1146.

(83) Harwell, J. R.; Glackin, J. M. E.; Davis, N. J. L. K.; Gillanders, R. N.; Credgington, D.; Turnbull, G. A.; Samuel, I. D. W. Sensing of Explosive Vapor by Hybrid Perovskites: Effect of Dimensionality. *APL Mater.* **2020**, *8*, 071106.

(84) Ma, Y.; Wang, S.; Wang, L. Nanomaterials for Luminescence Detection of Nitroaromatic Explosives. *TrAC Trends Anal. Chem.* **2015**, *65*, 13–21.

(85) LI, P.; LIU, J.; NAG, N.; CROZIER, P. In Situ Synthesis and Characterization of Ru Promoted Co/Al2O3 Fischer–Tropsch Catalysts. *Appl. Catal. A Gen.* **2006**, *307*, 212–221.

(86) Suárez, I.; Larrue, A.; Rodríguez-Cantó, P. J.; Almuneau, G.; Abargues, R.; Chirvony, V. S.; Martínez-Pastor, J. P. Efficient Excitation of Photoluminescence in a Two-Dimensional Waveguide Consisting of a Quantum Dot-Polymer Sandwich-Type Structure. *Opt. Lett.* **2014**, *39*, 4962.

(87) Abargues, R.; Abderrafi, K.; Pedrueza, E.; Gradess, R.; Marqués-Hueso, J.; Valdés, J. L.; Martínez-Pastor, J. Optical Properties of Different Polymer Thin Films Containing in Situ Synthesized Ag and Au Nanoparticles. *New J. Chem.* **2009**, *33*, 1720.

(88) Uthale, S. A.; Dhamal, N. A.; Shinde, D. K.; Kelkar, A. D. Polymeric Hybrid Nanocomposites Processing and Finite Element Modeling: An Overview. *Sci. Prog.* **2021**, *104*, 1–44.

(89) Mittal, V. In - Situ Synthesis of Polymer Nanocomposites. In *In-situ Synthesis of Polymer Nanocomposites*; Mittal, V., Ed.; WILEY-VCH Verlag GmbH & Co. KGaA, 2012; pp 1–25.

(90) Ma, Y.; Xu, S.; Wang, S.; Wang, L. Luminescent Molecularly-Imprinted Polymer Nanocomposites for Sensitive Detection. *TrAC Trends Anal. Chem.* **2015**, *67*, 209–216.

(91) D'Aurelio, R.; Chianella, I.; Goode, J. A.; Tothill, I. E. Molecularly Imprinted Nanoparticles Based Sensor for Cocaine Detection. *Biosensors* **2020**, *10*, 22.

(92) Song, X.; Li, J.; Wang, J.; Chen, L. Quercetin Molecularly Imprinted Polymers: Preparation, Recognition Characteristics and Properties as Sorbent for Solid-Phase Extraction. *Talanta* **2009**, *80*, 694–702.

(93) Zhang, T.; Liu, F.; Chen, W.; Wang, J.; Li, K. Influence of Intramolecular Hydrogen Bond of Templates on Molecular Recognition of Molecularly Imprinted Polymers. *Anal. Chim. Acta* **2001**, *450*, 53–61.

(94) Shi, Y.; Zhang, J.-H.; Shi, D.; Jiang, M.; Zhu, Y.-X.; Mei, S.-R.; Zhou, Y.-K.; Dai, K.; Lu, B. Selective Solid-Phase Extraction of Cholesterol Using Molecularly Imprinted Polymers and Its Application in Different Biological Samples. *J. Pharm. Biomed. Anal.* **2006**, *42*, 549–555.

(95) Zhao, Y.; Ma, Y.; Li, H.; Wang, L. Composite QDs@MIP Nanospheres for Specific Recognition and Direct Fluorescent Quantification of Pesticides in Aqueous Media. *Anal. Chem.* **2012**, *84*, 386–395.

(96) Zhang, Y.; Zhang, J.; Liu, Q. Gas Sensors Based on Molecular Imprinting Technology. *Sensors* **2017**, *17*, 1567.

(97) Xu, S.; Lu, H.; Li, J.; Song, X.; Wang, A.; Chen, L.; Han, S. Dummy Molecularly Imprinted Polymers-Capped CdTe Quantum Dots for the Fluorescent Sensing of 2,4,6-Trinitrotoluene. *ACS Appl. Mater. Interfaces* **2013**, *5*, 8146–8154.

(98) Holthoff, E. L.; Stratis-Cullum, D. N.; Hankus, M. E. A Nanosensor for TNT Detection Based on Molecularly Imprinted Polymers and Surface Enhanced Raman Scattering. *Sensors* **2011**, *11*, 2700–2714.

(99) Alizadeh, T.; Zare, M.; Ganjali, M. R.; Norouzi, P.; Tavana, B. A New Molecularly Imprinted Polymer (MIP)-Based Electrochemical Sensor for Monitoring 2,4,6-Trinitrotoluene (TNT) in Natural Waters and Soil Samples. *Biosens. Bioelectron.* **2010**, *25*, 1166–1172.

(100) Bakhshpour, M.; Denizli, A. Highly Sensitive Detection of Cd(II) Ions Using Ion-Imprinted Surface Plasmon Resonance Sensors. *Microchem. J.* **2020**, *159*, 105572.

(101) Kan, X.; Zhou, H.; Li, C.; Zhu, A.; Xing, Z.; Zhao, Z. Imprinted Electrochemical Sensor for Dopamine Recognition and Determination Based on a Carbon Nanotube/Polypyrrole Film. *Electrochim. Acta* **2012**, *63*, 69–75.

(102) Anker, J. N.; Hall, W. P.; Lyandres, O.; Shah, N. C.; Zhao, J.; Van Duyne, R. P. Biosensing with Plasmonic Nanosensors. *Nat. Mater.* **2008**, *7*, 442–453.

(103) Tokarev, I.; Minko, S. Tunable Plasmonic Nanostructures from Noble Metal Nanoparticles and Stimuli-Responsive Polymers. *Soft Matter* **2012**, *8*, 5980.

(104) Kelly, K. L.; Coronado, E.; Zhao, L. L.; Schatz, G. C. The Optical Properties of Metal Nanoparticles: The Influence of Size, Shape, and Dielectric Environment. *J. Phys. Chem. B* **2003**, *107*, 668–677.

(105) Abargues, R.; Marqués-Hueso, J.; Canet-Ferrer, J.; Pedrueza, E.; Valdés, J. L.; Jiménez, E.; Martínez-Pastor, J. P. High-Resolution Electron-Beam Patternable Nanocomposite Containing Metal Nanoparticles for Plasmonics. *Nanotechnology* **2008**, *19*, 355308.

(106) Ferhan, A. R.; Kim, D.-H. Nanoparticle Polymer Composites on Solid Substrates for Plasmonic Sensing Applications. *Nano Today* **2016**, *11*, 415–434.

(107) Marqués-Hueso, J.; Abargues, R.; Valdés, J. L.; Martínez-Pastor, J. P. Ag and

Au/DNQ-Novolac Nanocomposites Patternable by Ultraviolet Lithography: A Fast Route to Plasmonic Sensor Microfabrication. *J. Mater. Chem.* **2010**, *20*, 7436.

(108) Marques-Hueso, J.; Abargues, R.; Richards, B. S.; Valdes, J. L.; Martinez-Pastor, J. P. Plasmon Dumping in Ag-Nanoparticles/Polymer Composite for Optical Detection of Amines and Thiols Vapors. In *Nanophotonics IV*; 2012; Vol. 8424, p 842410.

(109) Gómez-Gómez, M.; Calderón, J.; Abargues, R.; Rodríguez-Cantó, P. J.; Suárez, I.; Pastor, J. P. M.; Hill, D. An Advance Towards the Synthesis of Ag Nanorod Arrays with Controlled Surface Roughness for SERS Substrates. *Mater. Today Proc.* **2016**, *3*, 294–302.

(110) Ayankojo, A. G.; Reut, J.; Öpik, A.; Furchner, A.; Syritski, V. Hybrid Molecularly Imprinted Polymer for Amoxicillin Detection. *Biosens. Bioelectron.* **2018**, *118*, 102–107.

(111) Thanh, N. T. K.; Maclean, N.; Mahiddine, S. Mechanisms of Nucleation and Growth of Nanoparticles in Solution. *Chem. Rev.* **2014**, *114*, 7610–7630.

(112) Polte, J. Fundamental Growth Principles of Colloidal Metal Nanoparticles – a New Perspective. *CrystEngComm* **2015**, *17*, 6809–6830.

(113) Román, F.; Colomer, P.; Calventus, Y.; Hutchinson, J. Study of Hyperbranched Poly(Ethyleneimine) Polymers of Different Molecular Weight and Their Interaction with Epoxy Resin. *Materials (Basel).* **2018**, *11*, 410.

(114) Fragua, D. M.; Abargues, R.; Rodriguez-Canto, P. J.; Sanchez-Royo, J. F.; Agouram, S.; Martinez-Pastor, J. P. Au-ZnO Nanocomposite Films for Plasmonic Photocatalysis. *Adv. Mater. Interfaces* **2015**, *2*, 1500156.

(115) Pedrueza, E.; Valdés, J. L.; Chirvony, V.; Abargues, R.; Hernández-Saz, J.; Herrera, M.; Molina, S. I.; Martínez-Pastor, J. P. Novel Method of Preparation of Gold-Nanoparticle-Doped TiO2 and SiO2 Plasmonic Thin Films: Optical Characterization and Comparison with Maxwell-Garnett Modeling. *Adv. Funct. Mater.* **2011**, *21*, 3502–3507.

(116) Fragua, D.; Noguera-Gomez, J.; Rodríguez-Canto, P. J.; Valencia, L. M.; de la Mata, M.; Herrera, M.; Molina, S. I.; Abargues, R. Au–NiO x Nanocomposite for Hot Electron-Assisted Plasmonic Photocatalysis. *J. Mater. Chem. C* **2020**, *8*,

9885–9897.

(117) Ricci, A. *Amino Group Chemistry: From Synthesis to the Life Sciences*; Ricci, A., Ed.; Wiley, 2007.

(118) Agnihotri, S.; Mukherji, S.; Mukherji, S. Immobilized Silver Nanoparticles Enhance Contact Killing and Show Highest Efficacy: Elucidation of the Mechanism of Bactericidal Action of Silver. *Nanoscale* **2013**, *5*, 7328–7340.

(119) Zhao, Y.; Liu, L.; Li, C.; Ye, B.; Xiong, J.; Shi, X. Immobilization of Polyethyleneimine-Templated Silver Nanoparticles onto Filter Paper for Catalytic Applications. *Colloids Surfaces A Physicochem. Eng. Asp.* **2019**, *571*, 44–49.

(120) Jiang, K.; Kharel, P.; Peng, Y.; Gangishetty, M. K.; Lin, H.-Y. G.; Stavitski, E.; Attenkofer, K.; Wang, H. Silver Nanoparticles with Surface-Bonded Oxygen for Highly Selective CO2 Reduction. *ACS Sustain. Chem. Eng.* **2017**, *5*, 8529–8534.

(121) Sayari, A.; Heydari-Gorji, A.; Yang, Y. CO2-Induced Degradation of Amine-Containing Adsorbents: Reaction Products and Pathways. *J. Am. Chem. Soc.* **2012**, *134*, 13834–13842.

(122) Baggiani, C.; Giovannoli, C.; Anfossi, L.; Passini, C.; Baravalle, P.; Giraudi, G. A Connection between the Binding Properties of Imprinted and Nonimprinted Polymers: A Change of Perspective in Molecular Imprinting. *J. Am. Chem. Soc.* **2012**, *134*, 1513–1518.

(123) Foerster, B.; Spata, V. A.; Carter, E. A.; Sönnichsen, C.; Link, S. Plasmon Damping Depends on the Chemical Nature of the Nanoparticle Interface. *Sci. Adv.* **2019**, *5*.

(124) Rani, S.; Dilbaghi, N.; Kumar, S.; Varma, R. S.; Malhotra, R. Rapid Redox Sensing of P-Nitrotoluene in Real Water Samples Using Silver Nanoparticles. *Inorg. Chem. Commun.* **2020**, *120*, 108157.

(125) Riskin, M.; Tel-Vered, R.; Lioubashevski, O.; Willner, I. Ultrasensitive Surface Plasmon Resonance Detection of Trinitrotoluene by a Bis-Aniline-Cross-Linked Au Nanoparticles Composite. *J. Am. Chem. Soc.* **2009**, *131*, 7368–7378.

(126) Riskin, M.; Tel-Vered, R.; Bourenko, T.; Granot, E.; Willner, I. Imprinting of Molecular Recognition Sites through Electropolymerization of Functionalized Au

Nanoparticles: Development of an Electrochemical TNT Sensor Based on π-Donor−Acceptor Interactions. *J. Am. Chem. Soc.* **2008**, *130*, 9726–9733.

(127) Kobayashi, S.; Shirasaka, H.; Suh, K.; Uyama, H. Viscosity Behaviors and Gel Properties of Linear and Branched Polyethylenimines: Effects of Micro-Structures. *Polym. J.* **1990**, *22*, 442–446.

(128) Vandevelde, F.; Belmont, A.-S.; Pantigny, J.; Haupt, K. Hierarchically Nanostructured Polymer Films Based on Molecularly Imprinted Surface-Bound Nanofilaments. *Adv. Mater.* **2007**, *19*, 3717–3720.

(129) Findlay, J. W. A.; Smith, W. C.; Lee, J. W.; Nordblom, G. D.; Das, I.; DeSilva, B. S.; Khan, M. N.; Bowsher, R. R. Validation of Immunoassays for Bioanalysis: A Pharmaceutical Industry Perspective. *J. Pharm. Biomed. Anal.* **2000**, *21*, 1249–1273.

(130) O'Connell, M. A.; Belanger, B. A.; Haaland, P. D. Calibration and Assay Development Using the Four-Parameter Logistic Model. *Chemom. Intell. Lab. Syst.* **1993**, *20*, 97–114.

(131) Jung, L. S.; Shumaker-Parry, J. S.; Campbell, C. T.; Yee, S. S.; Gelb, M. H. Quantification of Tight Binding to Surface-Immobilized Phospholipid Vesicles Using Surface Plasmon Resonance: Binding Constant of Phospholipase A 2. *J. Am. Chem. Soc.* **2000**, *122*, 4177–4184.

(132) Kenakin, T. Principles: Receptor Theory in Pharmacology. *Trends Pharmacol. Sci.* **2004**, *25*, 186–192.

(133) Darmadi, I.; Nugroho, F. A. A.; Langhammer, C. High-Performance Nanostructured Palladium-Based Hydrogen Sensors—Current Limitations and Strategies for Their Mitigation. *ACS Sensors* **2020**, *5*, 3306–3327.

(134) Algarra, M.; Campos, B. B.; Miranda, M. S.; da Silva, J. C. G. E. CdSe Quantum Dots Capped PAMAM Dendrimer Nanocomposites for Sensing Nitroaromatic Compounds. *Talanta* **2011**, *83*, 1335–1340.

(135) Lu, H.; Carroll, G. M.; Neale, N. R.; Beard, M. C. Infrared Quantum Dots: Progress, Challenges, and Opportunities. *ACS Nano* **2019**, *13*, 939–953.

(136) Maulu, A.; Rodríguez-Cantó, P. J.; Navarro-Arenas, J.; Abargues, R.; Sánchez-

Royo, J. F.; García-Calzada, R.; Martínez Pastor, J. P. Strongly-Coupled PbS QD Solids by Doctor Blading for IR Photodetection. *RSC Adv.* **2016**, *6*, 80201–80212.

(137) Maulu, A.; Navarro-Arenas, J.; Rodríguez-Cantó, P.; Sánchez-Royo, J.; Abargues, R.; Suárez, I.; Martínez-Pastor, J. Charge Transport in Trap-Sensitized Infrared PbS Quantum-Dot-Based Photoconductors: Pros and Cons. *Nanomaterials* **2018**, *8*, 677.

(138) Yadav, P. V. K.; Ajitha, B.; Kumar Reddy, Y. A.; Sreedhar, A. Recent Advances in Development of Nanostructured Photodetectors from Ultraviolet to Infrared Region: A Review. *Chemosphere* **2021**, *279*, 130473.

(139) Yan, L.; Shen, X.; Zhang, Y.; Zhang, T.; Zhang, X.; Feng, Y.; Yin, J.; Zhao, J.; Yu, W. W. Near-Infrared Light Emitting Diodes Using PbSe Quantum Dots. *RSC Adv.* **2015**, *5*, 54109–54114.

(140) Abargues, R.; Navarro, J.; Rodríguez-Cantó, P. J.; Maulu, A.; Sánchez-Royo, J. F.; Martínez-Pastor, J. P. Enhancing the Photocatalytic Properties of PbS QD Solids: The Ligand Exchange Approach. *Nanoscale* **2019**, *11*, 1978–1987.

(141) Yuan, M.; Liu, M.; Sargent, E. H. Colloidal Quantum Dot Solids for Solution-Processed Solar Cells. *Nat. Energy* **2016**, *1*, 16016.

(142) Gordillo, H.; Suarez, I.; Abargues, R.; Rodriguez-Canto, P.; Almuneau, G.; Martinez-Pastor, J. P. Quantum-Dot Double Layer Polymer Waveguides by Evanescent Light Coupling. *J. Light. Technol.* **2013**, *31*, 2515–2525.

(143) Gordillo, H.; Suarez, I.; Abargues, R.; Rodriguez-Canto, P.; Martinez-Pastor, J. P. Color Tuning and White Light by Dispersing CdSe, CdTe, and CdS in PMMA Nanocomposite Waveguides. *IEEE Photonics J.* **2013**, *5*, 2201412–2201412.

(144) Freeman, R.; Willner, I. Optical Molecular Sensing with Semiconductor Quantum Dots (QDs). *Chem. Soc. Rev.* **2012**, *41*, 4067–4085.

(145) Ze, L.; Yueqiu, G.; Xujun, L.; Yong, Z. MoS2-Modified ZnO Quantum Dots Nanocomposite: Synthesis and Ultrafast Humidity Response. *Appl. Surf. Sci.* **2017**, *399*, 330–336.

(146) Bueno, A.; Suarez, I.; Abargues, R.; Sales, S.; Pastor, J. P. M. Temperature

Sensor Based on Colloidal Quantum Dots–PMMA Nanocomposite Waveguides. *IEEE Sens. J.* **2012**, *12*, 3069–3074.

(147) Paramanik, B.; Bhattacharyya, S.; Patra, A. Detection of Hg2+ and F− Ions by Using Fluorescence Switching of Quantum Dots in an Au-Cluster-CdTe QD Nanocomposite. *Chem. - A Eur. J.* **2013**, *19*, 5980–5987.

(148) Devi, S.; Kaur, R.; Paul, A. K.; Tyagi, S. MPA-Capped CdSe QD/Mercaptoethylamine-Capped AuNP Nanocomposite-Based Sensor for Instant Detection of Trinitrotoluene. *Colloid Polym. Sci.* **2018**, *296*, 427–440.

(149) Shi, G. H.; Shang, Z. Bin; Wang, Y.; Jin, W. J.; Zhang, T. C. Fluorescence Quenching of CdSe Quantum Dots by Nitroaromatic Explosives and Their Relative Compounds. *Spectrochim. Acta Part A Mol. Biomol. Spectrosc.* **2008**, *70*, 247–252.

(150) Hines, D. A.; Kamat, P. V. Recent Advances in Quantum Dot Surface Chemistry. *ACS Appl. Mater. Interfaces* **2014**, *6*, 3041–3057.

(151) Freeman, R.; Willner, I. NAD+/NADH-Sensitive Quantum Dots: Applications To Probe NAD + -Dependent Enzymes and To Sense the RDX Explosive. *Nano Lett.* **2009**, *9*, 322–326.

(152) Komikawa, T.; Tanaka, M.; Tamang, A.; Evans, S. D.; Critchley, K.; Okochi, M. Peptide-Functionalized Quantum Dots for Rapid Label-Free Sensing of 2,4,6-Trinitrotoluene. *Bioconjug. Chem.* **2020**, *31*, 1400–1407.

(153) Wu, Z.; Duan, H.; Li, Z.; Guo, J.; Zhong, F.; Cao, Y.; Jia, D. Multichannel Discriminative Detection of Explosive Vapors with an Array of Nanofibrous Membranes Loaded with Quantum Dots. *Sensors* **2017**, *17*, 2676.

(154) Feng, S.; Farha, F.; Li, Q.; Wan, Y.; Xu, Y.; Zhang, T.; Ning, H. Review on Smart Gas Sensing Technology. *Sensors* **2019**, *19*, 3760.

(155) Xu, Q.; Zhang, Y.; Tang, B.; Zhang, C. Multicolor Quantum Dot-Based Chemical Nose for Rapid and Array-Free Differentiation of Multiple Proteins. *Anal. Chem.* **2016**, *88*, 2051–2058.

(156) Potyrailo, R. A.; Leach, A. M.; Surman, C. M. Multisize CdSe Nanocrystal/Polymer Nanocomposites for Selective Vapor Detection Identified

from High-Throughput Screening Experimentation. *ACS Comb. Sci.* **2012**, *14*, 170–178.

(157) Bright, C. J.; Nallon, E. C.; Polcha, M. P.; Schnee, V. P. Quantum Dot and Polymer Composite Cross-Reactive Array for Chemical Vapor Detection. *Anal. Chem.* **2015**, *87*, 12270–12275.

(158) Yu, W. W.; Peng, X. Formation of High-Quality CdS and Other II-VI Semiconductor Nanocrystals in Noncoordinating Solvents: Tunable Reactivity of Monomers. *Angew. Chemie Int. Ed.* **2002**, *41*, 2368–2371.

(159) Woodruff, M. A.; Hutmacher, D. W. The Return of a Forgotten Polymer—Polycaprolactone in the 21st Century. *Prog. Polym. Sci.* **2010**, *35*, 1217–1256.

(160) Meikhail, M. S.; Abdelghany, A. M.; Awad, W. M. Role of CdSe Quantum Dots in the Structure and Antibacterial Activity of Chitosan/Poly ε-Caprolactone Thin Films. *Egypt. J. Basic Appl. Sci.* **2018**, *5*, 138–144.

(161) Aznar-Gadea, E.; Rodríguez-Canto, P. J.; Martínez-Pastor, J. P.; Lopatynskyi, A.; Chegel, V.; Abargues, R. Molecularly Imprinted Silver Nanocomposites for Explosive Taggant Sensing. *ACS Appl. Polym. Mater.* **2021**, *3*, 2960–2970.

(162) Pholosi, A.; Naidoo, E. B.; Ofomaja, A. E. Intraparticle Diffusion of Cr(VI) through Biomass and Magnetite Coated Biomass: A Comparative Kinetic and Diffusion Study. *South African J. Chem. Eng.* **2020**, *32*, 39–55.

(163) Frasco, M.; Chaniotakis, N. Semiconductor Quantum Dots in Chemical Sensors and Biosensors. *Sensors* **2009**, *9*, 7266–7286.

(164) Choi, J.; Shin, H.; Yang, S.; Cho, M. The Influence of Nanoparticle Size on the Mechanical Properties of Polymer Nanocomposites and the Associated Interphase Region: A Multiscale Approach. *Compos. Struct.* **2015**, *119*, 365–376.

(165) Aznar-Gadea, E.; Sanchez-Alarcon, I.; Soosaimanickam, A.; Rodriguez-Canto, P. J.; Perez-Pla, F.; Martínez-Pastor, J. P.; Abargues, R. Molecularly Imprinted Nanocomposites of CsPbBr3 Nanocrystals: An Approach towards Fast and Selective Gas Sensing of Explosive Taggants. *J. Mater. Chem. C* **2022**, *10*, 1754–1766.

(166) Manser, J. S.; Christians, J. A.; Kamat, P. V. Intriguing Optoelectronic Properties

of Metal Halide Perovskites. *Chem. Rev.* **2016**, *116*, 12956–13008.

(167) Yang, D.; Cao, M.; Zhong, Q.; Li, P.; Zhang, X.; Zhang, Q. All-Inorganic Cesium Lead Halide Perovskite Nanocrystals: Synthesis, Surface Engineering and Applications. *J. Mater. Chem. C* **2019**, *7*, 757–789.

(168) Zhou, Y.; Padture, N. P. Gas-Induced Formation/Transformation of Organic–Inorganic Halide Perovskites. *ACS Energy Lett.* **2017**, *2*, 2166–2176.

(169) Kakavelakis, G.; Gagaoudakis, E.; Petridis, K.; Petromichelaki, V.; Binas, V.; Kiriakidis, G.; Kymakis, E. Solution Processed CH3NH3PbI3– x Clx Perovskite Based Self-Powered Ozone Sensing Element Operated at Room Temperature. *ACS Sensors* **2018**, *3*, 135–142.

(170) Stoeckel, M.-A.; Gobbi, M.; Bonacchi, S.; Liscio, F.; Ferlauto, L.; Orgiu, E.; Samorì, P. Reversible, Fast, and Wide-Range Oxygen Sensor Based on Nanostructured Organometal Halide Perovskite. *Adv. Mater.* **2017**, *29*, 1702469.

(171) Sun, W.; Huang, C.; Fan, R.; Liu, S.; Wang, Y.; Xiao, Y.; Gan, Q.; Xiao, S.; Song, Q. On-Chip-Integrated Methylammonium Halide Perovskite Optical Sensors. *Adv. Opt. Mater.* **2019**, *7*, 1801308.

(172) Xu, W.; Li, F.; Cai, Z.; Wang, Y.; Luo, F.; Chen, X. An Ultrasensitive and Reversible Fluorescence Sensor of Humidity Using Perovskite CH3NH3PbBr3. *J. Mater. Chem. C* **2016**, *4*, 9651–9655.

(173) Ren, K.; Huang, L.; Yue, S.; Lu, S.; Liu, K.; Azam, M.; Wang, Z.; Wei, Z.; Qu, S.; Wang, Z. Turning a Disadvantage into an Advantage: Synthesizing High-Quality Organometallic Halide Perovskite Nanosheet Arrays for Humidity Sensors. *J. Mater. Chem. C* **2017**, *5*, 2504–2508.

(174) Sheng, X.; Liu, Y.; Wang, Y.; Li, Y.; Wang, X.; Wang, X.; Dai, Z.; Bao, J.; Xu, X. Cesium Lead Halide Perovskite Quantum Dots as a Photoluminescence Probe for Metal Ions. *Adv. Mater.* **2017**, *29*, 1700150.

(175) Ruan, S.; Lu, J.; Pai, N.; Ebendorff-Heidepriem, H.; Cheng, Y.-B.; Ruan, Y.; McNeill, C. R. An Optical Fibre-Based Sensor for the Detection of Gaseous Ammonia with Methylammonium Lead Halide Perovskite. *J. Mater. Chem. C* **2018**, *6*, 6988–6995.

(176) Chen, J.; Mo, Z.-H.; Yang, X.; Zhou, H.-L.; Gao, Q. Exploration of Organic–Inorganic Hybrid Perovskites for Surface-Enhanced Infrared Spectroscopy of Small Molecules. *Chem. Commun.* **2017**, *53*, 6949–6952.

(177) Shamsi, J.; Urban, A. S.; Imran, M.; De Trizio, L.; Manna, L. Metal Halide Perovskite Nanocrystals: Synthesis, Post-Synthesis Modifications, and Their Optical Properties. *Chem. Rev.* **2019**, *119*, 3296–3348.

(178) Chen, X.; Sun, C.; Liu, Y.; Yu, L.; Zhang, K.; Asiri, A. M.; Marwani, H. M.; Tan, H.; Ai, Y.; Wang, X.; Wang, S. All-Inorganic Perovskite Quantum Dots CsPbX3 (Br/I) for Highly Sensitive and Selective Detection of Explosive Picric Acid. *Chem. Eng. J.* **2020**, *379*, 122360.

(179) Shan, X.; Zhang, S.; Zhou, M.; Geske, T.; Davis, M.; Hao, A.; Wang, H.; Yu, Z. Porous Halide Perovskite–Polymer Nanocomposites for Explosive Detection with a High Sensitivity. *Adv. Mater. Interfaces* **2019**, *6*, 1801686.

(180) Zu, B.; Guo, Y.; Dou, X. Nanostructure-Based Optoelectronic Sensing of Vapor Phase Explosives – a Promising but Challenging Method. *Nanoscale* **2013**, *5*, 10693.

(181) Chen, P.-C.; Sukcharoenchoke, S.; Ryu, K.; Gomez de Arco, L.; Badmaev, A.; Wang, C.; Zhou, C. 2,4,6-Trinitrotoluene (TNT) Chemical Sensing Based on Aligned Single-Walled Carbon Nanotubes and ZnO Nanowires. *Adv. Mater.* **2010**, *22*, 1900–1904.

(182) Che, Y.; Yang, X.; Liu, G.; Yu, C.; Ji, H.; Zuo, J.; Zhao, J.; Zang, L. Ultrathin N-Type Organic Nanoribbons with High Photoconductivity and Application in Optoelectronic Vapor Sensing of Explosives. *J. Am. Chem. Soc.* **2010**, *132*, 5743–5750.

(183) Muthu, C.; Nagamma, S. R.; Nair, V. C. Luminescent Hybrid Perovskite Nanoparticles as a New Platform for Selective Detection of 2,4,6-Trinitrophenol. *RSC Adv.* **2014**, *4*, 55908–55911.

(184) Huang, S.; Guo, M.; Tan, J.; Geng, Y.; Wu, J.; Tang, Y.; Su, C.; Lin, C. C.; Liang, Y. Novel Fluorescence Sensor Based on All-Inorganic Perovskite Quantum Dots Coated with Molecularly Imprinted Polymers for Highly Selective and Sensitive Detection of Omethoate. *ACS Appl. Mater. Interfaces* **2018**, *10*, 39056–39063.

(185) Protesescu, L.; Yakunin, S.; Bodnarchuk, M. I.; Krieg, F.; Caputo, R.; Hendon, C. H.; Yang, R. X.; Walsh, A.; Kovalenko, M. V. Nanocrystals of Cesium Lead Halide Perovskites (CsPbX3, X=Cl, Br, and I): Novel Optoelectronic Materials Showing Bright Emission with Wide Color Gamut. *Nano Lett.* **2015**, *15*, 3692–3696.

(186) Guarino, V.; Gentile, G.; Sorrentino, L.; Ambrosio, L. Polycaprolactone: Synthesis, Properties, and Applications. In *Encyclopedia of Polymer Science and Technology*; John Wiley & Sons, Inc.: Hoboken, NJ, USA, 2017; pp 1–36.

(187) Salmieri, S.; Lacroix, M. Physicochemical Properties of Alginate/Polycaprolactone-Based Films Containing Essential Oils. *J. Agric. Food Chem.* **2006**, *54*, 10205–10214.

(188) Lan, Y.; Wang, Y.; Song, Y. Efficient Flexible Perovskite Solar Cells Based on a Polymer Additive. *Flex. Print. Electron.* **2020**, *5*, 014001.

(189) Mohd Yusoff, A. R. Bin; Vasilopoulou, M.; Georgiadou, D. G.; Palilis, L. C.; Abate, A.; Nazeeruddin, M. K. Passivation and Process Engineering Approaches of Halide Perovskite Films for High Efficiency and Stability Perovskite Solar Cells. *Energy Environ. Sci.* **2021**, *14*, 2906–2953.

(190) Wang, Y.; Zhang, Z.; Tao, M.; Lan, Y.; Li, M.; Tian, Y.; Song, Y. Interfacial Modification towards Highly Efficient and Stable Perovskite Solar Cells. *Nanoscale* **2020**, *12*, 18563–18575.

(191) Gorodzha, S. N.; Surmeneva, M. A.; Surmenev, R. A. Fabrication and Characterization of Polycaprolactone Cross-Linked and Highly-Aligned 3-D Artificial Scaffolds for Bone Tissue Regeneration via Electrospinning Technology. *IOP Conf. Ser. Mater. Sci. Eng.* **2015**, *98*, 012024.

(192) Lee, E. J.; Kim, D.-H.; Chang, R. P. H.; Hwang, D.-K. Induced Growth of CsPbBr3 Perovskite Films by Incorporating Metal Chalcogenide Quantum Dots in PbBr2 Films for Performance Enhancement of Inorganic Perovskite Solar Cells. *ACS Appl. Energy Mater.* **2020**, *3*, 10376–10383.

(193) Pashaei Adl, H.; Gorji, S.; Muñoz-Matutano, G.; Sánchez-Alarcón, R. I.; Abargues, R.; Gualdrón-Reyes, A. F.; Mora-Seró, I.; Martínez-Pastor, J. P. Homogeneous and Inhomogeneous Broadening in Single Perovskite Nanocrystals Investigated by Micro-Photoluminescence. *J. Lumin.* **2021**, *240*, 1–

8.

(194) Zhu, W.; Tao, S.; Tao, C.; Li, W.; Lin, C.; Li, M.; Wen, Y.; Li, G. Hierarchically Imprinted Porous Films for Rapid and Selective Detection of Explosives. *Langmuir* **2011**, *27*, 8451–8457.

(195) Geethanjali, H. S.; Nagaraja, D.; Melavanki, R. M.; Kusanur, R. A. Fluorescence Quenching of Boronic Acid Derivatives by Aniline in Alcohols – A Negative Deviation from Stern–Volmer Equation. *J. Lumin.* **2015**, *167*, 216–221.

(196) Tan, W.; Yu, Q.; Ruan, X.; Huang, X. Design of SnO2-Based Highly Sensitive Ethanol Gas Sensor Based on Quasi Molecular-Cluster Imprinting Mechanism. *Sensors Actuators B Chem.* **2015**, *212*, 47–54.

Appendices

A. List of acronyms

- **1-NN:** 1-Nitronaphtalene
- **2D:** Two-dimensional
- **2-MET:** 2-Mercaptoethanol
- **2-NT:** 2-Nitrotoluene
- **3-NT:** 3-Nitrotoluene
- **4-NP:** 4-Nitrophenol
- **4-NT:** 4-Nitrotoluene
- **5-NI:** 5-Nitroisoquinoline
- **ACN:** Acetonitrile
- **AFM:** Atomic force microscopy
- **Ag:** Silver
- **$AgNO_3$:** Silver Nitrate
- **AN:** Ammonium nitrate
- **ANFO:** Ammonium nitrate fuel oil
- **AP:** Ammonium phosphate
- **Au:** Gold
- **CdO:** Cadmium oxide
- **ClBz:** Chlorobenzene
- **CO:** Carbon monoxide
- **DADP:** Diacetone diperoxide
- **DMDNB:** 2,3-dimethyl-2,3-dinitrobutane
- **EDA:** Ethylenediamine
- **EtOAc:** Ethyl acetate
- **FID:** Flame ionization detector
- **FRET:** Fluorescence resonance energy transfer
- **FT-IR:** Fourier-transform infrared spectroscopy
- **FWHM:** Full width at half maximum
- **GC:** Gas chromatography
- **GC-MS:** Gas chromatography–mass spectrometry

- **HMTD:** Hexamethylene triperoxide diamine
- **HMX:** Octogen
- **HNS:** Hexanitrostilbene
- **HPLC-MS:** Liquid chromatography-mass spectrometry
- **HR-TEM:** High-resolution transmission electron microscopy
- **HXM:** Hexamine
- **ICT:** Intramolecular charge transfer
- **IED:** Improvised explosive device
- **K_A:** Binding affinity
- **LC:** Liquid chromatography
- **LOD:** Limit of detection
- **LSPR:** Localized surface plasmon resonance
- **m/z:** Mass-to-charge ratio
- **MeOH:** Methanol
- **MIP:** Molecularly imprinted polymer
- **MIT:** Molecularly imprinted technology
- **MS:** Mass spectrometry
- **MW_e:** Molecular weight of the explosive
- **NC:** Nitrocellulose
- **NCs:** Nanocrystals
- **NG:** Nitroglycerine
- **NIP:** Non-molecularly imprinted polymer
- **NM:** Nitromethane
- **NP:** Nanoparticle
- **OA:** Oleic acid
- **OAm:** Oleylamine
- **OB:** Oxygen balance
- **ODE:** 1-Octadecene
- **PA:** Picric acid
- **PBXs:** Polymer bonded explosives
- **PCL:** Polycaprolactone
- **PEI:** Polyethyleneimine
- **PET:** Photo-induced electron transfer
- **PETN:** Pentaerythritol tetranitrate

- **PL:** Photoluminescence
- **PLQY:** Photoluminescence quantum yield
- **PVK:** Perovskite
- **Q:** Heat of explosion
- **QD:** Quantum dot
- **R_a:** Surface roughness
- **RDX:** Hexogen, 3,5-trinitroperhydro-1,3,5-triazine
- **RET:** Resonance energy transfer
- **SERS:** Surface enhanced Raman scattering
- **SFC:** Supercritical fluid chromatography
- **TATB:** Triaminotrinitrobenzene
- **TATP:** Triacetone triperoxide
- **TEM:** Transmission electron microscopy
- **T_g:** Glass transition temperature
- **TNT:** 2,4,6-trinitrotoluene
- **TOF:** Time-of-flight
- **TOP:** Trioctylphosphine
- **V:** Volume of gas
- **VOC:** Volatile organic compound
- **VOD:** Velocity of detonation
- **XRD:** X-ray diffraction
- **ΔH_p:** Heat of formation of the products
- **ΔH_r:** Heat of formation of the explosive

B. List of Figures

C. List of Schemes

D. List of Tables

E. Publications

- V.I. Chegel, A.M. Lopatynskyi, V.K. Lytvyn, P.V. Demydov, J.P. Martínez-Pastor, R. Abargues, **E.A. Gadea**, S.A. Piletsky, *Localized surface plasmon resonance nanochips with molecularly imprinted polymer coating for explosives sensing*, Semiconductor Physics, Quantum Electronics & Optoelectronics, 2020, 23, 431-436, DOI: 10.15407/spqeo23.04.431.

- **Eduardo Aznar-Gadea**, Pedro J. Rodríguez-Canto, Juan P. Martínez-Pastor, Andrii Lopatynskyi, Vladimir Chegel, and Rafael Abargues, *Molecularly Imprinted Silver Nanocomposites for Explosive Taggant Sensing*, ACS Applied Polymer Materials, 2021, 3, 2960-2970, DOI: 10.1021/acsapm.1c00116.

- **Eduardo Aznar-Gadea**, Pedro J. Rodriguez-Canto, Sandra Albert Sánchez, Juan P. Martínez-Pastor and Rafael Abargues, *Luminescent CdSe Quantum Dot Arrays for Rapid Sensing of Explosive Taggants*, ACS Applied Nano Materials, 2022, 5, 6717-6725, DOI: 10.1021/acsanm.2c007432022.

- **Eduardo Aznar-Gadea**, Ivan Sanchez-Alarcon, Ananthakumar Soosaimanickam, Pedro J. Rodriguez-Canto, F. Perez-Pla, Juan P. Martínez-Pastor, and Rafael Abargues, *Molecularly imprinted nanocomposites of $CsPbBr_3$ nanocrystals: an approach towards fast and selective gas sensing of explosive taggants*, Journal of Materials Chemistry C, 2022, 10, 1754-1766, DOI: 10.1039/D1TC05169E.